



Fakultät für Elektrotechnik und Informationstechnik  
Lehrstuhl für Nanoelektronik

# Fabrication and Characterization of Carbon Nanotube Random Network Transistors

Qingqing Gong

Vollständiger Abdruck der von der Fakultät für Elektrotechnik und Informationstechnik  
der Technischen Universität München zur Erlangung des akademischen Grades eines

Doktor-Ingenieurs

genehmigten Dissertation.

Vorsitzender:	Univ.-Prof. Dr. Thomas Hamacher
Prüfer der Dissertation:	1. Univ.-Prof. Paolo Lugli, Ph.D. 2. Univ.-Prof. Dr. Franz Kreupl

Die Dissertation wurde am 05.11.2014 bei der Technischen Universität München eingereicht und durch die Fakultät für Elektrotechnik und Informationstechnik am 07.05.2015 angenommen.



# Zusammenfassung

Zwecks Herstellung von Feldeffekttransistoren aus ungeordneten Netzen von Kohlenstoffnanoröhren wurde eine Technik entwickelt, die Tropfenbeschichtung mit Lochmaskenabscheidung kombiniert und mit Lösungen bearbeitbar ist. Die Technik, die einfach, schnell und zuverlässig ist, erlaubt direkte Steuerung über Netzdichte und damit Transistoreigenschaften. Eine systematische Untersuchung über Faktoren, die Transistorleistung beeinflussen, bietet neue Kenntnisse sowie Leitlinien künftiger Optimierung.

**Stichwörter:** Halbleiterbereicherung, Kohlenstoffnanoröhren-Feldeffekttransistor, Leistungsanalyse, metallische Rohrdichte, Tropfenbeschichtung, ungeordnetes Netzwerk.



# Abstract

A solution-processable technique combining drop-casting and shadow-mask deposition was developed for the fabrication of field-effect transistors based on carbon nanotube random networks. The proposed technique, which is easy, fast, and reliable, allows direct control of network density and thus of the transistor characteristics. A systematic study has been carried out on the factors influencing the transistor performance, which provides novel knowledge and guidance for future device optimization.

**Keywords:** CNTFET, drop-casting, metallic tube density, performance analysis, random network, semiconductor enrichment.



# Acknowledgements

This work was sponsored by the German Research Foundation (DFG) through the TUM International Graduate School of Science and Engineering (IGSSE) and the TUM Institute for Advanced Studies (IAS).

I am very grateful to my principal doctoral advisors Prof. Paolo Lugli and Dr. Giuseppe Scarpa from the Institute for Nanoelectronics, Technische Universität München (TUM), and Prof. Chan Bee Eng Mary (alias Mary B. Chan-Park) from the School of Chemical & Biomedical Engineering, Nanyang Technological University in Singapore (NTU).

From TUM, I also want to thank Dr. Bernhard Fabel for helpful discussion and experimental guidance to characterization of semiconductor devices. I am grateful to Rosi Heilmann for her experimental assistance. I would like to thank Edgar Albert and Vijay Deep Bhatt for their simulations on CNT random networks, and Mario Bareiß for his patience by taking high-resolution SEM images. Thanks to Igor E. Nikolskiy and Alexander Weise for doing part of measurements on CNTFETs. Thanks to Quan Niu Pan for her advice on how to prepare CNT suspensions. Thanks to Alexandra Münzer for introducing precise pipetting instrument. I further would like thank Margi Remm from the Institute for Medical Electronics, TUM, for her kind help by preparing silicon wafers with various oxide thicknesses.

I am deeply grateful to Associate Prof. Zhang Qing from the School of Electrical & Electronic Engineering, NTU, for kindly hosting me in his group for a three-month research visit. I also want to thank Dr. Zhou Jianping and Zhang Kang for helpful

discussion and experimental guidance. Thanks to Neo Bee Geok for her assistance by using SEM and Raman spectroscopy.

I further want to thank the group of Prof. Zhang Qing for having produced CNTFETs based on individual CNT-ropes for this research. And thanks to Pyria R. D. Mariathomas from the group of Prof. Chan, for CNTFET samples made by her.

Finally, I want to thank my parents and friends for their supports during the past years.

Munich, November 2014



# Contents

<b>1</b>	<b>Introduction.....</b>	<b>13</b>
1.1	About this research project.....	14
1.2	About this thesis .....	17
<b>2</b>	<b>Carbon Nanotube as Electronic Material.....</b>	<b>21</b>
2.1	Progress of carbon nanotube research .....	22
2.2	Structure and properties of carbon nanotubes .....	24
2.2.1	Chirality of single-walled carbon nanotubes .....	24
2.2.2	Electronic type of single-walled carbon nanotubes .....	26
2.3	Carbon nanotube field-effect transistors .....	29
2.3.1	Individual rope-based carbon nanotube transistors.....	29
2.3.2	Random network-based carbon nanotube transistors .....	32
<b>3</b>	<b>Fabrication of Carbon Nanotube Random Network Transistors .....</b>	<b>37</b>
3.1	Preparation of carbon nanotube suspension .....	38
3.1.1	Semiconductor-enriched carbon nanotubes .....	38
3.1.2	Solubility of single-walled carbon nanotubes.....	41
3.2	Deposition of carbon nanotube random network .....	43
3.2.1	Substrate preparation .....	43
3.2.2	Printing and coating techniques .....	46
3.2.3	Network density control.....	48
3.3	Contacting carbon nanotube random network .....	51
<b>4</b>	<b>Characterization of Carbon Nanotube Random Network Transistors .....</b>	<b>55</b>
4.1	Transistor characteristics .....	56
4.2	Characterization of transistor performance .....	59

4.2.1	On-off ratio .....	59
4.2.2	Transconductance and drain conductance .....	61
4.2.3	Mobilities .....	65
4.2.4	Threshold voltage and subthreshold swing.....	69
4.2.5	Frequency characteristics.....	72
4.3	Raman spectroscopy.....	75
4.3.1	Raman spectra of single-walled carbon nanotubes .....	75
4.3.2	Confocal Raman imaging of carbon nanotube random network .....	78
<b>5</b>	<b>Performance Analysis of Carbon Nanotube Random Network Transistors.....</b>	<b>83</b>
5.1	Design of experiment .....	84
5.2	Influence of network properties .....	87
5.2.1	Influence factors concerning the on-off ratio.....	87
5.2.2	Influence factors concerning the field-effect mobility.....	90
5.2.3	Tube diameter as an influence factor .....	93
5.3	Hysteresis .....	96
<b>6</b>	<b>Conclusion and Outlook.....</b>	<b>101</b>
<b>A</b>	<b>How to make a CNTFET.....</b>	<b>105</b>
<b>B</b>	<b>List of Work Functions.....</b>	<b>107</b>
<b>C</b>	<b>List of Symbols .....</b>	<b>109</b>
<b>D</b>	<b>Abbreviations and Acronyms .....</b>	<b>113</b>
<b>E</b>	<b>List of Publications.....</b>	<b>115</b>
	<b>Bibliography .....</b>	<b>117</b>

# List of Figures

1.1	Schedule for research and development on carbon-based nanoelectronics	14
2.1	Common structures of carbon allotropes .....	23
2.2	Chirality of single-walled carbon nanotubes .....	25
2.3	Band structure and density of states from the zone-folding model .....	27
2.4	Schematic band diagram of metal-semiconductor contacts .....	30
2.5	Individual rope-based carbon nanotube transistors .....	31
2.6	Random network-based carbon nanotube transistors .....	33
2.7	Carbon nanotube random network transistors as impedimetric pH sensor	34
3.1	Carbon nanotube suspensions .....	42
3.2	Schematic diagram of functionalization on substrate surface .....	44
3.3	Shadow-mask deposition for nanotube network and metal contacts .....	45
3.4	Carbon nanotube random networks deposited on silicon substrate .....	47
3.5	Random network-based CNTFETs with different network density .....	50
3.6	Commonly used structures for carbon nanotube transistors .....	52
3.7	Device layout of the back-gated CNTFET .....	53
3.8	Performance of CNTFETs as a function of channel length.....	54
4.1	Transistor characteristics of random network-based CNTFET .....	57

4.2	Influence of measurement settings on the range of on-off ratio .....	60
4.3	Characterization of transconductance .....	62
4.4	Transconductance influenced by measurement temperature .....	63
4.5	Comparison of transconductance and drain conductance .....	65
4.6	Comparison of MOSFET mobilities .....	66
4.7	Influence of gate oxide capacitance on field-effect mobility .....	68
4.8	Threshold voltage determined by the linear extrapolation method .....	71
4.9	Small-signal equivalent circuit for CNTFET.....	73
4.10	Raman spectra of single-walled carbon nanotubes .....	76
4.11	Confocal Raman images of random carbon nanotube networks .....	78
4.12	Confocal Raman images of random network-based CNTFETs .....	80
5.1	Sample size of the systematic study .....	85
5.2	The average on-off ratio of random network-based CNTFETs .....	88
5.3	Statistic of drain currents and on-off ratio .....	89
5.4	The average field-effect mobility of random network-based CNTFETs ....	91
5.5	Statistic of field-effect mobility .....	92
5.6	Transistor performance influenced by tube diameter .....	94
5.7	Hysteresis observed in random network-based CNTFETs .....	97
5.8	Statistic of hysteresis and on-off ratio .....	98

## List of Tables

3.1	Commercial carbon nanotube products .....	39
3.2	Density gradation of CNT random networks .....	49
4.1	Device performance of random network-based CNTFETs .....	82
4.2	Raman spectroscopic features of CNTs .....	78



# Chapter 1

## Introduction

Research on carbon nanotube (CNT) has flourished since the 1990's, inspired by the observation of multi-walled CNTs (MWNTs) and later on single-walled CNTs (SWNTs) [1]-[2]. CNTs have a quasi-one-dimensional structure that can be considered as rolling up one single graphene sheet for SWNTs or several coaxial layers of graphene sheets for MWNTs [1]. Research has shown promising properties of CNTs in the fields of electrical transport [3], optical transmittance [4], thermal conductivity [5], electrochemical sensitivity and biocompatibility [6]-[7], mechanical bendability and flexibility [8]-[9], and mechanical strength with lightweight [10]. Depending on the tube structure, SWNTs can be either metallic or semiconducting [3]-[4], which makes them especially attractive candidate for the next-generation semiconductor industries.

The quasi-one-dimensional CNTs can be used to build nanometer-scale semiconducting channel in carbon nanotube field-effect transistors (CNTFETs). The International Technology Roadmap for Semiconductors (ITRS) has recommended carbon-based nanoelectronics, including CNT and graphene devices, as extension to complementary metal-oxide-semiconductor (CMOS) or beyond CMOS devices for scaling in information processing technologies [11]-[12]. Fig. 1.1 shows a schedule planned for the research and development on carbon-based nanoelectronics from 2009 to 2016, which includes challenges like ohmic contacts between nanotube and metal contacts, high- $\kappa$  gate dielectric and gate metal, controlled growth of CNTs in terms of

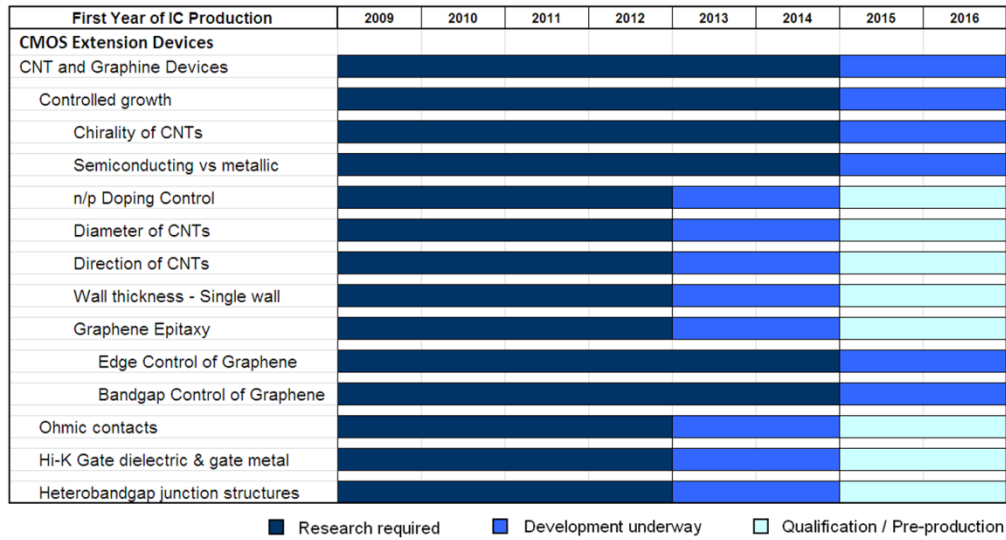


**Figure 1.1** Schedule for research and development on carbon-based nanoelectronics: listed from 2009 to 2019 to impact the industrial timetable for device scaling in following three phases: research required, development underway, and qualification and pre-production [11].

chirality, tube diameter, tube direction, electronic type, and doping [11]. CNTFETs are expected to provide promising performance like ballistic transport, high charge carrier mobility, small subthreshold swing, and low leakage current [13]-[15].

In addition to individual rope-based CNTFET, CNT random network or aligned CNT array can also be used as micrometer-scale semiconducting channel, for instance as an alternative to organic thin-film transistor (OTFT) that has organic molecules as semiconducting channel [16]. In recent years, field-effect transistors (FETs) based on CNT random network or aligned CNT array have been demonstrated with wide range of applications such as in flexible electronics [17], radio frequency technique [18], and sensor technique [19]. A milestone in this research field is the invention of a sorting technique known as the density gradient ultracentrifugation (DGU) which enables high-yield production of CNTs sorted by their electronic types [20].

## 1.1 About this research project

The research project as a whole was entitled “Carbon nanotube-based printed electronics” with the aim towards the manufacturability of CNT-based printed electronics. The project



was included in an international collaborated research programme led by the Nanyang Technological University in Singapore, Technische Universität München (TUM), University of Illinois (Urbana-Champaign), Massachusetts Institute of Technology, Dayton University, and ST Microelectronics as an industrial partner. The overall objective of the research programme was to develop printed CNTFETs with high yield and high performance in terms of high mobility and large on-off ratio. A prototype device was to be demonstrated in high-performance logic circuits with a special focus on the field of radio frequency technique. The research team from TUM was to contribute in following two parts, while this thesis mainly involved in the first part:

- Characterization and optimization of CNT-based devices
- Circuit design and simulation of CNT-based devices

The main focus of this international collaborated research programme was printed electronics, especially those on flexible substrate like plastic foil, which has been predicted with a great potential future market that covers a wide range of novel applications like wearable electronics, electronic newspapers, flexible displays, bendable solar panels, and radio frequency identification (RFID) tags, wherever the conventional silicon electronics can hardly be implemented due to the rigidity of silicon substrate. Printed electronics also enables high yield production in contrast to conventional silicon electronics which requires complex production steps. The largest segments of printed electronics would be transistors and memory. As mentioned before, CNTs as emerging research material have shown excellent electronic properties, along with mechanical bendability, flexibility, lightweight, and mechanical strength. Moreover, the long-term stability of CNT-based devices in ambient air and the relative low cost of them makes them superior to organic semiconducting molecules, another candidate for future printed electronics.

In the first phase of this research project, CNTFETs based on either individual CNT rope or CNT random network were delivered from the partner group in Singapore for characterization of the transistor performance in terms of mobility and on-off ratio. Then, based on the knowledge obtained from characterization of those sample devices, work was carried out towards the optimization of devices. Firstly, a solution-processable process was developed for fabrication of random network-based CNTFETs. The fabrication process was based on a drop-casting technique combined with shadow-mask

evaporation, which enabled simple, fast, and reliable production of CNTFETs. Commercial product of sorted CNT powders with high semiconductor enrichment were purchased and dissolved in organic solvent to create CNT suspensions, which then drop-cast on silicon substrate to form CNT random networks. The network density could be easily controlled via change of drop-cast liquid volume. Moreover, the drop-casting process could be considered as an approximation to the printing process, while the drop-casting technique requires no special printing machine and therefore suitable for study on prototypes.

As next step, a systematic study was carried out on a set of over hundred random network-based CNTFETs with variations in network density, semiconductor enrichment, and tube diameter. The CNTFETs were made via the solution-processable drop-casting process mentioned above. The aim of this systematic study was to investigate the influence of those parameters on the performance of CNTFETs in terms of mobility and on-off ratio, as mentioned in the overall objective of this research project, so that optimization of device performance could be achieved. In recent years, previous research works have studied the influence factors on performance of CNTFETs in various ways, including influence factors like network density [17]-[18], [21], semiconductor enrichment [21], channel length [8]-[9], and channel width [22]. The novelty of the performance analysis carried out in this study was to focus on the combined influence of network density and semiconductor enrichment. The results could lead to better understanding of device mechanism and provide guidance to further optimization of device performance.

In the simulation part of this research project, a theoretical model based on the Monte Carlo method was built for simulation of CNT random networks. In the model, CNTs were randomly generated according to a given semiconductor enrichment and within a defined channel area. The drain and source electrodes were placed on two parallel opposite sides of the simulated CNT network. After generation of the CNT random network, the resistance of junctions between each pair of CNTs in contact was identified according to the type of junctions. Considering the existence of both metallic and semiconducting species, the junction type could be one of the following three types: metallic-semiconducting, semiconducting-semiconducting, and metallic-metallic. The two homogeneous junctions were considered to have much lower contact resistance than the heterogeneous one. Thereafter, conducting paths were identified between both

electrodes across the channel. This theoretical model can simulate the current flow of CNT random network as a function of network density.

Scientific publications from this research project that relate to the part of fabrication and characterization of random network-based CNTFETs are listed in Appendix E.

## 1.2 About this thesis

This thesis is entitled “Fabrication and characterization of carbon nanotube random network transistors” and deals with the characterization and optimization part of results obtained from the research project as stated above. The main part of those results has been included in several scientific publications as listed in Appendix E. This thesis is divided in six chapters. The first chapter gives introduction to the background of CNT research, the research project towards the manufacturability of CNT-based printed electronics, and the scope of this thesis.

Chapter 2 gives an overview of the theoretical background related to this thesis. Section 2.1 provides a general view of the research progress on CNTs: firstly the various allotrope forms of element carbon from graphene to fullerenes; then the wide range of applications of CNTs in mechanical, optical, electronic, and radiofrequency fields; lastly the synthesis methods for CNTs like arc-discharge, laser ablation, and chemical vapor deposition (CVD). Section 2.2 discusses the cylindrical structure of CNTs with a focus on the chirality of single-walled species that has influence on their electronic types. The chirality system is explained with band structure diagram and density of states. Section 2.3 discusses the different kinds of CNTFETs based on individual CNT rope, aligned CNT array, or CNT random network. For rope-based or network-based CNTFETs, a schematic model, a short review of research progress, and microscopic images of prototype devices are included. Also included in this section are aspects relating to the CNTFETs in general, like *n*-doping of CNTs or the direction and alignment of CNT arrays.

Chapter 3 describes the solution-processable fabrication of random network-based CNTFETs that was developed in this study. Section 3.1 deals with the preparation of CNT suspension. The first part of this section summarizes the characteristics of

commercial CNT products purchased for this study, followed by an overview of various ways to create CNT suspension or solution with or without additional surfactants. Section 3.2 describes the deposition of CNT random networks from CNT suspensions. The first part of this section deals with the substrate preparation, including aspects relating to the functionalization of silicon substrate to increase the adhesion and homogeneity of deposited CNT random networks. The second part gives an overview of the printing and coating techniques. The last part explains the network density control via the drop-casting technique. Three terms have been used in this work to characterize the density of CNT random networks: network density ( $\text{mg}/\text{m}^2$ ), tube density ( $\text{tube}/\mu\text{m}^2$ ), and the equivalent CNT concentration ( $\text{mg}/\text{L}$ ). Section 3.3 deals with contacting the deposited CNT random networks with metal electrodes. Metal electrodes were thermally evaporated through a shadow-mask in a photoresist-free process. The second part of this section describes different transistor structures: the back-gated structure with a global back-gate; the bottom-gate and top-gate structures with local gate either at the bottom or on top of the CNT channel. CNTFETs made in this study were contacted with Pd/Au multilayer as electrodes and had a back-gated structure.

Chapter 4 deals with the characterization of random network-based CNTFETs. Section 4.1 describes the typical transistor characteristics of CNTFETs in general. Section 4.2 gives details about characterization of performance parameters including on-off ratio, transconductance, drain conductance, mobilities, threshold voltage, subthreshold swing, and frequency characteristics from the small-equivalent circuit. The characterization of random network-based CNTFETs was carried out on a conventional semiconductor characterization system mostly at room-temperature in ambient environment. To each performance parameter, the definition, measurement settings, and experimental results compared with literature are included. A discussion of the temperature dependence of transconductance characterization is also included. Section 4.3 discusses the Raman spectroscopy and its use in quality control of CNT random networks, including an introduction to the Raman spectra of SWNTs and confocal Raman imaging.

Chapter 5 contains the performance analysis based on a systematic study of over hundred random network-based CNTFETs made in this work. Section 5.1 explains the design of experiment. Section 5.2 discusses the influence factors on transistor performance in terms of drain current, on-off ratio and field-effect mobility. The influence factors discussed in this section includes network density, semiconductor

enrichment, and tube diameter. A new parameter, the metallic tube density, defined as network density multiplying metallic tube content, was introduced to express the co-influence of those two parameters. Section 5.3 deals with hysteresis, a generally undesired effect observed in transistor characteristics of CNTFETs. Experimental results, discussion on the origin of hysteresis, and treatments to depress this effect are included.

Chapter 6 concludes the whole work and gives outlook and suggestions for future work.

The Appendices include following parts: (a) description of the process steps that have been developed in this study on how to make a solution-processable random network-based CNTFET; (b) list of work functions including SWNT and common chemical elements that can be used as metal contacts; (c) list of symbols and (d) abbreviations and acronyms; and (e) list of publications.



## Chapter 2

# Carbon Nanotube as Electronic Material

The electronic properties of CNTs make them attractive to a wide range of applications like conducting coating for metallic species or channel material in transistors for semiconducting species. This chapter gives a basic theoretical background for CNT electronics with focus on those especially relevant to this thesis. In the previous chapter, challenges concerning CNT-based devices are listed in Fig. 1.1, including chirality, electronic types, doping, and direction. General view of those aspects is included in this chapter. Firstly, Section 2.1 provides an overview of the recent research progress on CNTs, including the synthesis and the diverse potential application fields of CNTs. Section 2.2 describes the structure and basic physical properties of CNTs. The first part of this section explains the chirality system that has been adopted to identify SWNTs. The second part discusses the electronic type of CNTs: metallic or semiconducting, based on the model of chirality system, band structure diagram, and density of states.

Section 2.3 focuses on the CNTFETs based on either individual CNT rope or CNT random network. Individual rope-based CNTFETs can be used as devices in nanometer-scale; while random network-based CNTFETs can be used in flexible electronics or as sensors. For each type of CNTFET, a schematic model, a general review of the research progress, and images of prototype devices are included. Various microscopic measurements have been taken on prototypes, including optical microscope, scanning electron microscope (SEM), field emission scanning electron microscope (FESEM),

atomic force microscope (AFM), three-dimensional AFM image, and confocal Raman image. The first part deals with the individual rope-based CNTFETs and also includes discussion about the  $n$ -doping of CNTFETs, which are intrinsically  $p$ -type. The second part deals with the random network-based CNTFETs but also includes discussion about the alignment of CNTs in comparison to CNT random networks. At the end of this part, an example of random network-based CNTFET as pH-sensor is also included.

## 2.1 Progress of carbon nanotube research

The carbon atom can form three types of covalent bonds depending on the hybridization of orbitals [23]. The  $sp^1$  hybridization has two  $\sigma$ -bonds separated by an angle of  $180^\circ$  and two  $\pi$ -bonds. The  $sp^2$  hybridization has three  $\sigma$ -bonds separated by an angle of  $120^\circ$  on the same plane and one  $\pi$ -bond. The  $sp^3$  hybridization has four  $\sigma$ -bonds separated by an angle of  $109.5^\circ$ . The tetrahedral form of the  $sp^3$  bonds is typical for diamond, the hardest substance known so far. The  $sp^2$  bonds are typical for graphite, while the single sheet of graphite is known as graphene which is formed by a hexagonal network of  $sp^2$  hybridized carbon atoms. Other than the insulating  $sp^3$  bonds, the  $sp^2$  bonds provide good electrical conductivity [23]. The third allotrope of carbon is known as fullerenes which also have  $sp^2$  bonds and can be in spheroidal form, known as buckyballs, or cylindrical form, known as carbon nanotubes. Fig. 2.1 shows the common structure of carbon allotropes like amorphous carbon, diamond, graphite, and fullerenes [24].

The tubular form of fullerenes, known as carbon nanotubes, can be either single-walled or coaxial multi-walled. The tube diameter of single-walled CNTs is typically around 1 nm, while the tube diameter of multi-walled CNTs can exceed 10 nm depending on number of walls [25]. The tube length of CNTs can vary from several micrometers to hundreds micrometers [26]. Generally, CNTs have a high aspect ratio that can be considered as quasi-one-dimensional.

As mentioned before, research on CNTs has shown many promising properties of them that create a wide range of potential applications. At the early stage of research, individual CNTs have been used as nanotweezers [27] or nanoprobe in scanning tunneling microscope (STM) [28], due to the nanometer scale and mechanical strength of



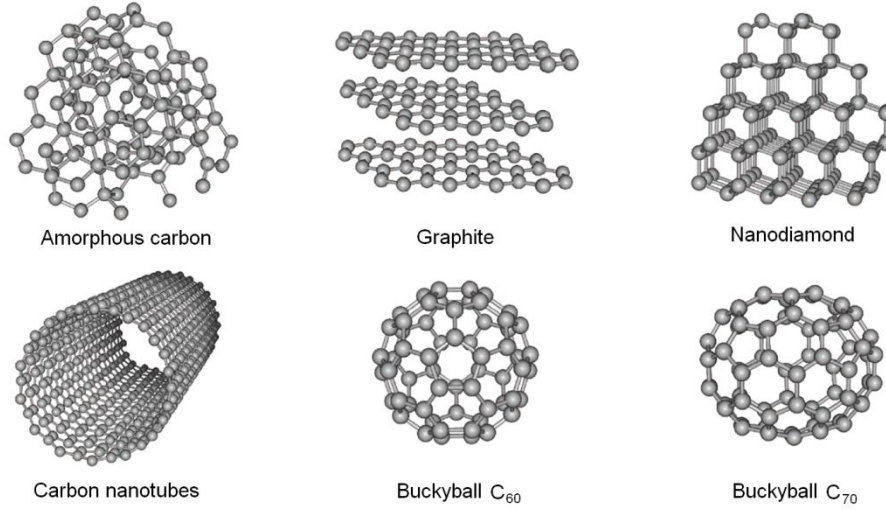


**Figure 2.1** Common structures of carbon allotropes. From left above: amorphous carbon, graphite (single sheet known as graphene), diamond, SWNT, and buckyballs  $C_{60}$  and  $C_{70}$  [24].

CNTs. The tubular structure of CNTs has been considered as possible storage for hydrogen, although later on under disputation [29]. The thin-films of CNTs have been demonstrated as transparent and conductive coating [4], due to the optical transmittance and electrical conductivity of CNTs. The electrical conductivity can be tuned to a dramatic switching behaviour that has been shown in CNTs with specific Y-junction, where mutual interaction of currents could lead to novel logic device [30]. From a single CNT, a radio receiver [31] and light-emitting diodes (LEDs) [32] has been realized, relying on the field-emission and light emission properties of CNTs, respectively. Aligned CNT arrays have been integrated into three-dimensional microelectromechanical systems [33]. Recently, the thermal conductivity of CNTs has shown potential in remote heating [5]. When longitudinally unzipped, CNTs can be cut into graphene nanoribbons (GNRs), a novel two-dimensional material [34]. As the research progresses, further novel applications can be expected. This work focuses on the application of CNTs as semiconducting channel material in FETs.

The synthesis of CNTs and especially SWNTs can be achieved via following three basic techniques: arc-discharge, laser ablation, and chemical vapor deposition [35]. The first observed CNTs were synthesized via arc-discharge method, which had long been applied for synthesis of fullerenes [1]-[2]. The arc-discharge technique creates CNTs by generating arc within a helium atmosphere between two graphite electrodes, while a mixture of metal catalysts filled in the graphite anode [36]. Commonly used metal

catalysts include various mixtures from Ni, Co, Y, and Fe [35]-[36]. The arc-discharge method generates CNTs with high yield, low cost, and high quality with relatively low content of residual catalyst.

The laser ablation technique was developed in 1996 [37]. The laser ablation method creates CNTs by placing a carbon target mixed with metal catalyst in a tube-furnace heated to above 1000 °C with inert gas flow and vaporizing the carbon target via pulsed laser [37]-[38]. Commonly used metal catalysts include various mixtures from Ni, Co, and Y [37]-[38]. CNTs generated by laser ablation method are mostly found in form of ropes [37]. The arc-discharge and laser ablation techniques are both based on the condensation of carbon atoms from solid carbon sources and therefore require a high temperature close to the melting temperature of graphite at around 3000–4000 °C [35].

The CVD technique was first introduced in 1998 [39]. CNTs are created by flowing hydrocarbon gas over metal catalyst nanoparticles placed in a tube-furnace [39]-[41]. The key factors to control the CVD process include the choice of hydrocarbon gas, catalyst, and growth temperature [35]. Commonly used hydrocarbon molecules include methane and ethylene, for instance; while commonly used metal catalysts include various mixtures from Fe, Ni, Co, and Mo [35], [39]-[40]. The CVD technique can enable controlled growth of CNTs on substrate in terms of selective position and direction [41]. A great advantage of CVD process in comparison to the other two processes is the lower temperature required that can be down to 800 °C [35]. Many variations of CVD process are known nowadays, such as the high-pressure carbon monoxide process (HiPCO).

## 2.2 Structure and properties of carbon nanotubes

### 2.2.1 Chirality of single-walled carbon nanotubes

The chirality system has been introduced to distinguish different types of SWNTs and generally includes following three types: armchair, zigzag, and chiral, as shown in Fig. 2.2a. SWNT can be considered as formed by rolling up a graphene sheet. Therefore, the chirality system is built on a graphene sheet as shown in Fig. 2.2b. The two unit vectors of this chirality system,  $\mathbf{a}_1$  and  $\mathbf{a}_2$ , both start from the zero point (0, 0) placed at one

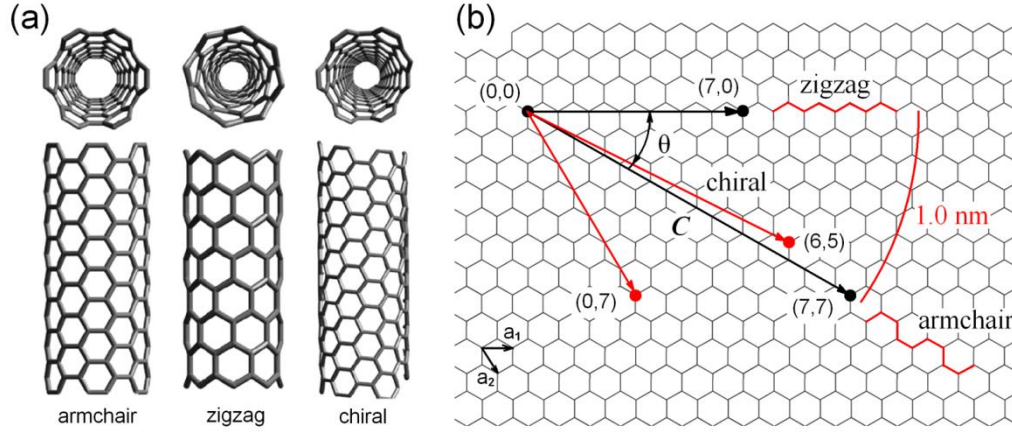


**Figure 2.2** Chirality of single-walled carbon nanotubes. (a) Three chirality types: armchair, zigzag, and chiral [42]. (b) Construction of single-walled carbon nanotube from a graphene sheet with the chiral vector  $C = na_1 + ma_2$ , where  $a_1$  and  $a_2$  are unit vectors of graphene lattice,  $(n, m)$  are chiral indices. The Chiral vector is perpendicular to the tube axis. A CNT with indices  $(n, m)$  is formed by rolling up the graphene sheet along the chiral vector and overlapping the zero point  $(0, 0)$  with the point  $(n, m)$ . The red arc shows the tube diameter of 1.0 nm. Zigzag CNTs have indices  $(n = m)$  and chiral angle  $\theta = 0^\circ$ , while armchair CNTs have indices  $(n, 0)$  and  $\theta = 30^\circ$ .

vertex of the hexagonal lattice, and end at two other vertices of the graphene lattice. The unit vectors have an angle of  $60^\circ$  between them and a unit length of  $2.46 \text{ \AA}$ , calculated from the minimum carbon-carbon distance  $a_{c-c} \approx 1.42 \text{ \AA}$  [23]. The two unit vectors therefore set up a coordinate system on the graphene sheet as shown in Fig. 2.2b. Within such a chirality system, a chiral vector  $C$  is then given as

$$C = na_1 + ma_2 \quad (2.01)$$

Where  $a_1$  and  $a_2$  are the unit vectors, and the numbers  $n$  and  $m$  are integers [23], [42]-[43]. The angle between the chiral vector and the horizontal axis is called the chiral angle  $\theta$ . The group  $(n, m)$  is called chiral indices used to identify the type of SWNT according to the chirality system. A nanotube is then formed by rolling up the graphene sheet along the chiral vector and overlapping the zero point  $(0, 0)$  with the chiral point  $(n, m)$ . The tube axis is then perpendicular to the chiral vector and the tube diameter  $d_t$  is given as

$$d_t = \frac{\sqrt{3}a_{c-c}(m^2+n^2+mn)^{1/2}}{\pi} \quad (2.02)$$

Where  $(n, m)$  are the chiral indices, and  $a_{c-c} \approx 1.42 \text{ \AA}$  [23]. For example, a  $(6, 5)$ -CNT has a tube diameter of *ca.* 0.8 nm, while a  $(7, 7)$ -CNT has a tube diameter of *ca.* 1.0 nm. The red arc in Fig. 2.2b marks the CNTs with a tube diameter of 1.0 nm.

From the three types of SWNTs, the zigzag tubes are those with a chiral vector along the unit vectors in the chirality system. The chiral indices are either  $(n, 0)$  or  $(0, m)$ . For instance, the  $(7, 0)$ -CNT or the  $(0, 7)$ -CNT shown in Fig. 2.2b are zigzag. They have a zigzag profile as shown in Fig. 2.2, thus the name. The chiral angle is  $\theta = 0^\circ$  or  $\theta = 60^\circ$ . The armchair tubes are those with two equal chiral indices  $(n, m = n)$ . They have a chiral angle of  $\theta = 30^\circ$ . For instance, the  $(7, 7)$ -CNT shown in Fig. 2.2b is armchair. The armchair tubes have a profile similar to the armchair as shown in Fig. 2.2, thus the name. All the other tubes are called chiral, with a chiral angle between  $0^\circ$  and  $30^\circ$ , or between  $30^\circ$  and  $60^\circ$ . The chiral indices are  $(n, m \neq n)$ . For instance, the  $(6, 5)$ -CNT shown in Figure 2.2b is chiral. Most SWNTs are chiral. The chiral indices of a SWNT can be experimentally determined via measurements on the chiral angle and tube diameter.

The chirality system describes the geometrical structure of SWNTs and can be related to the electronic type of CNTs. As mentioned before, SWNTs can be either metallic or semiconducting. Prior research has revealed the relation between the chirality system and electronic type of CNTs, obtained from the theoretical model on the energy boundary conditions in the circumferential direction of CNT and proven by experimental results observed on diverse samples [43]. As a general rule, CNTs are metallic when  $|n - m| = 3i$ , where  $n, m, i$  are all integrals. Therefore, the armchair CNTs are all metallic, while the zigzag and chiral CNTs can be either metallic or semiconducting depending on their chiral indices. As an example, the  $(7, 7)$ -CNT is metallic, while the  $(7, 0)$ -CNT and  $(6, 5)$ -CNT shown in Fig. 2.2b are both semiconducting. Following this rule, about one-third of all the as-grown SWNTs are expected to be metallic. The rule also shows that for those CNTs with similar tube diameter but different chiral indices, their electronic type can also be different. More about the electronic type of SWNTs are given in next section.

### 2.2.2 *Electronic type of single-walled carbon nanotubes*

Single-walled CNTs can be either metallic or semiconducting. Similar to intrinsic graphene, the metallic CNTs have no band gap in comparison to the semiconducting species. The conductivity of semiconducting species can be switched on and off under the control of external voltage bias; while the conductivity of metallic species cannot be effectively varied via external bias. Therefore, semiconducting CNTs are considered to be

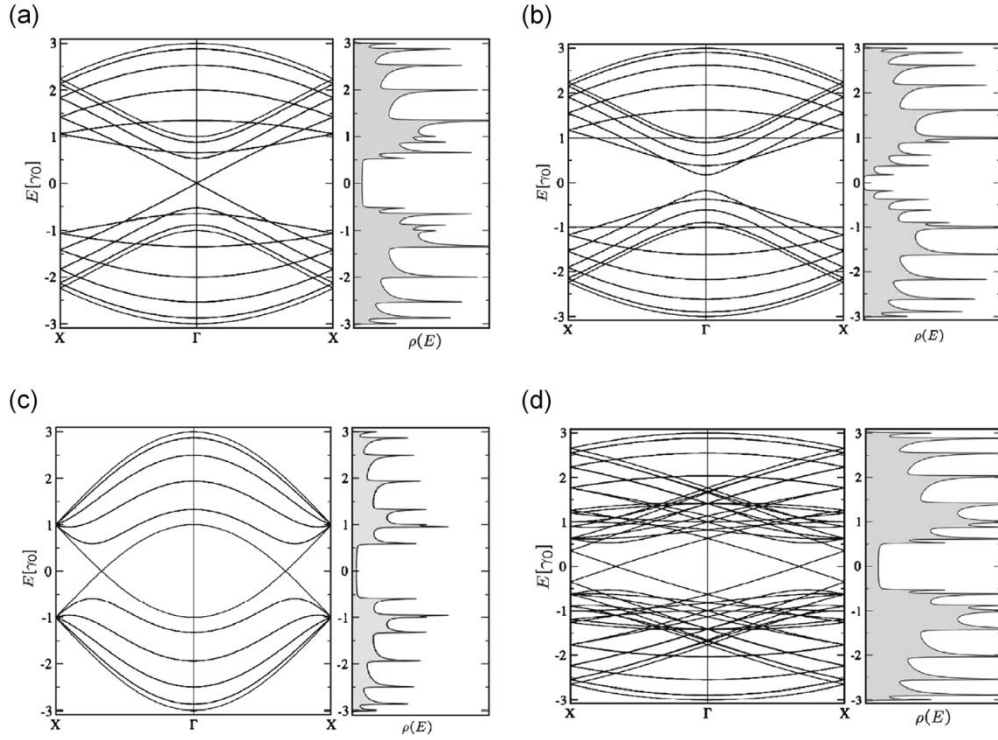


**Figure 2.3** Band structure and density of states from the zone-folding model [45]. The band structures are plotted along the X- $\Gamma$ -X direction with the Fermi surface located at  $\Gamma$  (X and  $\Gamma$  are points in the Brillouin zone). Band energy  $E$  is scaled with  $\gamma_0 \approx 2.9$  eV (the minimum carbon-carbon overlap energy), while the Fermi energy located at zero. Density of state  $\rho$  is plotted as a function of band energy. (a) Zigzag (9, 0) with no band gap, metallic. (b) Zigzag (10, 0) with band gap and no state at the Fermi level, semiconducting. (c) Armchair (5, 5) with overlapped conduction and valence bands, metallic. (d) Chiral (8, 2) with overlapped energy bands, metallic.

promising candidate for novel semiconducting devices; while metallic CNTs with their excellent conductivity can be used as novel conducting material.

The electronic types of SWNTs can be identified from the electronic band structure or from the density of states (DOS). Fig. 2.3 gives four examples concerning the chirality system and theoretical calculation based on a zone-folding approximation of a tight-binding model [45]. Fig. 2.3a is the simulated results for a (9, 0)-CNT, while Fig. 2.3b for a (10, 0)-CNT. Both tubes are zigzag. The former one is metallic, while the latter one is semiconducting which for instance can be seen from the band gap in the band structure diagram. Fig. 2.3c is an armchair (5, 5)-CNT and Fig. 2.3d is a chiral (8, 2)-CNT, both are metallic. Those four CNTs have similar tube diameter around 0.7 nm.

The band structure diagram is plotted along the X- $\Gamma$ -X direction of the Brillouin zone, where  $\Gamma$  is the central point of the Brillouin zone and X is on the zone edge [45]. The

Fermi surface is located at  $\Gamma$ . The energy level is scaled with the minimum carbon-carbon overlap energy of  $\gamma_0 \approx 2.9$  eV, while the Fermi energy located at the zero point. As shown in Fig. 2.3, the conduction and valence states both include several energy bands. The conduction bands are located above the Fermi level, while the valence bands are below the Fermi level. As mentioned before, the electronic type of CNTs can then be seen from the band gap between conduction and valence bands. For metallic CNTs, the conduction and valence bands cross each other or meet exactly at the Fermi level with no band gap; while for semiconducting CNTs, the conduction and valence bands have a small energy gap between them. Moreover, CNTs with different geometrical structure (zigzag, armchair, or chiral) also have different shapes of band structures, as illustrated in Fig. 2.3. The band gap  $E_{\text{gap}}$  of semiconducting CNTs has been known as approximately inversely proportional to the tube diameter, as given by

$$E_{\text{gap}} = \frac{2\gamma_0 \cdot a_{\text{c-c}}}{d_t} \approx \frac{0.82}{d_t} \quad (2.03)$$

Where  $\gamma_0$  is the minimum carbon-carbon overlap energy,  $a_{\text{c-c}}$  is the minimum carbon-carbon distance, and  $d_t$  is the tube diameter [43]. For example, semiconducting CNTs with a tube diameter of 0.8 nm have an energy band gap of *ca.* 1.0 eV, while those with a tube diameter of 1.4 nm have a band gap of *ca.* 0.6 eV.

The density of states  $\rho$  represents the density of available states at a certain energy level and can be calculated from a zone-folding mode by counting the number of available states for an infinite small interval of band energy [45]. Alternatively, the density of states can be experimentally determined by measuring the conductance  $dI/dV$  on a CNT or the normalized value of  $(dI/dV) / (I/V)$  [43]. Fig. 2.3 gives four examples plotted as a function of band energy  $E$ , while the Fermi level placed at the zero point of band energy [45]. The sharp peaks in the density curves correspond to the van Hove singularities, resulted by the limitation in the directions perpendicular to tube axis due to the one-dimensional shape of CNTs [43], [45]. The electronic types of CNTs can be identified from the available states at the Fermi level. The semiconducting CNTs have none states at the Fermi level due to the band gap between conduction and valence bands; while the metallic tubes have overlapped conduction and valence bands and thus a certain density of states at the Fermi level as shown in Fig. 2.3. For the three metallic tubes in Fig. 2.3, a secondary gap can be seen. The secondary gap is typically wide and above 1.0 eV, while the primary gap relating to the semiconducting type is typically below 1.0 eV [43].

## 2.3 Carbon nanotube field-effect transistors

### 2.3.1 Individual rope-based carbon nanotube transistors

An individual rope-based CNTFET contains a single tube or rope of CNT as semiconducting channel between electrodes. Various material have been used as substrate for CNTFETs like silicon, quartz, or flexible plastics such as polyimide (PI) [22], polyethylene terephthalate (PET) [9], and polyethylene naphthalate (PEN) [46]. In the early phase research, CNT has been placed above pre-patterned electrodes, obtaining only weak contact between CNT and underlying metal electrodes [47]. The later form of CNTFETs mainly has CNTs placed below electrodes to improve the metal-semiconductor contact. In some case, the substrate can serve as a back-gate, for instance highly doped silicon substrate [48]. Otherwise, a local gate electrode is placed above or below the CNT channel, which is called top-gate [49] or bottom-gate [50], respectively. A novel gate structure wrapping around the CNT channel has also been demonstrated in prior research [51]. Moreover, the gate control efficiency can be enhanced by applying local gate electrode with a thin-film high- $\kappa$  dielectric like  $\text{HfO}_2$  ( $\kappa_{\text{ox}} = 16$ ) or  $\text{ZrO}_2$  ( $\kappa_{\text{ox}} = 19.8$ ) [52].

The performance of individual rope-based CNTFETs has been demonstrated as comparable with conventional metal-oxide-semiconductor field-effect transistors (MOSFETs) based on silicon substrate, for instance with subthreshold swing below 100 mV/dec and on-off ratio up to  $10^5$  [49]-[50]. Another advantage of rope-based CNTFETs is the possibility for ballistic transport. Individual rope-based CNTFETs have nanometer-scale channel that can be scaled down to sub-10 nm [53], while the mean free path of charge carriers in CNT is *ca.* 500 nm at room-temperature [13]. Therefore, ballistic transport can be realized in CNTFETs with channel length smaller than the mean free path of charge carriers. The quantum limit of resistance in single CNT is given by

$$R_q = \frac{h}{4q^2} \approx 6.5 \text{ k}\Omega \quad (2.04)$$

Where  $R_q$  is the quantum limit,  $h = 6.626 \times 10^{-34}$  J·s the Planck's constant, and  $q = 1.602 \times 10^{-19}$  C the elemental electronic charge [13].

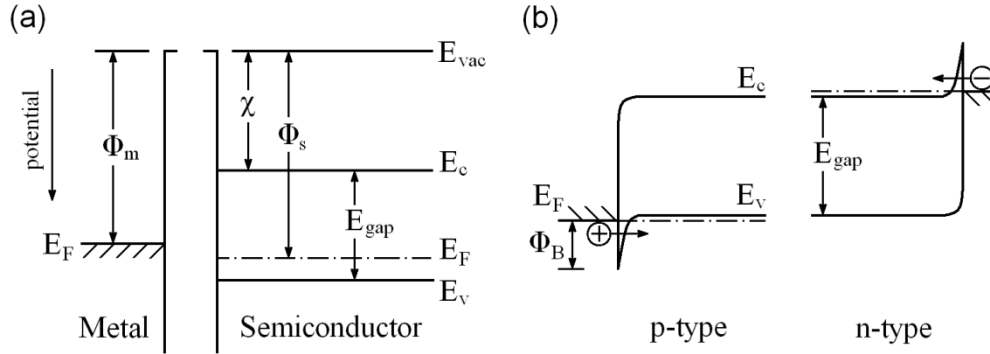


**Figure 2.4** Schematic band diagram of metal-semiconductor contacts: (a) Flat bands with mismatching metal and semiconductor bands before into contact ( $E_{vac}$  is the vacuum level,  $E_F$  the Fermi level,  $E_c$  the conduction band edge,  $E_v$  the valence band edge,  $E_{gap}$  the band gap,  $\Phi_s$  the semiconductor work function,  $\Phi_m$  the metal work function,  $\chi$  the electron affinity of semiconductor). (b) Bent bands after contact with energy barrier at the metal-semiconductor interfaces for  $p$ - and  $n$ -type semiconductors, respectively ( $\Phi_B$  is the barrier height). In  $p$ -type semiconductor, holes tunnel through the energy barrier under negative bias; while in  $n$ -type semiconductor, electrons tunnel through the energy barrier under positive bias.

As mentioned before, CNTFETs are intrinsically  $p$ -type with holes as majority charge carriers. The semiconducting channel is turned on under negative bias. The  $p$ -type characteristics of CNTFETs are due to the absorption of oxygen on CNTs, therefore  $n$ -doping can be realized via polymer functionalization [54], annealing in vacuum [55] or in hydrogen atmosphere [49], and doping with potassium as an electron donor [47]. Polyethylene imine (PEI) has been used to functionalize CNTFETs that provides air-stable  $n$ -type characteristics [54]. Annealing in vacuum or in hydrogen atmosphere can lead to desorption of oxygen from CNTs and change of CNTFET into  $n$ -type. However, CNTFETs return to  $p$ -type when exposed in air. Therefore, the channel area of converted CNTFETs has to be covered with an insulation layer to remain  $n$ -type under ambient conditions, for instance covered with polymethylmetacrylate (PMMA) [47]. In this way, CMOS logic gate like inverter has been realized based on either one single CNT [47] or a couple of  $p$ -/ $n$ -CNTFETs [49]. However, doping control of CNTs is still under investigation.

To contact the CNT channel, various metals has been used in research, including gold [47], molybdenum [49], titanium [48], and palladium [50]. The mismatch of work functions at the metal-semiconductor interface is known as the Schottky barrier that creates nonlinear and rectifying contact [3], [56]. Fig. 2.4 shows a schematic band



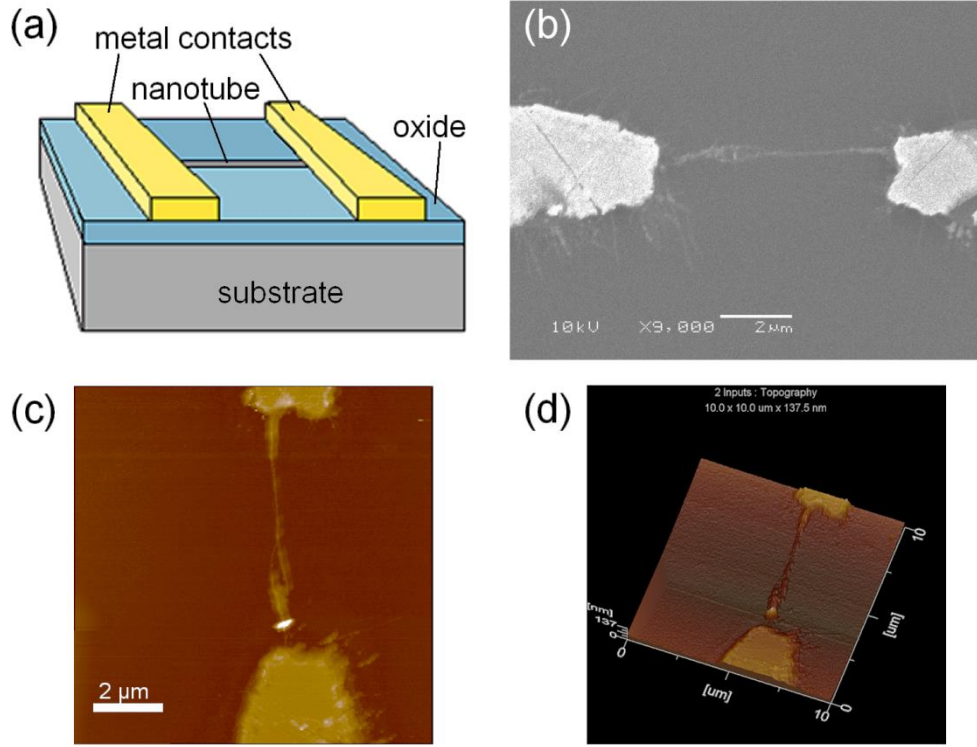


**Figure 2.5** Individual rope-based carbon nanotube transistors. (a) Schematic diagram of back-gated rope transistor with silicon substrate as back-gate and CNT rope lying between and below two electrodes. (b) SEM image of a rope-based CNTFET with channel length of 7  $\mu\text{m}$  (scale bar: 2  $\mu\text{m}$ ), (c) AFM image of the same CNTFET (scale bar: 2  $\mu\text{m}$ ), and (d) three-dimensional AFM image (scan size: 10  $\mu\text{m}$  x 10  $\mu\text{m}$ ).

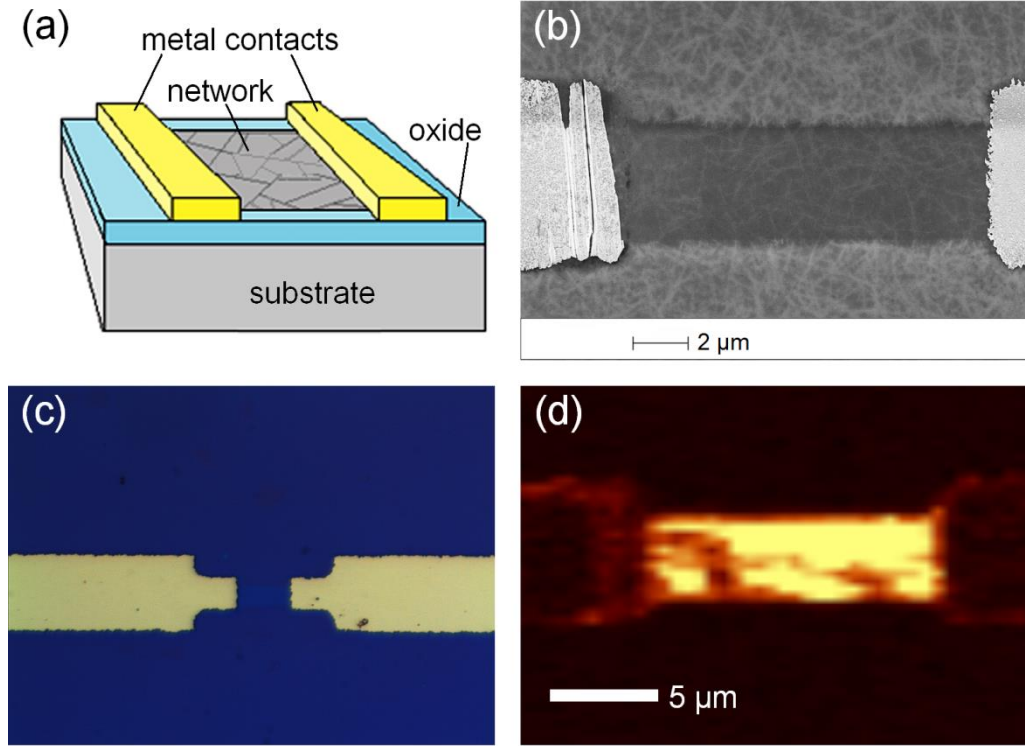
diagram of metal-semiconductor contacts [56]. Fig. 2.4a is the flat band diagrams of semiconductor and metal before contact. The work function is defined as the difference between the vacuum level and the Fermi level. The electron affinity of the semiconductor is the difference between the vacuum level and the conduction band. The band gap of semiconductor is the difference between the conduction and valence bands. When get into contact, the energy bands are bent and build barrier at the metal-semiconductor interface, as shown in Fig. 2.4b. In *p*-type semiconductor, the edge of valence band is bent near the Fermi level and the energy barrier becomes thinner under negative bias that holes can tunnel through to create current flow. In *n*-type semiconductor, the energy barrier is formed at the edge of conducting band that electrons can tunnel through under positive bias. The work function of CNT and common metals can be found in Appendix B [57]-[58]. Moreover, graphene and metallic CNTs have also been used as contacts in CNTFETs [9], [18]. The geometry of electrodes also has influence on the device performance [59].

Fig. 2.5 gives an example of rope-based CNTFET with a channel length of 7  $\mu\text{m}$ . The CNT rope was grown on silicon substrate via CVD process, and then contacted with metal electrodes. The silicon substrate with thermally grown  $\text{SiO}_2$  layer serves as the back-gate. The CNT rope has a rope diameter in nanometer-scale and can be seen in both SEM and AFM images.

### 2.3.2 *Random network-based carbon nanotube transistors*

A random network-based CNTFET has a CNT random network as the semiconducting channel instead of one single semiconducting CNT. With a larger scale than single CNT, CNT random network as conducting channel can be more easily placed at desired spot or shaped to required form between electrodes. The CNT random networks can be directly grown on substrate, or deposited from CNT solution, or transfer-printed to desired substrate. The CNT random networks are flexible, stretchable, stable in air, and transparent in both visible and infrared range [4]. Moreover, the network out of one-dimensional CNTs can be used as sensor for detection of objects with size down to nanometer scale, like gas molecules [60], chemical compounds [6], and biomolecules [7].

Generally, a CNT random network can be considered as a thin film with mixed CNTs containing both semiconducting and metallic species. The semiconducting tube content can vary from two-third for as-grown CNTs to 99+% for well sorted CNTs. The metallic CNTs within a random network, although they might contribute to the improvement of conductivity, can degrade the transistor performance. For instance, the random network-based CNTFETs can have an on-off ratio up to  $10^4$  [17], lower than tube-based CNTFETs. The degradation in on-off ratio can be resulted by the heterogeneous contact resistance at a semiconducting-metallic tube junction, which is higher than the contact resistance at a homogenous tube junction of same species and limits the on-current [82]. Also, unlike semiconducting tubes, metallic tubes cannot be switched off via external voltage, thus result in higher off-current. Generally, well sorted CNTs with semiconductor enrichment up to 99% have been used in random network-based CNTFETs [8]-[9]. Alternatively, as-grown CNT random networks can be etched into stripes to depress the influence of metallic species in network [22].



**Figure 2.6** Random network-based carbon nanotube transistors. (a) Schematic diagram of a back-gated network transistor with silicon substrate as back-gate. (b) FESEM image of a network-based CNTFET with channel length of 12  $\mu\text{m}$  and channel width of 4  $\mu\text{m}$  (scale bar: 2  $\mu\text{m}$ ). (c) Optical microscope image of a CNTFET with similar channel geometry. (d) Confocal Raman image (scale bar: 5  $\mu\text{m}$ ).

Fig. 2.6 gives an example of random network-based CNTFET with a channel length of 12  $\mu\text{m}$  and channel width of 4  $\mu\text{m}$ . The CNT random network is placed between and below the metal electrodes, while the silicon substrate serves as a back-gate, as shown in the schematic diagram in Fig. 2.6a. The CNT channel is clearly visible in the FESEM, optical microscope, and confocal Raman images. The back-gate structure is often used for prototypes because no separate delicate gate structure is required. This thesis focuses on the fabrication and characterization of random network-based CNTFETs and performance analysis based on a set of CNTFETs. More details are included in the following chapters.

In addition to CNT random networks, aligned CNT arrays have also been used as semiconducting channel in CNTFETs. The alignment can be achieved via various techniques, including the Langmuir-Blodgett coating [61]-[62], spin-coating [63], fluidic channel method [64], dielectrophoresis (DEP) [65], and guided growth in horizontal or vertical directions [66]-[68]. A combination of the Langmuir-Blodgett method with

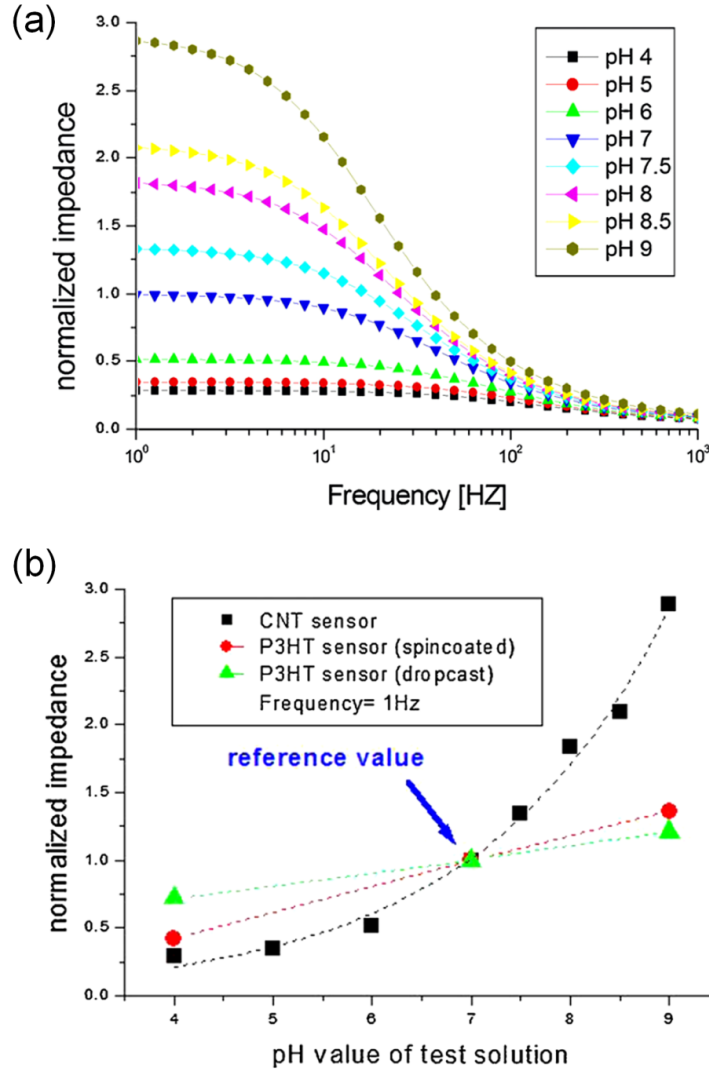


**Figure 2.7** Carbon nanotube random network transistors as impedimetric pH-sensor [19]. (a) Normalized impedance as a function of frequency, measured with pH-value from 4 to 9 (from bottom to top). (b) Comparison of pH-sensitivity of CNTFET with drop-cast and spin-coated P3HT sensor. Impedance normalized to reference value and plotted as a function of pH-value from 4 to 9, measured at the frequency of 1 Hz.

evaporation control can even create aligned CNT arrays in stripes [62]. The fluidic method aligns CNTs by flowing CNT suspension through a fluidic channel over patterned substrate surface [64]. The dielectrophoresis method is applicable for metallic CNTs [65]. Guided growth of CNTs on crystalline quartz creates horizontal alignment [66]; while water-assisted CVD growth enables vertical alignment of CNTs [68]. The aligned CNT arrays can be transferred to desired substrate via transfer-printing [67]-[68].

Recent researches have shown potential applications for random network-based CNTFETs in various fields like flexible electronics [17], radio frequency technique [18],

chemical and bio-sensors [19]. As an example, random network-based CNTFETs have been used as novel impedimetric pH-sensor by drop-casting test solution on CNT network [19]. Fig. 2.7 shows characteristics and comparison of different pH-sensors. In Fig. 2.7a, the normalized impedance is plotted as a function of frequency varied from 1 Hz to 1 kHz. The pH-value varies from 4 to 9. Generally, the impedance and sensitivity increase with increasing pH-value; while the sensitivity also increases with decreasing frequency. As a result, the impedimetric sensor is more sensitive in alkaline solution and measured at low frequency. Fig. 2.7b shows performance comparison of CNT sensor with organic sensors made from poly (3-hexylthiophene) (P3HT). The normalized impedance is plotted as a function of pH-value from 4 to 9, measured at 1 Hz. Generally, the CNT sensor has a larger slope than the P3HT sensors, indicating a higher sensitivity of CNTs in comparison to the organic polymer.



## Chapter 3

# Fabrication of Carbon Nanotube Random Network Transistors

The fabrication process of random network-based carbon nanotube transistors generally includes following three steps: preparing the substrate, distributing carbon nanotube network on substrate, and contacting nanotube network. Depending on application purpose, further steps can be added to the basic process, for instance transfer printing, encapsulation, isolation, and functionalization.

Construction of CNT networks with high quality is a crucial step to the whole process. Therefore, various approaches have been developed from various research groups so far, for instance direct growth on substrate, transfer printing, and solution-based process with pre-purified CNTs. This thesis mainly focuses on the last approach. Comparing with direct growth, solution-based process requires no extra high temperature. In addition, pre-purified CNTs, which can be purchased commercially, have such high quality in terms of semiconductor-enrichment and purity that can hardly be obtained by direct growth. In comparison with the transfer printing, where also pre-purified CNTs can be applied, distribution from CNT solution has the advantage of being quick and easy to apply and requiring less process steps. Again, there are various solution-based distributing approaches that have been developed and used in research. A general review is given in Section 3.2, together with detailed description of the drop-casting process used in this

study. The drop-casting process developed in this study also enables direct control of network density, providing basis for the performance analysis discussed in Chapter 5. A further part of Section 3.2 gives an overview on how to prepare substrate for CNT distribution with a focus on silicon substrate (covered with thermally grown oxide) that has been used in this study.

As mentioned before, pre-purified semiconductor-enriched CNTs used in this study were purchased from commercial producer. Section 3.1 gives an overview of physical properties of the purchased CNT products and the preparation of CNT solutions based on them. A general discussion about the solubility of single-walled CNTs is also included.

Finally, Section 3.3 describes different ways to contact CNT random networks, giving various device layouts that have been used by other research groups, and with a focus on the back-gate structure that have been used in this study. An important point relating to the choice of transistor structures is the availability of suitable gate insulator. Concerning the source/drain contacts, a general discussion about choosing suitable metal is also included in this Section.

## 3.1 Preparation of carbon nanotube suspension

### 3.1.1 *Semiconductor-enriched carbon nanotubes*

As-grown carbon nanotubes usually contain both metallic and semiconducting species, typically one-third metallic when estimated from the chirality theory [45]. Semiconducting CNTs can be electrically switched on and off via an external electrical field. The conductance of semiconducting CNTs is thus controllable similar to conventional semiconductors. In opposite to semiconducting species, the conductance of metallic CNTs cannot be significantly altered via external electrical field. Thus metallic species are comparable with conventional conductor. When used as channel material in field-effect transistors, the metallic tube content of CNT random network has to be minimized. Despite the large current density that can be carried by metallic CNTs, their existence of metallic species in CNT random networks can significantly degrade the on-off ratio of CNTFETs. When CNT network becomes dense, metallic tubes can build short



**TABLE 3.1**  
COMMERCIAL CARBON NANOTUBE PRODUCTS

Property	SG65	IsoNanotubes-S
Synthesis	CoMoCAT CVD	Arc discharge
Diameter range	0.7 – 0.9 nm	1.2 – 1.7 nm
Average tube diameter	0.8 nm	1.4 nm
Length range	450 nm – 2 $\mu$ m	100 nm – 4 $\mu$ m
Average tube length	0.9 $\mu$ m	1.0 $\mu$ m
Catalyst impurity	N.A.	ca. 0.5% by mass
Carbonaceous impurity	N.A.	< 5% by mass
Carbon content	> 90% by weight	ca. 99% by mass
SWNT content	80%	> 95%
Chirality	> 50% (6, 5)	N.A.
Semiconducting CNT content	> 90%	90%, 95%, 98%, 99+%
Suspension color	black	pink

Cited from the technical data sheets for SWeNT and NanoIntegris

paths between metal contacts. Moreover, metallic species have dominance in a mixed CNT random network and are less influenced by gate control.

In recent years, various approaches have been developed to separate mixed as-grown CNTs, such as selective destruction, chemical separation, and selective growth [69]. Electrical breakdown is one of the most mentioned selective destruction methods [70]. Metallic nanotubes are burned out via extremely large current, whereas semiconducting tubes are switched off via gate control and protected from electrical destruction. Electrical breakdown has the advantage of being easily operated, but lacks on the possibility of precise control, high yield, and flexibility. Moreover, extremely large current used in destructive process might cause damage to devices. Another widely adopted technique is the DGU process, which enables separation via selective chemical functionalization [20]. In this way, as-grown CNTs are non-covalently functionalized with surfactants and then dispensed in solution. Depending on their tube diameter, functionalized CNTs have

different buoyant densities thus can be sorted via ultracentrifugation. Therefore, electronic type enrichment can be achieved by carefully choosing source material and combining surfactants. The DGU technique enables production of purified and sorted CNTs with high yield and semiconductor enrichment up to 99%.

In this work, two kinds of commercial semiconductor-enriched CNT products were used for CNTFETs: SG65 CNTs from SWeNT and IsoNanotubes-S CNTs from NanoIntegris. Table 3.1 lists typical properties of SG65 and IsoNanotubes-S CNTs, according to the technical data sheets provided by producers. The SG65 CNTs were synthesized via a selective CVD process with combination of Co-Mo catalyst (CoMoCAT) that a narrow chirality distribution can be obtained [71]. Purified SG65 CNTs were 90%-semiconducting (90%-sc) with more than 50% tubes obtaining (6, 5)-chirality. The average tube diameter was 0.8 nm, while the average tube length was 900 nm. The IsoNanotubes-S CNTs were synthesized through arc-discharge process and then sorted via DGU. The average tube diameter was 1.4 nm, and the average tube length was 1.0  $\mu\text{m}$ . A range of semiconductor enrichment from 90%-sc to over 99%-sc was available. In addition, the carbon content and SWNT content of IsoNanotubes-S CNTs were higher than SG65 CNTs.

Moreover, the properties of commercial CNT products have been characterized via following measurements: the optical absorbance spectra, thermogravimetric analysis (TGA), and Raman spectra. The optical absorbance spectra are used to measure the electronic type enrichment of sorted CNTs [72]. Both SG65 and IsoNanotubes-S CNTs have strong absorbance peaks in semiconducting spectral range along with high semiconducting-to-metallic ratios [73]. The thermogravimetric analysis (TGA) curves are used to measure the impurity content, including carbonaceous impurities, residual catalyst, and residual surfactant. The IsoNanotubes-S CNTs have much smaller residual mass content (*ca.* 1%) than the SG65 CNTs (*ca.* 10%). The Raman spectra of CNTs are used to measure the content of amorphous carbon in term of the G/D ratio [74]. The G-band represents intensity of CNT content, while the disorder-induced D-band represents intensity of carbonaceous impurities such as amorphous carbon or damaged CNTs. Section 4.3 will give more details of the Raman spectroscopy and its use in characterization of the quality of CNTs.

### 3.1.2 Solubility of single-walled carbon nanotubes

As mentioned in Chapter 2, carbon nanotube can be considered as roll-up of a single atomic layer, which means the sidewall of CNT is smooth. When distributed in liquid, the smooth sidewall of CNTs makes them easy to bond together via the van der Waals interactions between tubes. Furthermore, the length of CNTs, typically in micrometer range, adds more difficulty to the attempt of dissolving them in common solvents. Research has shown limited solubility of SWNTs at room-temperature in several organic solvents, including 1,2-dichlorobenzene (DCB), *N*-methylpyrrolidinone (NMP), dimethylformamide (DMF), chloroform, and methanol [75]. The SWNT solution was prepared by applying sufficient sonication, which could exfoliate SWNT bundles into small ropes or eventually individual tubes. The room-temperature solubility of SWNTs has been found to be 95 mg/L in DCB, 31 mg/L in chloroform, and 10 mg/L in NMP [75]. The stability of such CNT solutions has been observed to vary from several hours to several days [75]. After that time, dissolved CNTs eventually formed larger bundles.

Although CNTs can be dissolved in organic solvents with limited solubility, they cannot be dispersed in aqueous solution without additional treatment. Prior research has shown several approaches to obtain aqueous solution of CNTs with improved solubility and stability via various surfactants and biomolecules functionalized to bare CNTs [42], [76]. By adding non-covalently bonded surfactants or wrapping polymers, individual CNTs could be effectively exfoliated from large bundles. Commonly used surfactants include sodium dodecyl sulfate (SDS), sodium dodecyl benzene sulphonate (SDBS), sodium cholate, and sodium deoxycholate [20]. Commonly used wrapping polymers include deoxyribonucleic acid (DNA), oligonucleotides, lignin, chitosan, and cellulose [77]. According to the technical data sheet for IsoNanotubes-S CNTs, which are also available in solution form functionalized with surfactants, the stability of functionalized CNT solution can last several months. However, after deposition of CNT random networks, surfactants have to be removed, for instance being rinsed with organic solvent or etched by acid.

Comparing above stated two approaches, purchased CNT powder was dissolved in organic solvent without additional surfactant in this study due to following considerations. Firstly, surfactants and additional removal step required by functionalized CNTs could cause contamination to deposited CNT random networks. Secondly, although the

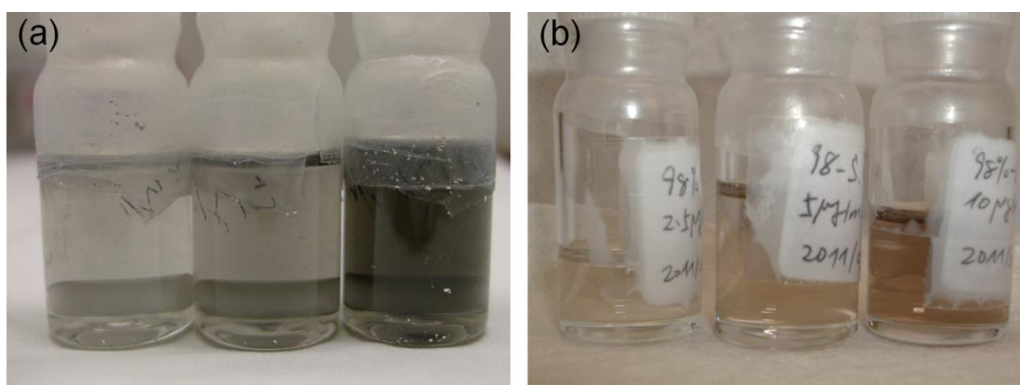


**Figure 3.1** Carbon nanotube suspensions (dissolved in NMP without additional surfactants). The CNT suspensions shown in both images have following concentrations: 2.5 mg/L, 5 mg/L, and 10 mg/L (from left to right). (a) 90%-sc SG65 CNT suspensions (black color). (b) 98%-sc IsoNanotubes-S CNT suspensions (pink color).

solubility of CNTs in organic solvent was low, it was acceptable to form random networks with adequate network density, as shown in Section 3.2. Moreover, increased network density could be achieved via repeated deposition steps. Finally, despite the short stability in organic solvent, CNT solution could be sonicated again before each use and thus not limited by the shelf life of surfactants.

In this study, semiconductor-enriched CNT powders (SG65 and IsoNanotubes-S) were dissolved in NMP (Merck, spectrophotometric grade, purity 99.5+%, through 0.2  $\mu\text{m}$  filter). The semiconductor enrichment was 90% and 98% for IsoNanotubes-S CNTs, and 90% for SG65 CNTs. Prepared CNT suspensions were sonicated in ice bath for *ca.* 90 minutes, until no more particles were visible and the suspensions were optically transparent. The CNT/NMP suspensions were firstly prepared with CNT concentration of 10 mg/L, and then diluted to 5 mg/L and 2.5 mg/L to form concentration gradation. The stability of CNT suspensions were several hours after sufficient sonication. After that time, dissolved IsoNanotubes-S CNTs began to form visible large bundles in middle of the suspension, whereas SG65 CNTs lay down on bottom of container. The difference between them could be due to the different impurity content that resulted in different density. The prepared CNT/NMP suspensions were kept in glass container and were to be well sonicated before each use. Fig. 3.1 shows images of CNT/NMP suspensions from SG65 and IsoNanotubes-S CNTs, each with concentration gradation from 2.5 mg/L to 10 mg/L. As shown in Fig. 3.1a, the SG65 CNT suspensions have black colour, whereas the colour of IsoNanotubes-S CNT suspensions are pink, as shown in Fig. 3.1b. Prior

research works have noticed the colour variation of SWNTs depending on tube diameter and electronic type [20], [73]. For instance, according to the technical data sheet for IsoNanotubes-S CNTs, the solution of semiconducting tubes has pink colour, whereas the solution of metallic tubes has green colour. The colour of CNTs has been considered to be due to the boundary conditions of cylindrical CNT structure in circumferential direction [73]. The black colour of CNT suspension could be due to the mixture of metallic and semiconducting species or due to the impurity content. As a result, the following experiment part was largely focused on the IsoNanotubes-S CNTs with higher purity, whereas the SG65 CNTs were mainly used as reference in comparison of the influence of tube diameter on transistor performance, as discussed in Section 5.2.3.

## 3.2 Deposition of carbon nanotube random network

### 3.2.1 *Substrate preparation*

As mentioned before, construction of CNT random network on desired substrate can be realized via various approaches: direct growth of CNTs on substrate, transfer printing of ready-made CNT random networks onto substrate, and deposition from CNT solutions. As mentioned in Chapter 2, CVD process has been commonly used to grow CNTs on desired substrate. The growth of CNTs via CVD requires extreme high temperature ranged from 700 °C to 1000 °C [39]-[41]. Therefore, only substrates that can tolerate such high temperature treatment can be used. Furthermore, catalysts used in CVD process have to be removed after growth of CNTs, which requires additional removal step and can cause contamination to the CNT networks. Another point is the selective growth of CNTs with certain electronic type, which remains an unsolved issue. Although a striping technique could be applied to depress the influence of metallic tubes [22]. Transfer printing has been used to transfer ready-made CNT networks to desired substrate [67], [78]. The transferred random networks thus can be pre-purified, adequately shaped, and properly selected with certain electronic types. The transfer printing process generally requires much lower temperature than CVD growth, thus can also be applied to flexible substrates which cannot withstand high temperature. Comparing to transfer printing,

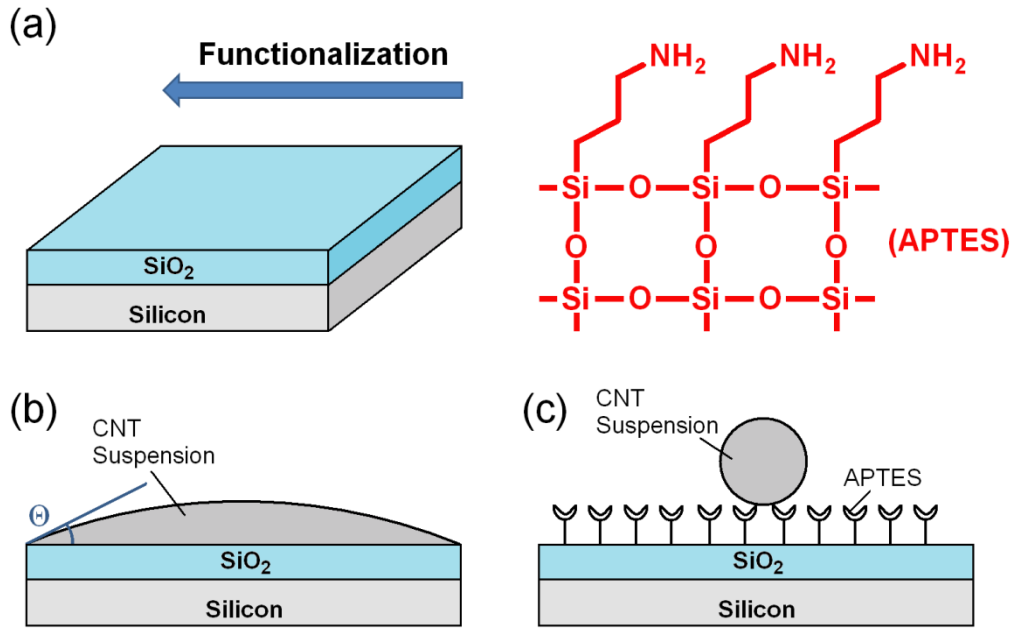


**Figure 3.2** Schematic diagram of functionalization on substrate surface. (a) APTES monolayer applied to silicon substrate. (b) CNT solution drop-cast on hydrophilic SiO<sub>2</sub> surface obtaining small contact angle  $\Theta$ . (c) CNT solution on hydrophobic surface functionalized with APTES [80].

solution-based deposition method has similar advantages but more straightforward, in the fact that no additional transfer step is required.

In this work, solution-based method was used to deposit CNT random networks on silicon substrate. In general, the substrate should be clean and smooth to enable uniform distribution of CNTs on surface and good contact between CNTs and substrate. Alternatively, substrates could be chemically treated adding a self-assembled monolayer (SAM) to enhance the adhesion and homogeneity of deposited CNT random networks [78]-[80]. Commonly used SAM materials included silanes such as (3-aminopropyl) triethoxysilane (APTES), (11-bromoundecyl) trimethoxysilane (BTS), 11-cyanoundecyltrimethoxysilane (CTS), and *n*-octadecyltrichlorosilane (OTS) [78]. Prior research work has recommended SAM treatment as being able to improve the performance of CNTFETs due to the chemically tuned interface between CNTs and substrate [79]. To create SAM on surface, substrates were to be soaked in silane-containing organic solution for several hours, then rinsed in organic solvent and dried afterwards (s. Appendix A). Typical SAM thickness is around 10 Å [78]. Fig. 3.2 gives a schematic diagram of functionalization of substrate surface with APTES, a widely used type of SAM. As depicted in Fig. 3.2, untreated silicon surface with thermally grown

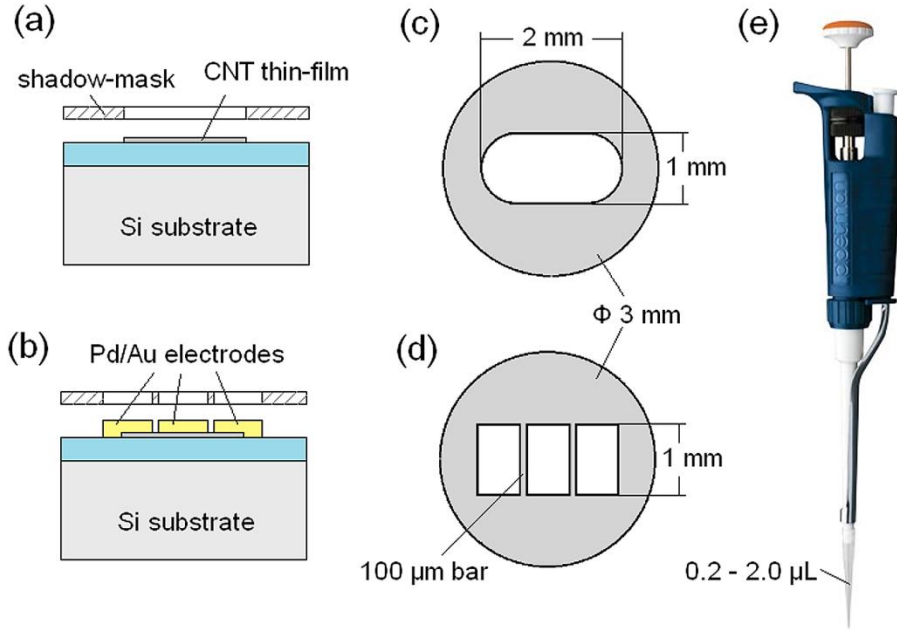


**Figure 3.3** Shadow-mask deposition for nanotube network and metal contacts: (a) CNTs deposited through a shadow-mask. (b) Metal contacts thermally evaporated through a shadow-mask on top of CNT network. (c) Layout of the TEM-grid (3 mm diameter, 1 mm × 2 mm slot) used for drop-casting CNT suspension. (d) Layout of the TEM-grid (3 mm diameter, 100 μm bar between slots, 1 mm slot width) used for metal contacts. (e) Pipette with adjustable accurate volume control (0.2 – 2.0 μL) for drop-casting, image from product sheet of Gilson.

oxide layer is hydrophilic, whereas APTES treated surface becomes hydrophobic. When a water droplet falls on hydrophilic surface, the contact angle  $\Theta$ , defined as the angle between substrate surface and the edge of droplet, is much smaller than in case of a hydrophobic surface. APTES-treated surface has been shown with a contact angle larger than  $50^\circ$  [78], [80]. Due to the hydrophobic surface, APTES-treated substrates were to be soaked in CNT solution to obtain homogeneous distribution of CNTs on substrate surface. APTES could be removed via oxygen plasma etching.

Despite the possible advantages of SAM-coating, in this study, the silicon substrate was used without additional surface treatment generally due to the consideration of reducing process complexity. When substrates were to be treated with SAM, additional process step of SAM coating would be required as well as a soaking process which required larger amount of CNT solution to cover the whole sample as mentioned before. Moreover, the adhesion of CNTs on bare  $\text{SiO}_2$  surface was observed to be sufficient that no additional treatment was urgently needed.

The silicon wafers used in this study were purchased from commercial producer. The silicon wafers were *p*-type, high-doped, <100>-oriented, and covered with a thermally grown SiO<sub>2</sub> layer on surface. The thickness of oxide layer was uniformly 200 nm. At the test phase of this study, home-made silicon wafers with various thickness of oxide layer had been used to construct CNTFETs. Silicon wafers with thinner oxide thickness, such as 45 nm and 100 nm, often suffered from breakdown of oxide layer. Silicon wafers with thicker oxide thickness, such as 300 nm, operated stably, however provided weak gate control. The original size of purchased silicon wafer was 2 inches, which was then cut into 1 cm × 1 cm chips. The silicon chips were cleaned via sonication in acetone and isopropyl alcohol (IPA) to remove particles and residues, followed by oxygen plasma treatment. Oxygen plasma effectively cleaned organic residues from substrate surface and also terminated substrate surface with OH groups that improved adhesion of CNTs to substrate [80]. Alternatively, silicon substrate could be treated with RCA clean (s. Appendix A). If necessary, a treatment with additional adhesive layer, such as APTES, could be applied to cleaned substrate.

### 3.2.2 *Printing and coating techniques*

In recent years, various techniques have been developed to deposit CNT random networks from solution onto substrate, most of which based on traditional printing and coating techniques [81]. Generally, deposition techniques can be divided in following three groups: (1) casting, like drop-casting [82], spin-coating [83], and spray-coating [15]; (2) soaking, like immerse-coating [80] and dip-coating [84]; (3) printing, like inkjet printing [18] and roll-to-roll printing [81]. There are further techniques that have not yet been used to CNTFETs but might be applicable, such as doctor blading, screen printing, and pad printing [81]. Alternatively, CNT random networks could be produced via vacuum filtration method and then transfer-printed to desired substrate [85]-[86].

As mentioned before, soaking techniques require large amount of CNT solution to cover the entire substrate. For immerse-coating, substrate is soaked in CNT solution for hours. An adhesive layer has to be added to the substrate surface before so that dissolved CNTs can be deposited on top of the adhesive layer [80]. In case of dip-coating, substrate is slowly vertically dipped into CNT solution to form Langmuir-Blodgett films of CNTs



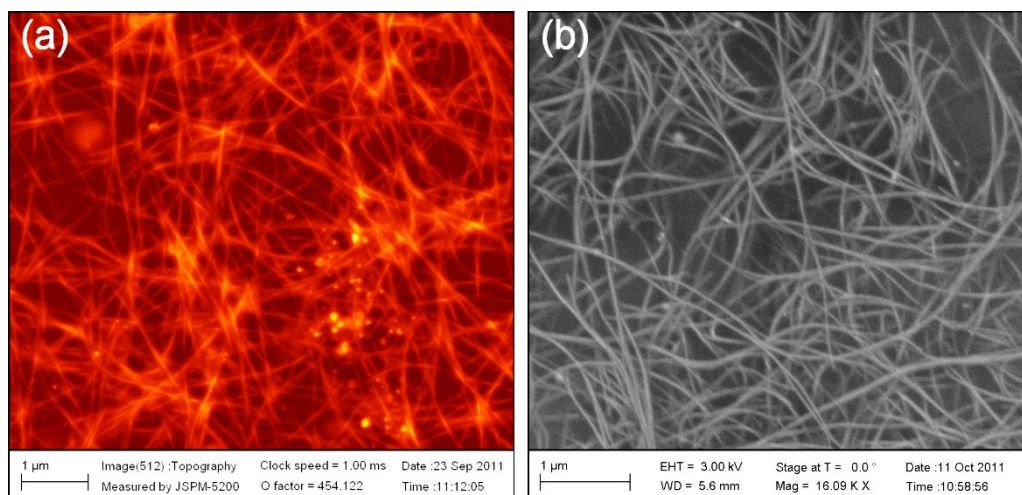


**Figure 3.4** Carbon nanotube random networks deposited on silicon substrate (scale bar: 1  $\mu\text{m}$ ). (a) AFM image. (b) FESEM image. CNTs form bundles with varied bundle length and diameter.

on substrate surface. Additional adhesive layer can be added to substrate surface to improve deposition quality [84]. In general, soaking techniques are time-consuming and non-selectively applied to the whole substrate surface.

Casting techniques require less liquid amount and are far less time-consuming than soaking techniques. Spin-coating is traditionally widely used in semiconductor industry. While CNT solution is being cast onto substrate surface, centripetal acceleration is being applied to substrate, so that a homogeneous ultrathin film can be formed on top of substrate. Adhesive layer might be required for CNT deposition [83]. Otherwise, the concentration of CNT solution should be high enough to ensure sufficient CNTs left on substrate after acceleration process. For spray-coating, fine aerosol is formed from CNT solution and sprayed to substrate through a nozzle [15]. Both spin-coating and spray-coating are non-selective concerning the deposited surface. In case of drop-casting, droplet of CNT solution is cast on substrate surface, for instance via pipette [82]. The size of coating area relatively depends on the size of droplet.

Unlike casting and soaking techniques, which are mainly used to coat single substrate, printing techniques can be used in high yield production. Printing techniques also enable selective pattern on substrate surface. Prior research has already shown application of inkjet printing and roll-to-roll printing in fabrication of CNTFETs on flexible substrate [18]. For inkjet printing, electrostatically charged droplets are formed from CNT solution and accelerate to substrate via an electric field [81]. Due to the specific machines required

for process, the printing techniques are beyond the scope of this thesis and remain appealing aspects for future work.

In this work, CNT solution was drop-cast on silicon chips. Before drop-casting, shadow-mask was covered on top of substrate to define the area for CNT deposition. Alternatively, deposition area could be defined via patterned photoresist. However, the photoresist layer had to be removed after CNT deposition, improving the complexity of process. Also required was additional adhesive layer for CNTs to withstand the lift-off step in photoresist process. As shadow-mask was used TEM grid purchased from Plano as following: copper, *ca.* 50  $\mu\text{m}$  thick, 3 mm in diameter, with one single middle slot with a size of 1 mm  $\times$  2 mm, as schematically depicted in Fig. 3.3. Pipette with adjustable precise volume control (purchased from Gilson, 0.2 – 2.0  $\mu\text{L}$  adjustable) was used for drop-casting CNT solution. For each casting step, 0.5  $\mu\text{L}$  solution was cast on substrate. The substrate was then dried at 100  $^{\circ}\text{C}$  to leave only CNTs on surface. Fig. 3.4 shows AFM and FESEM images of deposited IsoNanotubes-S CNT random networks on silicon substrate. The average bundle diameter was around 10 nm measured by AFM, comparing with the average tube diameter of 1.4 nm for IsoNanotubes-S CNTs. As shown in Fig. 3.4, the bundle length could exceed several micrometers, comparing with the average tube length of 1.0  $\mu\text{m}$  for given CNTs. The irregular sizes of CNT bundles increase difficulties in attempt to accurately count the number of CNTs based on microscope images. Apart from AFM and FESEM, the transmission electron microscope (TEM) has also been used to observe nanotubes.

### 3.2.3 Network density control

Network density is a parameter used to characterize CNT random network. Literally, network density can be obtained by counting the total number of CNTs within a given area. Practically, however, the total number of CNTs is difficult to count due to the irregularity of CNT bundles, as mentioned in Section 3.2.2. Alternatively, network density could be estimated by measuring and comparing the sheet conductance of CNT random network with reference networks [85].

**TABLE 3.2**  
DENSITY GRADATION OF CNT RADOM NETWORKS

Concentration (mg/L)	Network density (mg/m <sup>2</sup> )	Tube density (tube/μm <sup>2</sup> )
2.5	0.625	144
5.0	1.25	288
10	2.5	576
20	5.0	1152
40	10	2304
60	15	3456

Drop-casting of 0.5 μL CNT suspension in an area of 2 mm<sup>2</sup>

In this work, another method was developed to estimate the network density of CNT random networks based on drop-casting technique. The network density was considered as a function of drop-cast area, CNT concentration and drop-cast liquid volume, given as:

$$\text{Network Density} = \frac{\text{CNT Concentration} \times \text{Volume}}{\text{Area}} \quad (3.01)$$

For example, assuming drop-casting of 0.5 μL suspension with a CNT concentration of 10 mg/L in an area of 2 mm<sup>2</sup>, the network density is then calculated to be 2.5 mg/m<sup>2</sup> (2.5 × 10<sup>-15</sup> g/μm<sup>2</sup>).

As a result, the network density of drop-cast CNT random networks could be controlled either by changing the concentration of CNT solution or by varying the drop-cast liquid volume. As mentioned before, CNT/NMP suspensions were prepared in three basic concentrations: 2.5 mg/L, 5 mg/L, and 10 mg/L. To obtain even higher network density, multi-casting of 10 mg/L CNT suspension was applied. In the following parts, multi-casting of 10 mg/L CNT suspension for twice, four times, and six times was considered as with the equivalent concentration of 20 mg/L, 40 mg/L, and 60 mg/L, respectively. Therefore, following concentration gradation was included in this study: 2.5 mg/L, 5 mg/L, 10 mg/L, 20 mg/L, 40 mg/L, and 60 mg/L.

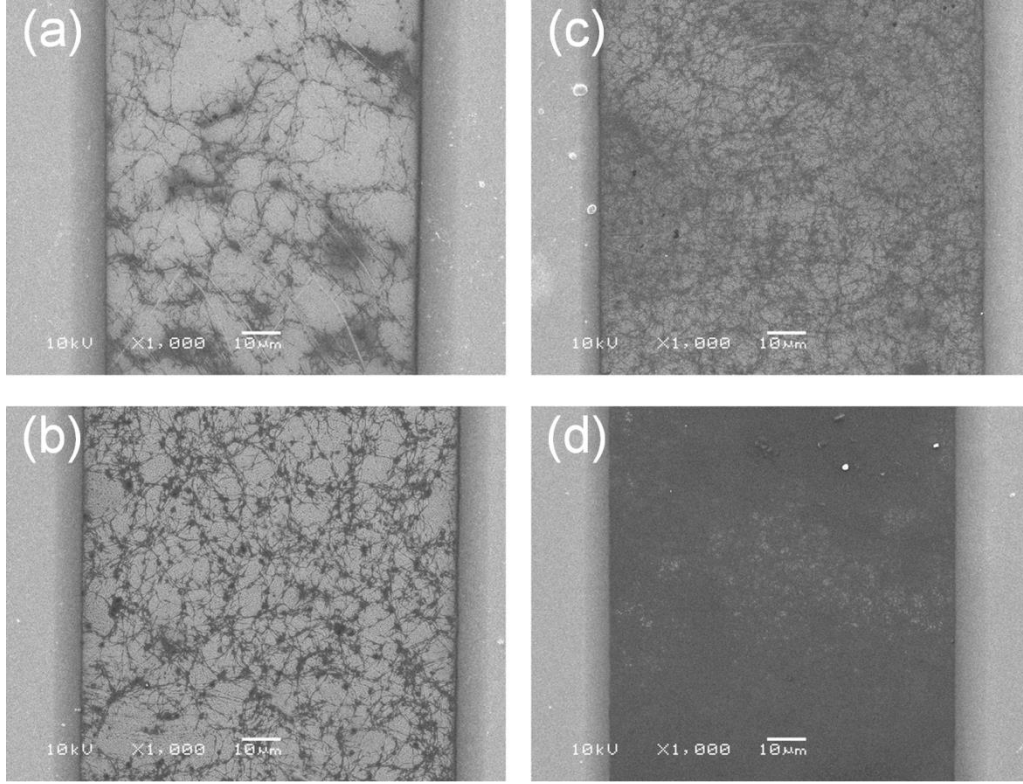


**Figure 3.5** Random network-based CNTFETs with different network density (SEM images taken from IsoNanotubes-S CNTFETs, scale bar: 10  $\mu\text{m}$ ). (a) CNT Network deposited from 2.5 mg/L suspension (90%-sc, channel length: 79  $\mu\text{m}$ , network density near the percolation threshold). (b) CNT network from 10 mg/L suspension (98%-sc, channel length: 96  $\mu\text{m}$ , network density above the percolation threshold). (c) CNT network equivalently from 20 mg/L suspension (90%-sc, channel length: 98  $\mu\text{m}$ ). (d) CNT network equivalently from 60 mg/L suspension (98%-sc, channel length: 89  $\mu\text{m}$ ).

The network density calculated above could be considered as the total weight of CNTs within a unit area. Alternatively, the tube density could be estimated on hand of network density and the average weight of carbon nanotube, as following:

$$\text{Tube Density} = \frac{\text{Network Density}}{\text{Average Tube Weight}} \quad (3.02)$$

The average tube weight  $m_t$  can be obtained from given CNT parameters, as following:

$$m_t \approx \frac{\pi \cdot d_t \cdot l_t}{\alpha_{c-c}^2} \times \frac{12 \text{ g/mol}}{N_A} \quad (3.03)$$

Where  $d_t$  is the average tube diameter,  $l_t$  the average tube length,  $a_{c-c}$  the nearest c-c distance (*ca.* 0.142 nm [23]),  $N_A$  the Avogadro's constant ( $6.022 \times 10^{23} \text{ mol}^{-1}$ ), and 12 g/mol the mole mass of carbon atom. For example, the IsoNanotubes-S CNTs have an

average tube diameter of 1.4 nm and average tube length of 1.0  $\mu\text{m}$ , so that the average tube weight  $m_t \approx 4.34 \times 10^{-18}$  g. Assuming drop-casting of 0.5  $\mu\text{L}$  suspension with a CNT concentration of 10 mg/L in an area of 2  $\text{mm}^2$ , the network density is then 2.5  $\text{mg}/\text{m}^2$ , whereas the tube density is 576  $\text{tube}/\mu\text{m}^2$ . If the CNT concentration changes to 2.5 mg/L, the network density is then 0.625  $\text{mg}/\text{m}^2$ , and the tube density 144  $\text{tube}/\mu\text{m}^2$ . At first sight, the estimated tube density appears to be higher than observed in microscope images. However, as mentioned before, CNTs within the random network tend to form bundles, where tens of CNTs could appear together in one single rope. Table 3.2 lists the gradations of CNT concentration, network density, and tube density used in this study.

Fig. 3.5 shows representative SEM images of drop-cast CNT random networks within the channel of CNTFETs. A variation of network density was obtained via drop-casting technique. In case of CNT network drop-cast from 2.5 mg/L suspension, the network density is near the percolation threshold [85]. There are only a few conducting paths across the channel, as shown in Fig. 3.5a. In case of CNT network cast from 10 mg/L suspension, the network density is already above the percolation threshold and many conducting paths can be seen uniformly distributed within the whole channel, as shown in Fig. 3.5b. As mentioned before, further increase in network density was realized via multi-casting. For instance the CNT network in Fig. 3.5c was drop-cast from equivalently 20 mg/L suspension and the network in Fig. 3.5d was drop-cast from equivalently 60 mg/L suspension. While the network density rises, the CNT network gradually becomes denser and finally almost completely covers the whole channel area.

### 3.3 Contacting carbon nanotube random network

To complete a CNTFET, deposited CNT random network has to be contacted with source/drain and gate electrodes. In prior research works, different transistor structures have been applied which could be generally divided in three types distinguished by the location of gate electrode: back-gated transistor, bottom-gate transistor, and top-gate transistor, as schematically illustrated in Fig. 3.6. The back-gated transistor employs bulk substrate as back-gate. In case of silicon wafer as bulk substrate, a thermally grown  $\text{SiO}_2$  layer can then serve as gate insulator [82]. In back-gated transistor, the back-gate acts globally over the whole substrate, while no local gate control is possible. Back-gated

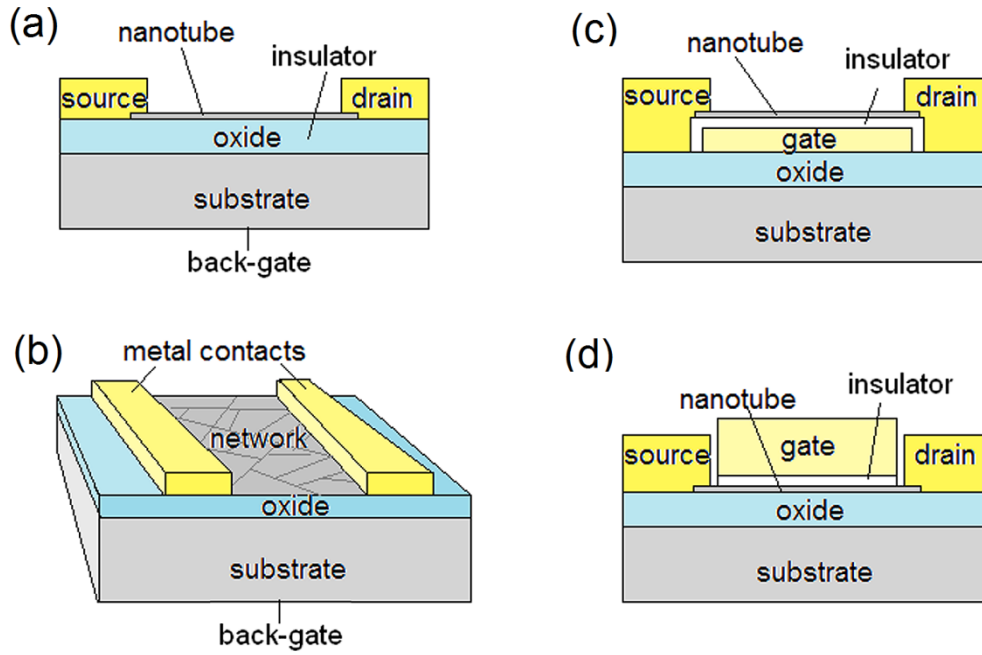


**Figure 3.6** Commonly used structures for carbon nanotube transistors. (a)-(b) Back-gated transistor with the substrate serving as a global back-gate. (c) Bottom-gate transistor with a local gate electrode beneath the CNT channel. (d) Top-gate transistor with a local gate electrode above the CNT channel. For all three structures, the CNT channel can be either of a single rope or of random network.

transistors have often found application as easy-made prototypes, because the fabrication process is simplified without the construction of a separate gate electrode.

Unlike back-gated structure, the bottom-gate [8] and top-gate transistors [22] both include a separate local gate electrode. The local gate enables separate control over individual transistors on substrate and can largely improve the efficiency of gate control. As shown in Fig. 3.6, the difference between bottom-gate and top-gate structures is the location of local gate electrode: either beneath or above the semiconducting channel. Similar to back-gated transistors, bottom-gate transistors have an open channel area, whereas the channel of top-gated transistors is covered by the local gate electrode. An open channel can be used as interface in sensors. Otherwise, the open channel area might need to be encapsulated.

An important aspect is the choice of insulating material, which strongly depends on the type of transistor structure. For instance, in case of back-gated and bottom-gate transistors, natural oxide layer can be directly grown from substrate or gate electrode,

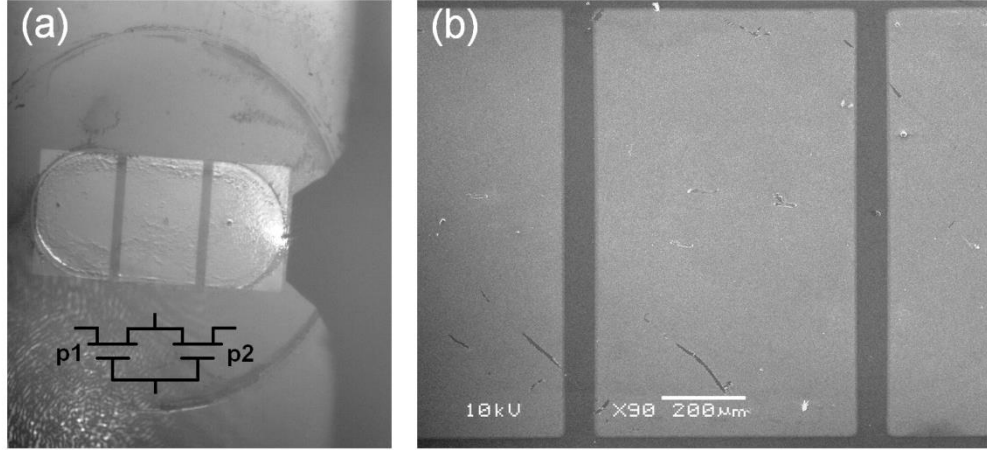


**Figure 3.7** Device layout of the back-gated CNTFET. (a) Optical microscope image taken from a sample placed on AFM stage (AFM cantilever at the right side). Two parallel connected *p*-type CNTFETs are formed from three metal contacts with the silicon substrate as a global back-gate, as depicted in insert. The CNTFETs shown here have channel geometry similar to the ones shown in (b) SEM image of the device layout with three metal contacts (scale bar: 200  $\mu\text{m}$ ).

which is hardly possible for top-gate transistors. Commonly used insulating materials with different oxide dielectric constants  $\kappa_{\text{ox}}$  include  $\text{SiO}_2$  ( $\kappa_{\text{ox}} = 3.9$ ),  $\text{Al}_2\text{O}_3$  ( $\kappa_{\text{ox}} = 8$ ),  $\text{HfO}_2$  ( $\kappa_{\text{ox}} = 16$ ) and other high- $\kappa$  materials [52], and self-assembled monolayer [87]. In general, a thin insulating layer from high- $\kappa$  material can effectively improve the efficiency of gate control [3].

Fig. 3.7 shows the device layout of back-gated transistor used in this study. Each chip contained two parallel connected *p*-type CNTFETs from three metal contacts and CNT random network beneath them. Each CNTFET on chip could be separately connected to external measurement circuit. After deposition of CNT random network, another shadow-mask was covered on top of CNT network for evaporation of metal contacts, as depicted in Fig. 3.3. Used as shadow-mask was copper TEM-grid purchased from Plano, with three slots separated by 100  $\mu\text{m}$  bar and slot width of 1 mm. Then a Pd/Au (10 nm/30 nm) multi-layer was thermally evaporated as metal contacts. Palladium has been recommended for contacting *p*-type CNTs, which could benefit hole-injection at metal-nanotube interface [88]. An additional gold layer upon palladium layer improved contact efficiency to external circuits.

The channel area of CNTFETs was defined by shadow-mask with channel length  $L = 100 \mu\text{m}$  and channel width  $W = 1000 \mu\text{m}$ . The shadow-mask evaporation enabled smooth

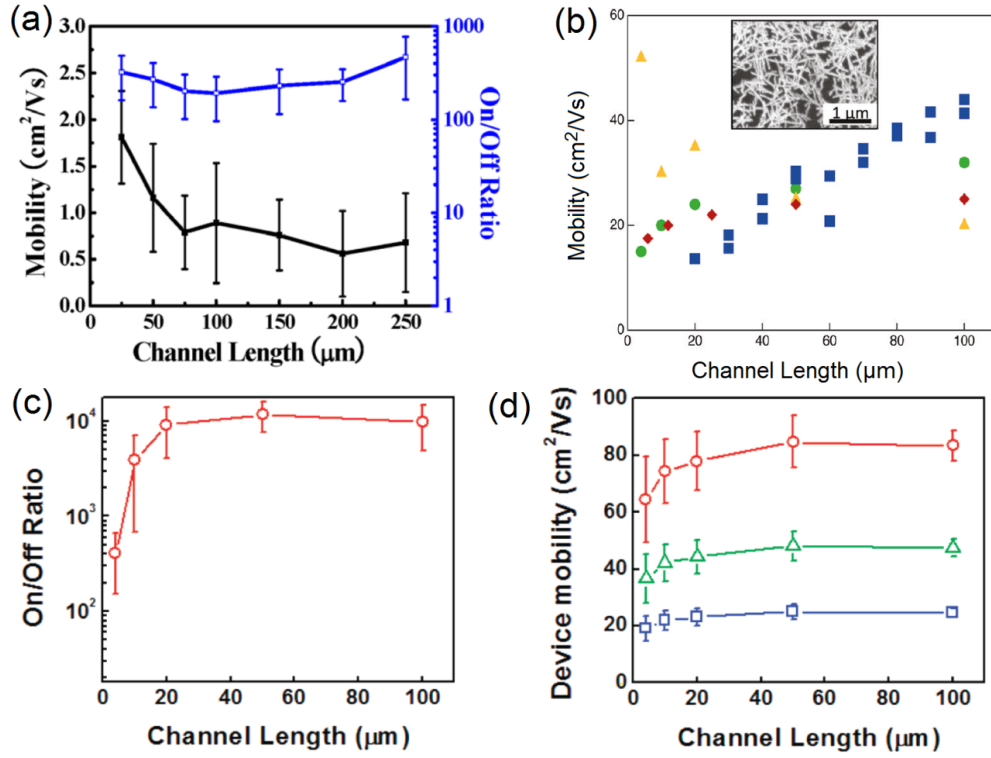


**Figure 3.8** Performance of CNTFETs as a function of channel length. (a) Effective mobility (black curve) and on-off ratio (blue curve) [9]. (b) Mobilities of CNTFETs with different semiconductor enrichments (blue square: 99%-sc, green circle: 98%-sc, yellow triangle: 95%-sc, red diamond: as-grown) [21]. (c) On-off ratio and (d) field-effect mobility (red circle: analytical equation, blue square: parallel plate model, green triangle: CV measurements) [8]. All CNTFETs are random network-based but with different configurations. The device performance remains relatively stable within the channel length range between 80  $\mu\text{m}$  and 100  $\mu\text{m}$ .

edge of metal contacts comparing with photoresist and lift-off process [89]. However, the channel length could vary from the designed length of 100 nm, for instance from 79  $\mu\text{m}$  to 98  $\mu\text{m}$  as shown in Fig. 3.5. Prior research works have already discussed the influence of channel length on performance of CNTFETs in terms of on-off ratio and device mobility, some of them cited in Fig. 3.8 [8]-[9], [21]. Generally, variation in transistor performance has been observed especially in case of small channel length. For a channel length range from 80  $\mu\text{m}$  to 100  $\mu\text{m}$ , the transistor performance has been observed relatively stable with no significant influence shown from the change of channel length, as can be seen in Fig. 3.8. Therefore, in the following discussions, the variation in channel length is negligible and thus uniformly considered to be 100  $\mu\text{m}$ .



## Chapter 4

# Characterization of Carbon Nanotube Random Network Transistors

Characterization of random network-based CNTFETs was carried out at room-temperature in ambient environment on a probe station controlled by a Keithley-4200 Semiconductor Characterization System (SCS) which provided measurement program specified with nanotube transistors.

The transistor characteristics of intrinsic CNTFETs are generally known as similar to the conventional *p*-type MOSFET either in depletion or in enhancement mode [22]. Section 4.1 provides details of the transistor characteristics of random network-based CNTFETs. Based on measured transistor characteristics, various device parameters can be extracted. Section 4.2 gives detailed discussion to each device parameter with definition and experimental results. An overview of the device performance of random network-based CNTFETs used in this study is summarized in Table 4.1 at the end of this chapter. In general, following parameters are included in this chapter: on-off ratio, transconductance, drain conductance, MOSFET mobilities, threshold voltage, subthreshold swing, and further frequency characteristics. Among them, the on-off ratio and mobility are two most often used parameters for comparing the electronic performance of CNTFETs, while the frequency characteristics are required for application in the frequency technique. Both on-off ratio and mobility can be extracted

from the transfer characteristics of CNTFETs. Concerning the mobility, different terms have been used in research and this study generally focused on the field-effect mobility. Characterization of the on-off ratio and field-effect mobility is the basis for the performance analysis in Chapter 5.

The second part of this chapter deals with the use of Raman spectroscopy in characterization of CNT random networks. The Raman characterization was carried out on a WITec alpha300-M confocal Raman microscope at room-temperature in ambient environment. As mentioned before, the Raman spectroscopy has been used to characterize the quality of target material, for instance the contents of good and defected tubes within CNT random networks. Section 4.3 gives details of the Raman spectra of SWNTs. When combined with a confocal microscope, 2D images can be scanned from target surface, for instance the channel area of CNTFETs, providing a scanned image of material distribution on target surface.

## 4.1 Transistor characteristics

In general, two kinds of transistor characteristics were measured on CNTFETs: the transfer characteristics and the output characteristics. For instance, transistor characteristics taken from a random network-based CNTFET (IsoNanotubes-S CNTs) are shown in Fig. 4.1. The transfer characteristic  $I_d$ - $V_{gs}$  was plotted as the drain current  $I_d$  as a function of the gate-source voltage  $V_{gs}$ , measured by a constant drain-source voltage  $V_{ds}$ . Transfer characteristics have often been plotted both in linear and in logarithmic scales, as shown in Fig. 4.1a. The output characteristics  $I_d$ - $V_{ds}$  were plotted as the drain current as a function of the drain-source voltage, often measured with a series of constant gate-source voltages and in linear scale, as shown in Fig. 4.1b. CNTFETs are intrinsically  $p$ -type transistors when no additional doping has been applied. The  $p$ -type transistors can be switched on via negative gate-source voltage, while switched off via positive gate-source voltage, as shown in Fig. 4.1a. Therefore, the drain-source voltage applied on CNTFET should also be negative, while the source electrode connected to ground. In  $p$ -type transistors, holes are the major charge carriers. When CNTFET is switched on, holes are tunneling through the Schottky barrier between CNT and metal contacts and injected into

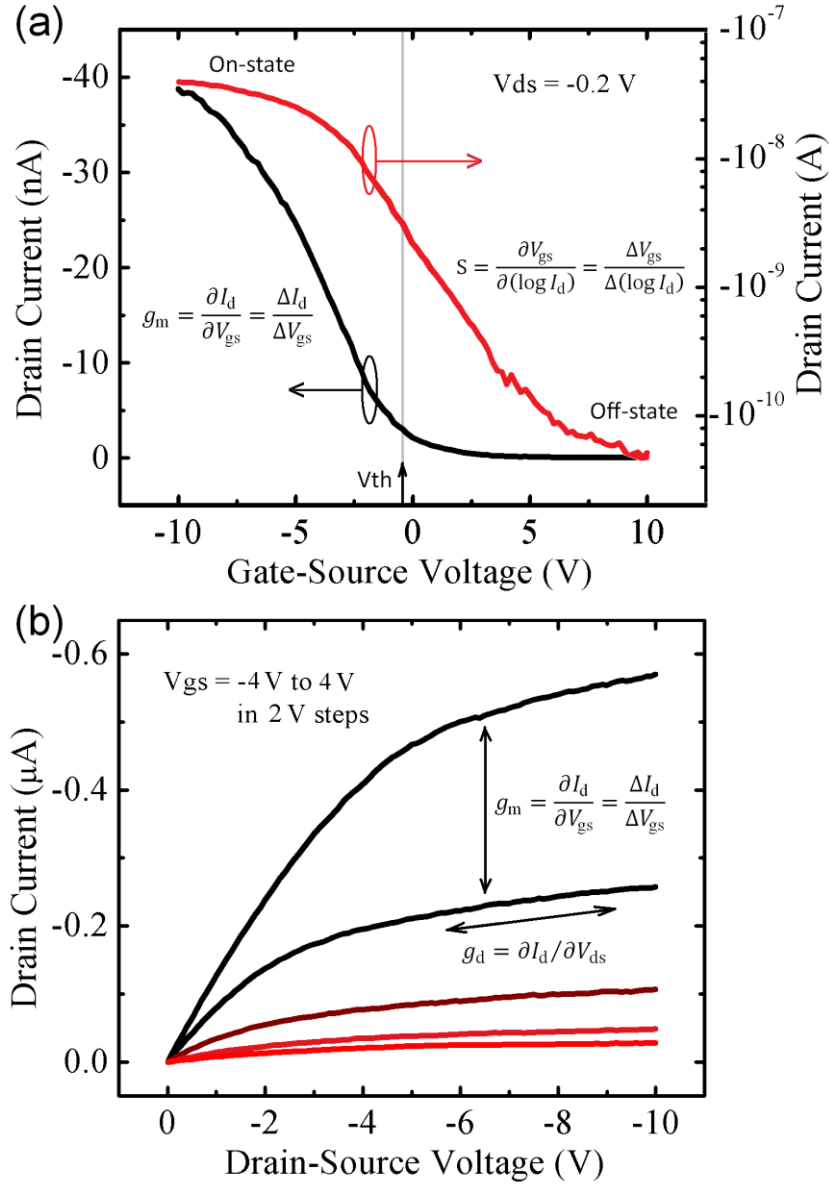


**Figure 4.1** Transistor characteristics of random network-based CNTFET. (a) Transfer characteristics  $I_d$ - $V_{gs}$  in linear and logarithmic scales ( $V_{ds} = -0.2$  V). The  $p$ -type transistor is switched on by negative gate bias. Threshold voltage  $V_{th}$  marks the threshold between the subthreshold and above-threshold regions. Transconductance  $g_m$  and subthreshold swing  $S$  can be extracted from the slope of transfer characteristics. (b) Output characteristics  $I_d$ - $V_{ds}$  taken in negative drain voltage sector and  $V_{gs}$  from -4 V to +4 V in 2 V steps (from top to bottom). Drain conductance  $g_d$  can be extracted from the slope of output characteristics.

CNT channels. For  $p$ -type transistors, the output characteristics are to be measured in the negative sector of drain-source voltage, as shown in Figure 4.1b.

The transfer characteristics represent the field control effect of gate electrode on drain current. Similar to the conventional silicon transistors, CNTFETs can be switched

between on-state and off-state, as shown in Fig. 4.1a. The ratio between the drain currents at both states is defined as the on-off ratio. The higher the efficiency of gate control, the larger is the on-off ratio. For instance, the transfer characteristics shown in Fig. 4.1a were measured within a voltage range of  $V_{gs}$  from -10 V to +10 V, and  $V_{ds} = -0.2$  V. The CNTFET had an on-off ratio around  $10^3$ . More details about the on-off ratio are given in Section 4.2.1 and in Section 5.2. In addition to on-off ratio, several further device parameters can be extracted from the transfer characteristics, like the subthreshold swing  $S$  and the transconductance  $g_m$ . With the threshold voltage  $V_{th}$  as the threshold point between the on- and off-states, the transfer characteristic can be divided in two regions: the subthreshold region and the above-threshold region. Within the subthreshold region, subthreshold swing can be extracted from the inverse slope of transfer characteristic in logarithmic scale, as shown in Fig. 4.1a. Details about subthreshold swing are given in Section 4.2.4. Within the above-threshold region, transconductance can be extracted from the slope of transfer characteristic in linear scale, details given in Section 4.2.2.

The output characteristics represent the control of drain-source voltage on drain current. Similar to the conventional silicon transistors, the output characteristics of CNTFETs can be divided into the linear region and the saturation region. Fig. 4.1b shows the output characteristics of a random network-based CNTFET measured within a voltage range of  $V_{ds}$  from 0 V to -10 V, and a series of  $V_{gs}$  from -4 V to +4 V in 2 V steps. The linear region is when the drain-source voltage is small and the drain current rises quasi-linearly with the increase in drain-source voltage. Within the linear region, the output characteristics can be considered as quasi-ohmic. At the same time, the drain conductivity is strongly influenced by the gate-source voltage, as shown in the on-state of CNTFET in Fig. 4.1a. The higher the gate-source voltage, the larger is the drain conductivity. The saturation region is when the increase in drain current tends to saturate with increasing drain-source voltage. In this region, the drain current remains relatively, while the influence of gate-source voltage on drain conductivity becomes largely reduced. Several device parameters can be obtained from the output characteristics. The drain conductance  $g_d$  can be extracted from the slope of output characteristics, while the transconductance can also be approximately estimated, as shown in Fig. 4.1b. Therefore, the transistor gain can be calculated as the ratio between transconductance and drain conductance. Details about those device parameters are given in Section 4.2.2.

## 4.2 Characterization of transistor performance

### 4.2.1 On-off ratio

A critical point concerning the device performance of CNTFETs is the on-off ratio, which is defined as the ratio between on-current  $I_{\text{on}}$  and off-current  $I_{\text{off}}$ . From the view of logic technique, a higher on-off ratio enables higher signal-to-noise ratio and larger switching capability of transistor. As mentioned before, the on-off ratio represents the efficiency of gate control on drain current. Moreover, on-off ratio becomes higher by increase in on-current or decrease in off-current. For the latter case, smaller off-current also means lower static power dissipation, which is desired in logic circuits [90]. In general, an on-off ratio in the range of  $10^4$ – $10^7$  has been recommended for emerging devices to be able to compete with conventional silicon transistors used in logic circuits [11]. To obtain such on-off ratio, the semiconducting channel of transistor has been recommended to have a band gap of preferably 0.4 eV or more [90]. As stated before in Section 2.1.3, the band gap of semiconducting CNT is inversely proportional to the tube diameter [43], [45]. For instance, CNTs used in this study have an average tube diameter of 0.8 nm for SG65 CNTs and 1.4 nm for IsoNanotubes-S CNTs, resulting in a band gap of 1.0 eV for SG65 and 0.6 eV for IsoNanotubes-S, which means CNTFETs based on those two kinds of CNTs could theoretically provide as high on-off ratio as required. The requirement on the on-off ratio also varies with the application fields. Generally, logic circuits require the highest on-off ratio to ensure sufficient signal-to-noise ratio as well as to depress the static power dissipation, while analog circuits of radio frequency devices could be satisfied with on-off ratio down to  $10^2$  [18].

In previous research works, the value of on-off ratio was for single rope-based CNTFETs in the range of  $10^3$ – $10^6$  [47]–[48], [50], while for random network-based CNTFETs in the range of  $10^2$ – $10^5$  [8], [17]–[18]. For single rope-based CNTFETs, variation in the on-off ratio could be resulted by transistor structures, for instance top-gate or bottom-gate, or by measurement conditions, for instance the choice of drain-source voltage. Depending on the drain-source voltage applied on device, the measured on-off ratio could vary for several orders of magnitude, as shown in [22]. The lower the drain-source voltage, the larger would be the on-off ratio, due to the more significant gate control effect in the linear region than in the saturation region, as mentioned before. In

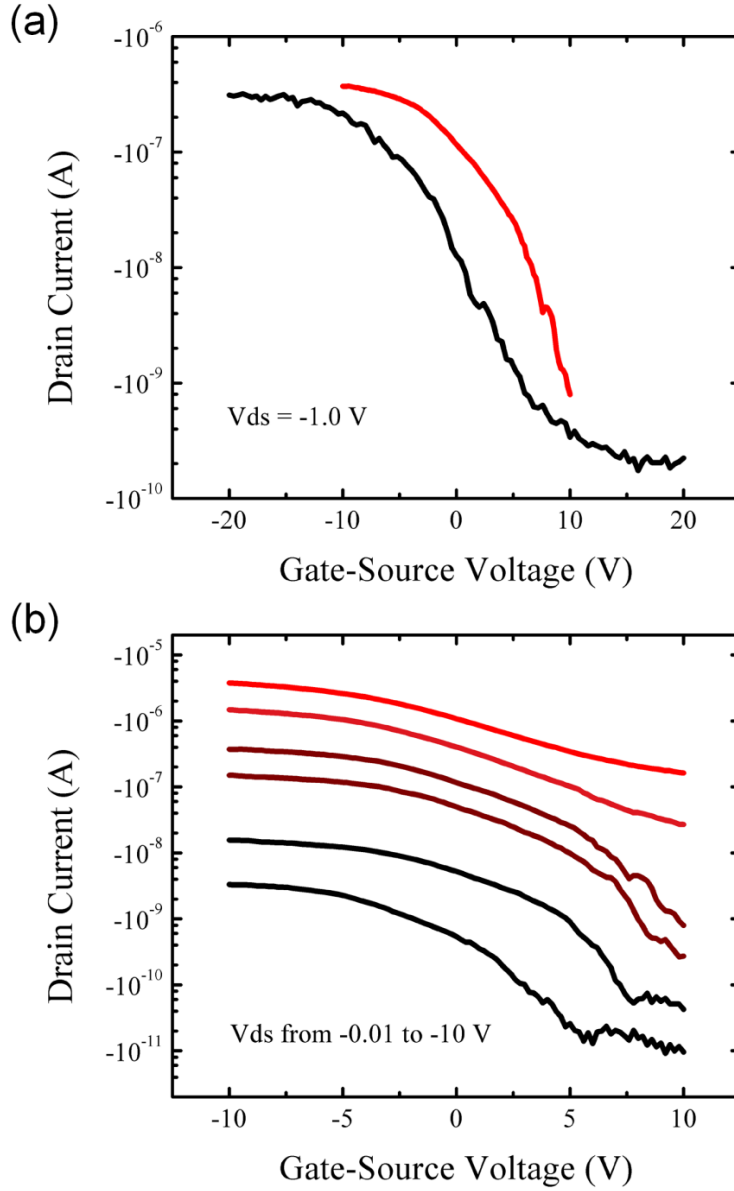


**Figure 4.2** Influence of measurement settings on the range of on-off ratio. (a) Transfer characteristics measured for  $V_{gs}$  from -10 V to +10 V (red) and from -20 V to +20 V (black,  $V_{ds} = -1.0$  V in both cases). (b) Transfer characteristics measured for  $V_{gs}$  from -10 V to +10 V and by different  $V_{ds}$  (from bottom to top:  $V_{ds} = -0.01$  V, -0.04 V, -0.4 V, -1.0 V, -4.0 V, and -10 V).

case of random network-based CNTFETs, variation in the on-off ratio could also be influenced by the semiconductor enrichment of CNTs as well as the geometry of semiconducting channel. Generally, the higher the semiconductor enrichment, the higher would be the on-off ratio of random network-based CNTFETs. Details about the influence of composition of CNT random networks on the device performance including the on-off ratio are discussed in Chapter 5. Influence of the channel geometry on device performance of CNTFETs is beyond the scope of this thesis. Generally, previous research

works have shown that increase in channel length or decrease in channel width could improve the on-off ratio [8], [22]. The latter one has been known as the stripping technique which divides large channel width into small strips [22]. Similar to random network-based CNTFETs, stripping on graphene transistors could also improve the on-off ratio to several orders of magnitude [90].

Fig. 4.2 gives examples of the influence of measurement settings on transfer characteristics taken from a random network-based CNTFET made in this study. Firstly, enlarging the range of  $V_{gs}$  could further enhance the on-off ratio. As shown in Fig. 4.2a, when measured within a wider range of  $V_{gs}$  from -20 V to +20 V instead of from -10 V to +10 V, the on-off ratio increases via depression of the off-current. Secondly, decreasing  $V_{ds}$  could improve the on-off ratio. As shown in Fig. 4.2b, transfer characteristics taken with a series of  $V_{ds}$  from -0.01 V to -10 V exhibit change in on-off ratio with up to one order of magnitude. However, change of the sweep step or sweep direction (forwards or backwards) of  $V_{gs}$  has not been observed to affect the on-off ratio.

In this work, transfer characteristics of CNTFETs were measured equally within a range of  $V_{gs}$  from -10 V to +10 V and by  $V_{ds} = -1.0$  V. As shown in Fig. 4.1, within the chosen range of  $V_{gs}$ , the CNTFET reaches its on- and off-states. Hysteresis has also been observed in random network-based CNTFETs, as will be discussed with details in Section 5.3. Therefore, all measurements were taken with the backwards sweep direction of  $V_{gs}$  from negative to positive voltage sectors.

#### 4.2.2 Transconductance and drain conductance

As stated before, the transconductance  $g_m$  of CNTFETs can be extracted from the slope of transfer characteristic in linear scale and is defined as shown in Fig. 4.1a as

$$g_m = \left. \frac{\partial I_d}{\partial V_{gs}} \right|_{V_{ds}=\text{constant}} \quad (4.01)$$

Where  $I_d$  is the drain current,  $V_{gs}$  is the gate-source voltage, and  $V_{ds}$  the drain-source voltage [56]. Alternatively, the transconductance can also be extracted from the output characteristics [90], which is however less precise due to the limited number of  $V_{gs}$ , as shown in Fig. 4.1b as

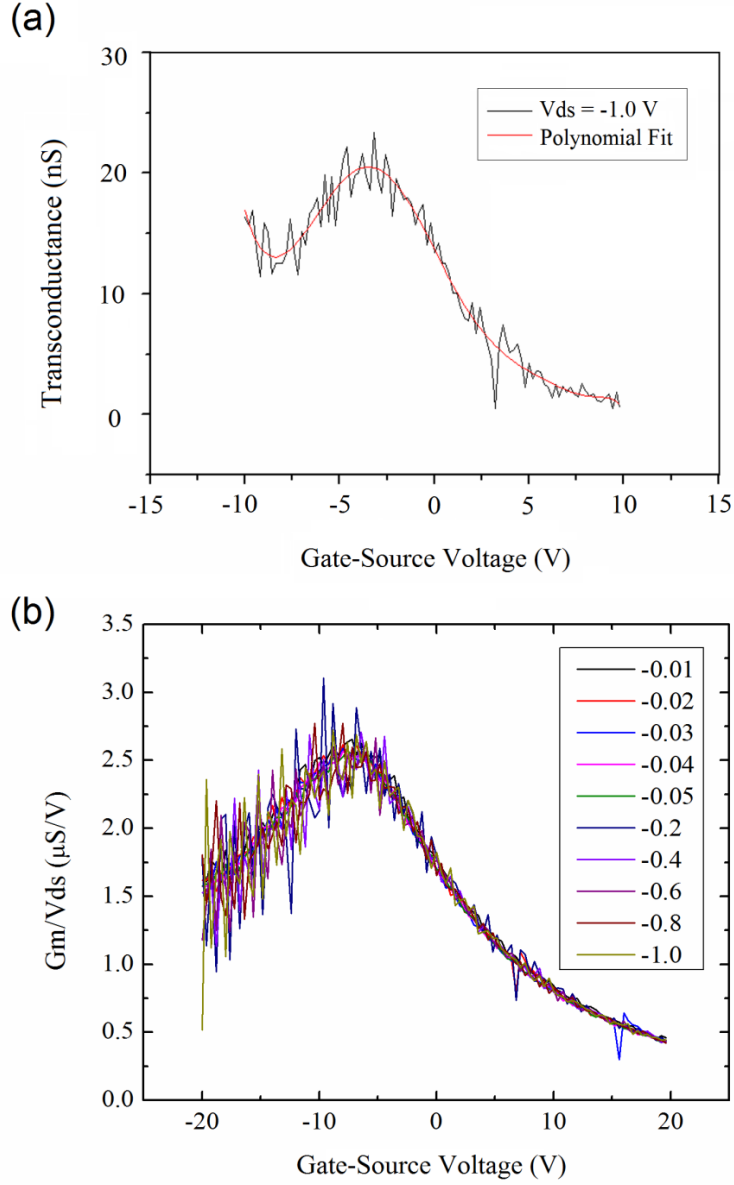


**Figure 4.3** Characterization of transconductance. (a) Transconductance measured by low current and the polynomial fit (red curve) taken as noise filter. (b) Transconductance normalized by drain-source voltage showing coincidence for a wide range of  $V_{ds}$  from -0.01 V to -1.0 V.

$$g_m = \frac{\partial I_d}{\partial V_{gs}} \approx \frac{\Delta I_d}{\Delta V_{gs}} \quad (4.02)$$

Transconductance was used to evaluate the field-effect mobility, to determine the threshold voltage via a linear extrapolation method, and to estimate the cutoff frequency. Therefore, transconductance plays an important role in the characterization of transistor performance. As mentioned above, transconductance was obtained as a function of  $V_{gs}$ . For characterization of device parameters mentioned above, the maximum  $g_{m,max}$  was



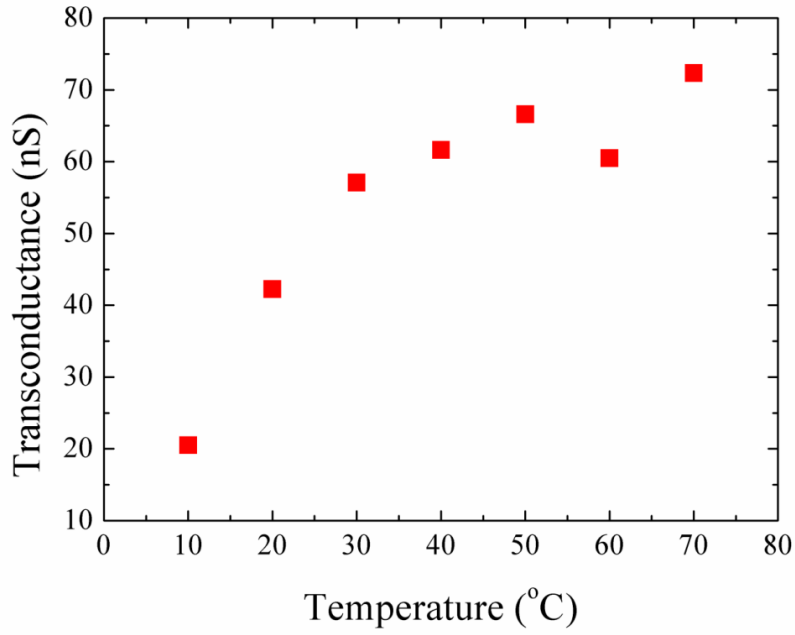


**Figure 4.4** Transconductance influenced by measurement temperature: taken on a random network-based CNTFET in ambient environment with temperature on wafer varied from 10 °C to 70 °C ( $V_{ds} = -1.0$  V). The room-temperature was around 30 °C.

applied. Distinguishing between intrinsic and terminal parameters has sometimes been recommended [90]. The intrinsic parameter restricts to the intrinsic components, while the terminal parameter also considers the influence parasitic components such as series resistances and parasitic capacitances. To simplify the discussion, this study only deals with the terminal transconductance.

Concerning the characterization of transconductance from transfer characteristics, following points need to be considered. Firstly, when the drain current was too low, for instance in the range of nanoampere, the outcome of transconductance could be quite noisy. In such case, curve fitting methods like polynomial fitting of high order was applied to filter out noise, as shown in Fig. 4.3a. Secondly, the outcome of transconductance was also affected by the drain-source voltage, due to the influence of  $V_{ds}$  on drain current. Nevertheless, the normalized value of  $g_m/V_{ds}$ , especially  $g_{m,max}/V_{ds}$  appeared to be relatively coincidental for different  $V_{ds}$ , as shown in Fig. 4.3b. In case of the random network-based CNTFETs made in this study, the value of  $g_{m,max}$  varied from 0.01  $\mu$ S to 10  $\mu$ S depending on the network density of CNT networks, when measured by

$V_{ds} = -1.0$  V. However, when measured with higher voltage of  $V_{ds} = -10$  V, the value of  $g_{m,max}$  increased for about one order of magnitude, as listed in Table 4.1.

Furthermore, the measurement of transconductance was also influenced by the temperature set on wafer. As shown in Fig. 4.4, the value of  $g_{m,max}$  varied from 20 nS to 70 nS, when the wafer temperature was changed from 10 °C to 70 °C. The measurement was carried out in ambient environment with the room-temperature near 30 °C. The change of wafer temperature was monitored by a Pt100 sensor (commercial resistance temperature detector) mounted on wafer. A clear fall in  $g_{m,max}$  was observed when the wafer temperature fell below the room-temperature.

The drain conductance  $g_d$  of CNTFETs can be obtained from the slope of output characteristic in linear scale and is defined as shown in Fig. 4.1b as

$$g_d = \left. \frac{\partial I_d}{\partial V_{ds}} \right|_{V_{gs}=\text{constant}} \quad (4.03)$$

Where  $I_d$  is the drain current,  $V_{ds}$  is the drain-source voltage, and  $V_{gs}$  the gate-source voltage [56]. The slope of output characteristics reaches the maximum in the linear region and then gradually decreases with the increase in drain-source voltage, while the slope in the saturation region remains at relatively constantly low level. The drain conductance is also affected by the gate-source voltage due to the influence of  $V_{gs}$  on drain current especially in the linear region. In the saturation region, influence of gate-source voltage becomes negligible. Drain conductance can be used in evaluation of MOSFET mobility as an alternative to transconductance, which leads to another kind of MOSFET mobility calculated, as discussed in Section 4.2.3. Furthermore, drain conductance is also applied in evaluation of the cutoff frequency, as given in Section 4.2.5.

Fig. 4.5 shows the drain conductance extracted from the output characteristic in Fig. 4.1b, taken by  $V_{gs} = -4.0$  V. Polynomial curve fitting was applied to filter out noise. Fig. 4.5 also shows the transconductance extracted from the same output characteristic. When drain-source voltage increases, the transconductance increases while drain conductance decreases. Given the value of  $g_m$  and  $g_d$ , the transistor gain can then be calculated as the ratio between transconductance and drain conductance. As shown in Fig. 4.5, the transistor gain is above unity when  $|V_{ds}| > 3$  V and reaches the maximum ( $> 10$ ) further in the saturation region.

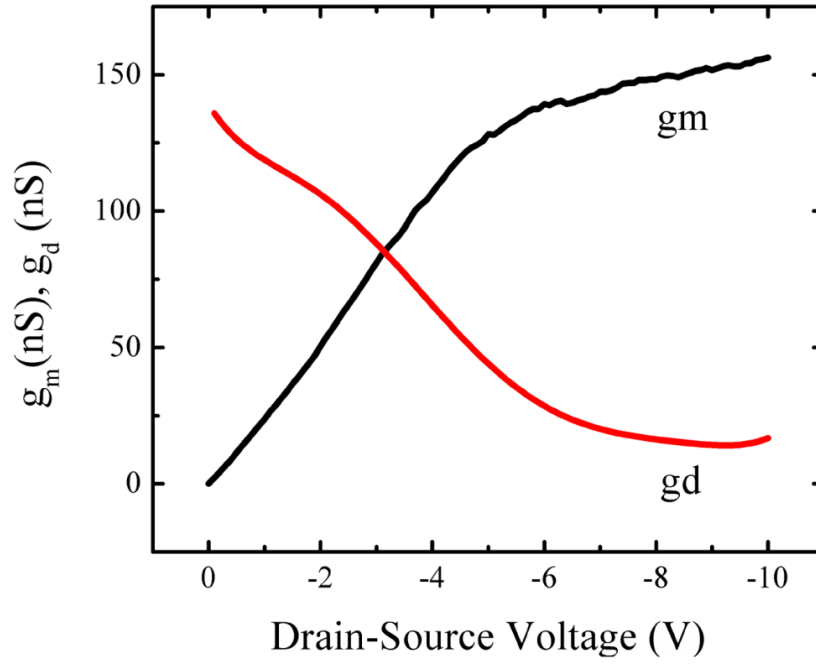


**Figure 4.5** Comparison of transconductance and drain conductance: from the output characteristics shown in Fig. 4.1, plotted as a function of drain-source voltage. The transistor gain is above unity for  $|V_{ds}| > 3$  V. The drain conductance was measured by  $V_{gs} = -4.0$  V. The curve fitting was applied on  $g_d$  as a noise filter.

### 4.2.3 Mobilities

The mobility is a tricky term to be dealt with. Firstly, there is difference between bulk mobilities and surface mobilities. The bulk mobilities include the conductivity, Hall, and magnetoresistance mobilities, in which case the charge carrier move freely through bulk material [56]. In opposition to the bulk mobilities, the surface mobilities, especially in MOSFET, take account of additional scattering mechanisms within a restricted surface area: the semiconducting channel. Additional scatterings can be resulted by the limited channel region and the oxide-semiconductor interface, for instance from oxide charges and surface roughness [56].

The surface-relevant MOSFET mobilities then include following variations: the effective mobility  $\mu_{eff}$ , the field-effect mobility  $\mu_{FE}$ , and the saturation mobility  $\mu_{sat}$ . The effective mobility is derived from the drain conductance  $g_d$  and defined as

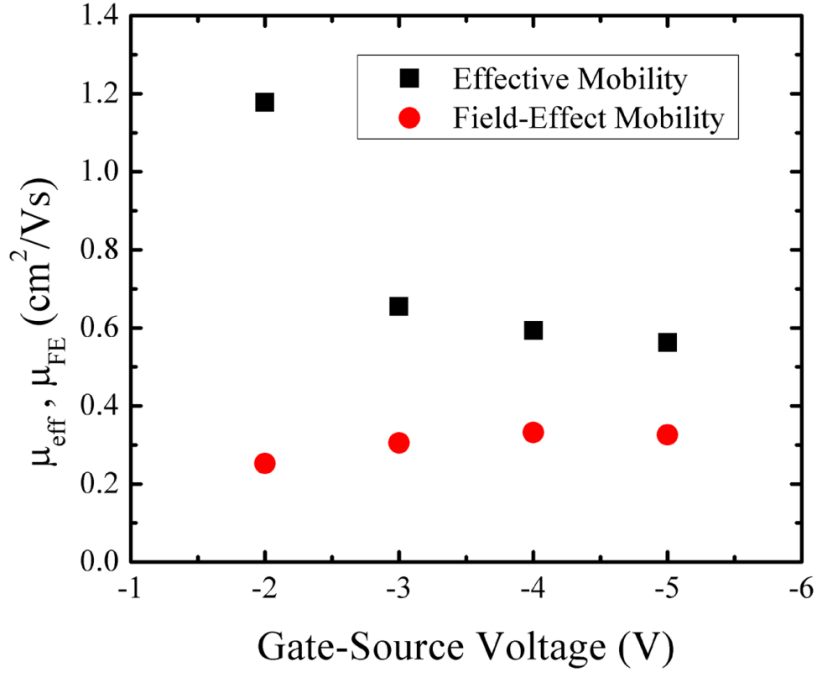


**Figure 4.6** Comparison of MOSFET mobilities: effective mobility (black squares) and field-effect mobility (red circles) plotted as a function of gate-source voltage. The value of  $\mu_{\text{FE}}$  is relatively constant, whereas the value of  $\mu_{\text{eff}}$  rises dramatically in the linear region (small  $V_{\text{gs}}$ ).

$$\mu_{\text{eff}} = \frac{L \cdot g_d}{W \cdot C_{\text{ox}} (V_{\text{gs}} - V_{\text{th}})} \quad (4.04)$$

The field-effect mobility is derived from the transconductance  $g_m$  and defined as

$$\mu_{\text{FE}} = \frac{L \cdot g_m}{W \cdot C_{\text{ox}} \cdot V_{\text{ds}}} \quad (4.05)$$

The saturation mobility is derived from the drain current  $I_d$  in the saturation region as

$$\mu_{\text{sat}} = \frac{2L}{W \cdot C_{\text{ox}} \cdot B} \cdot \left( \frac{\partial \sqrt{I_d}}{\partial (V_{\text{gs}} - V_{\text{th}})} \right)^2 \quad (4.06)$$

Where  $L$  is the channel length and  $W$  the channel width,  $C_{\text{ox}}$  is the oxide capacitance per unit area,  $V_{\text{th}}$  is the threshold voltage,  $V_{\text{gs}}$  the gate-source voltage,  $V_{\text{ds}}$  the drain-source voltage. The body effect factor  $B$  is weakly dependent on  $V_{\text{gs}}$  and typically set to around the unity [14], [56]. Because the exact value of body effect factor is rather ambiguous, this method has been rarely used and will also not be further discussed in this study.

Under same conditions, mobility obtained via the field-effect method is generally known as smaller than via the effective method due to the simplification of influence of

electric field [56]. To give an example, effective mobility and field-effect mobility were measured from a random network-based CNTFET made in this study. Fig. 4.6 shows the results plotted as a function of gate-source voltage. Within the whole voltage range, the field-effect mobility is smaller than the effective mobility, as stated before. The value of  $\mu_{FE}$  remains relatively constant, while a clear increase in  $\mu_{eff}$  is observed when gate-source voltage approaches towards the threshold voltage.

The influence of mobility on transistor performance mainly includes following aspects. Firstly, mobility indicates the charge-carrier velocity and thus the switching speed of device [14]. However, for devices operated in high electric field, for instance those transistors with extremely short channel length, the charge-carrier velocity saturates [90]. Secondly, the cutoff frequency increases with increase in mobility, although for high-field transport other factors such as the short-channel effect and parasitic resistances again take the major role instead of mobility [90]. Generally, devices with higher mobility can deliver larger current.

Concerning the characterization of MOSFET mobility, it has been suggested eliminating the influence of source/drain series resistances to achieve the intrinsic mobility [90]. Therefore, tricky could it be to compare the results of mobility obtained from different research groups, not only because of the difference between the intrinsic and terminal values, but also because of the methods taken into consideration: whether by effective method or by field-effect method. For the performance comparison in Chapter 5, terminal field-effect mobility was employed due to the relative stability of  $\mu_{FE}$  in opposition to  $\mu_{eff}$ , as stated before.

As given in (4.05), for calculation of MOSFET mobility, the oxide capacitance per unit area is required, which can be either measured from capacitance-voltage characteristics or estimated via following parallel plate model as

$$C_{ox} = \frac{\epsilon_0 \kappa_{ox}}{t_{ox}} \quad (4.07)$$

Where  $\epsilon_0$  is the permittivity in vacuum ( $8.854 \times 10^{-14}$  F/cm),  $t_{ox}$  is the oxide thickness, and  $\kappa_{ox}$  the oxide dielectric constant [56]. For example, 200 nm thick SiO<sub>2</sub> layer ( $\kappa_{ox} = 3.9$ ) as gate insulator has then an oxide capacitance of  $C_{ox} = 17.26$  nF/cm<sup>2</sup>. The oxide capacitance can be increased via high- $\kappa$  material or reducing the thickness of oxide layer. Generally, larger gate oxide capacitance enables more efficient field control of gate electrode.

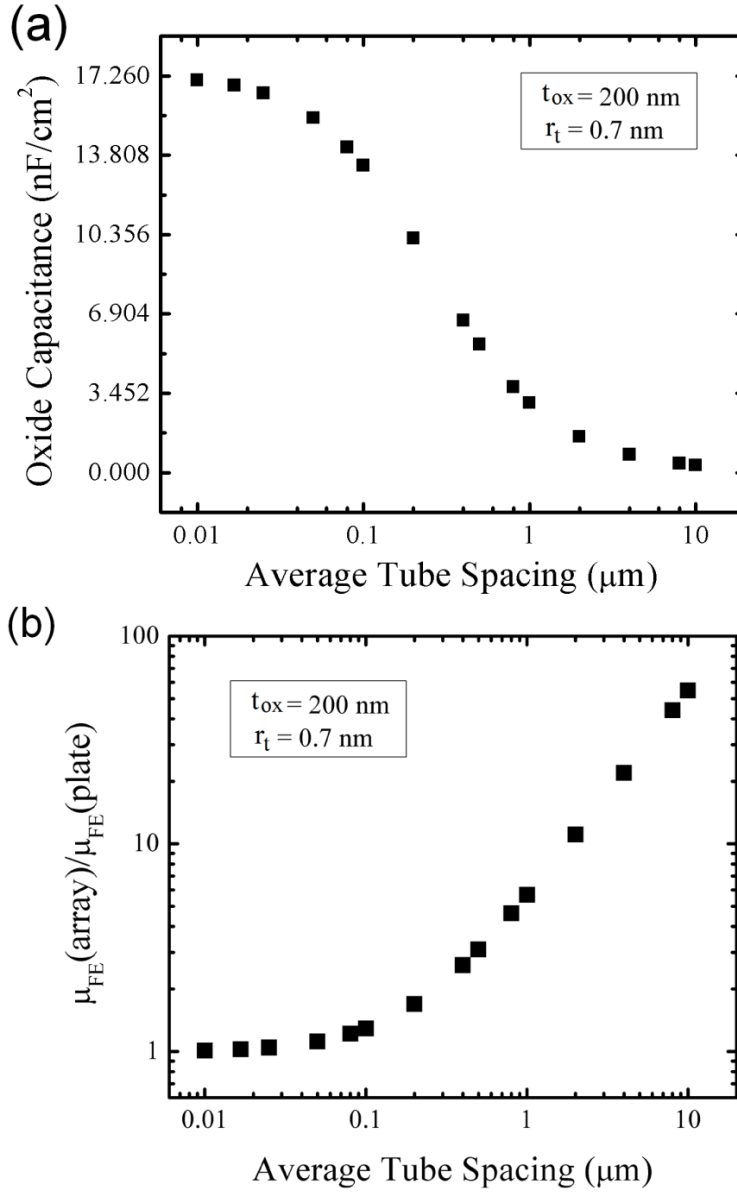


**Figure 4.7** Influence of gate oxide capacitance on field-effect mobility. (a) Oxide capacitance per unit area calculated by the array model, plotted as a function of the average tube spacing [91].  $C_{\text{ox}} = 17.26 \text{ nF}/\text{cm}^2$  from the parallel plate model, for  $\text{SiO}_2$  layer with a thickness of  $t_{\text{ox}} = 200 \text{ nm}$ , and the average tube radius of  $r_t = 0.7 \text{ nm}$  (IsoNanotubes-S). (b) Comparison of field-effect mobility obtained from the parallel plate model and the array model, plotted as a function of the average tube spacing.

Alternatively, the oxide capacitance can be calculated via a modified array model as

$$C_{\text{ox}} = \left\{ C_Q^{-1} + \frac{1}{2\pi\epsilon_0\kappa_{\text{ox}}} \cdot \ln \left[ \frac{\Lambda_0 \cdot \sinh(2\pi t_{\text{ox}}/\Lambda_0)}{\pi r_t} \right] \right\}^{-1} \cdot \Lambda_0^{-1} \quad (4.08)$$

Where  $\Lambda_0$  is the average tube spacing,  $r_t$  is the tube radius, and  $C_Q$  the quantum capacitance of CNTs ( $4.0 \times 10^{-12} \text{ F}/\text{cm}$ ) [17], [91]. The modified array model takes into

consideration of the electrostatic coupling between gate electrode and CNTs by introducing the parameter of  $\lambda_0$  [91]. Although the array model was at first developed for aligned array-based CNTFETs, it has also shown the ability of being adapted to the random network-based CNTFETs [17], [91].

To compare the outcomes of both models mentioned above, oxide capacitance was calculated according to the array model and plotted as a function of  $\lambda_0$  (from 0.01  $\mu\text{m}$  to 10  $\mu\text{m}$ ), as shown in Fig. 4.7a. The average tube radius was 0.7 nm for IsoNanotubes-S CNTs. As reference was taken the oxide capacitance calculated from the parallel plate model for 200 nm thick  $\text{SiO}_2$  layer given as example above. Moreover, the ratio between  $\mu_{\text{FE}}$  calculated via those two models was also plotted as a function of  $\lambda_0$ , as given in Fig. 4.7b. The difference made by applying different models for calculation of the oxide capacitance is less than one order of magnitude when the tube spacing is below 1  $\mu\text{m}$ . As observed in this study, a tube spacing of around 1  $\mu\text{m}$  means the CNT random network is well near the percolation threshold. Therefore, the parallel plate model could be well acceptable in calculation of the field-effect mobility.

#### 4.2.4 Threshold voltage and subthreshold swing

Generally, the threshold voltage  $V_{\text{th}}$  can be considered as a point of gate-source voltage where drain current begins to flow, which is rather ambiguous defined due to the nonlinearity of transfer characteristic [56]. Different methods have been developed to determine the threshold voltage, such as the linear extrapolation method, saturation extrapolation method, threshold drain current method, and subthreshold method [56]. Among those ones, the threshold drain current method is most straightforward by defining the threshold voltage as a point where a specified threshold drain current occurs. In this way, the value of  $V_{\text{th}}$  might vary depending on the choice of threshold current. The subthreshold method is also to be taken in the subthreshold region of transfer characteristic and in logarithmic scale, by defining the threshold voltage as a point where the drain current begins to differ from the linear relation to gate-source voltage which appears in the subthreshold region near the threshold. The saturation extrapolation method is to be taken in the saturation region, for instance at high drain-source voltage,

then from the transfer characteristic a curve of  $I_d^{1/2}$  is plotted as a function of gate-source voltage and linearly extrapolated at and with the maximum slope to zero drain current.

Similar to the saturation extrapolation method, the linear extrapolation method is to be taken in the linear region, for instance at low drain-source voltage, then from the transfer characteristic is linearly extrapolated at and with the maximum slope to zero drain current, as shown in Fig. 4.8. The threshold voltage is then defined as

$$V_{th} = V_{int} - \frac{V_{ds}}{2} \quad (4.09)$$

Where the intercept gate-source voltage  $V_{int}$  is obtained from linear extrapolation, and  $V_{ds}$  is the drain-source voltage at which the measurement was taken [56]. The maximum slope is obtained from the maximum of transconductance. For the example shown in Fig. 4.8, the threshold voltage is around 1.0 V when measured at  $V_{ds} = -1.0$  V. The linear extrapolation method is only valid by negligible small series resistance, therefore has to be carried out in linear region where the condition can be fulfilled [56]. In this study, the linear extrapolation method was used for determining the threshold voltage.

Threshold voltage is required to obtain device parameters such as the effective mobility and subthreshold swing. Moreover, transistors integrated in logic circuits need to have well-controlled relatively stable threshold voltages that are in coincidence with each other, especially when hysteresis is observed in transistor characteristics, as will be discussed in Section 5.3.

When threshold voltage is determined, the subthreshold swing  $S$  can be extracted from the subthreshold region of transfer characteristic. Subthreshold swing is an important parameter closely related to the switching behaviour of transistor and showing the voltage range required for switching between the on- and off-states [15], [90]. The smaller the subthreshold swing, the less change of gate-source voltage is required to switch the device. Subthreshold swing is obtained from the inverse slope of transfer characteristic in logarithmic scale as shown in Fig. 4.1 as

$$S = \left. \frac{\partial V_{gs}}{\partial (\log I_d)} \right|_{V_{ds}=\text{constant}} \quad (4.10)$$

Where  $I_d$  is the drain current,  $V_{gs}$  is the gate-source voltage, and  $V_{ds}$  the drain-source voltage [90]. For instance, the CNTFET shown in Fig. 4.1 has a subthreshold swing of *ca.*



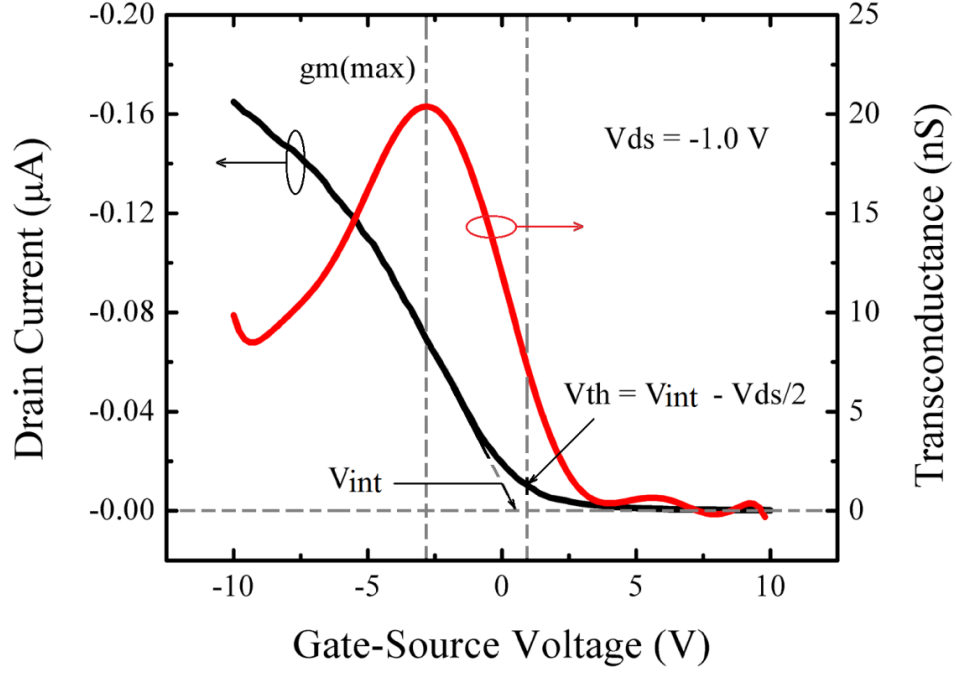


**Figure 4.8** Threshold voltage determined by the linear extrapolation method. The intercept gate-source voltage  $V_{\text{int}}$  is linearly extrapolated at and with the slope  $g_{m,\text{max}}$  from the transfer characteristic plotted in linear scale ( $V_{\text{ds}} = -1.0$  V). The threshold voltage is then given by  $V_{\text{th}} = V_{\text{int}} - V_{\text{ds}}/2$ , in this case  $V_{\text{th}} \approx 1.0$  V.

3 V/dec. The subthreshold swing was extracted as a function of gate-source voltage, and then taken at the minimum of  $S$  within the subthreshold region. Similar to the extraction of transconductance mentioned before, noise could be observed due to the small drain current in the subthreshold region. Therefore, curve fitting such as the polynomial fit was applied to filter out noise.

More precisely considered, the subthreshold swing can be defined as

$$S = \frac{kT}{q} \ln 10 \left( 1 + \frac{C_{\text{b}} + C_{\text{it}}}{C_{\text{ox}}} \right) \quad (4.11)$$

Where  $C_{\text{b}}$  is the bulk capacitance,  $C_{\text{it}}$  the interface trap capacitance,  $C_{\text{ox}}$  the gate oxide capacitance,  $T$  is the temperature,  $k$  is the Boltzmann's constant ( $8.617 \times 10^{-5}$  eV/K), and  $q$  the elemental electronic charge ( $1.602 \times 10^{-19}$  C) [56]. The bulk capacitance increases with an increase in the doping density, while the interface trap capacitance increases with an increase in the interface trap density. When both of them are clearly smaller than gate oxide capacitance, for instance in conventional silicon long-channel devices, the subthreshold swing approaches towards the ideal minimum of 60 mV/dec at the room-

temperature of 300 K. The term of  $(C_b + C_{it})$  sometimes has been replaced by the single term of  $C_{it}$  [15].

As mentioned above, subthreshold swing of random network-based CNTFETs measured in this study (*ca.* 3 V/dec) is much larger than the room-temperature limit. Experimental results have shown that subthreshold swing could be reduced by improving the efficiency of gate control via thin layer of high- $\kappa$  dielectrics [3].

#### 4.2.5 Frequency characteristics

In previous research works, the small-signal equivalent circuit has been used in analyzing the frequency response of CNTFETs, although different variations of the equivalent circuit have been employed [63], [90], [92]. Fig. 4.9 shows the small-signal equivalent circuit of CNTFET used in this study which includes the components that are relevant to the frequency characteristics discussed below. The equivalent circuit contains an intrinsic part and extrinsic part. The extrinsic part includes the series resistances connecting to the gate/source/drain electrodes:  $R_g$ ,  $R_s$ , and  $R_d$ . The intrinsic part includes the transconductance  $g_m$ , drain conductance  $g_d$ , gate-source capacitance  $C_{gs}$ , and gate-drain capacitance  $C_{gd}$  [90]. In other models, the intrinsic part might further include the gate-source and gate-drain resistances ( $R_{gs}$  and  $R_{gd}$ ) [92], or exclude the gate-source and gate-drain capacitance [63]; while the extrinsic part might further include parasitic capacitances between each two electrodes ( $C_{gdp}$ ,  $C_{gsp}$ , and  $C_{dsp}$ ) [92]. A detailed discussion about the determination of suitable small-signal equivalent circuit for CNTFETs is beyond the scope of this study and might be included in future work. Moreover, the value of elements of the small-signal equivalent circuit can be deduced from the S-parameter (scattering parameter) measurement [92].

There are two frequency parameters that have been commonly used to evaluate the frequency response of CNTFETs: the cutoff frequency  $f_T$  and the maximum frequency of oscillation  $f_{max}$ . The cutoff frequency is defined as the frequency at which the current gain of short-circuit becomes unity (0 dB), while the maximum frequency of oscillation as the frequency at which the unilateral power gain falls to unity (0 dB) [63], [93]. The current gain is defined as the output current divided by input current, while the unilateral power gain is obtained from isolated and impedance-matched output and input [63]. Normally,

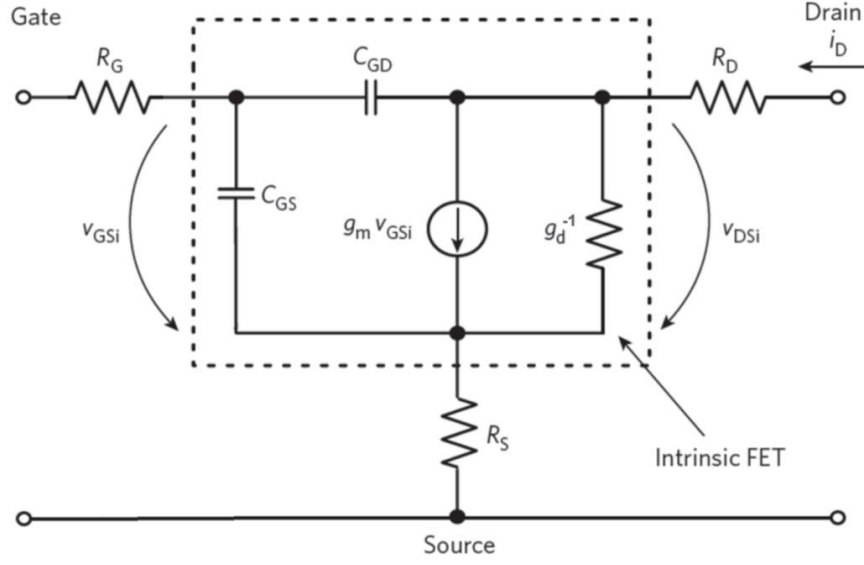


**Figure 4.9** Small-signal equivalent circuit for CNTFET [90]: intrinsic components within the dashed frame (transconductance  $g_m$ , drain conductance  $g_d$ , gate-source capacitance  $C_{gs}$ , and gate-drain capacitance  $C_{gd}$ ), and series resistance of gate electrode  $R_g$ , of source electrode  $R_s$ , and of drain electrode  $R_d$ . The intrinsic voltage  $V_{gsi}$  and  $V_{dsi}$ , drain current  $I_d$ .

those frequency parameters can be obtained via the S-parameter measurement on CNTFETs and by plotting the current and power gain against the operating frequency [94]. The cutoff frequency and the maximum frequency of oscillation set the limit at which a device can be expected to work. The higher the frequency parameters, the faster a device can be operated. Recently, the cutoff frequency of random network-based CNTFET has been found to be as high as 80 GHz [94], while for silicon MOSFET with short channel has been shown in the order of several hundred GHz [90].

Alternatively, the cutoff frequency  $f_T$  can be deduced from the small-signal equivalent circuit of CNTFET as shown in Fig. 4.9 as

$$f_T \approx \frac{g_m}{2\pi} \cdot \frac{1}{(C_{gs} + C_{gd})[1 + g_d(R_s + R_d)] + C_{gd}g_m(R_s + R_d)} \quad (4.12)$$

Where  $g_m$  is the transconductance,  $g_d$  the drain conductance,  $C_{gs}$  is the gate-source capacitance,  $C_{gd}$  the gate-drain conductance,  $R_s$  the series resistance of the source electrode, and  $R_d$  the series resistances of drain electrode [90]. Therefore, the cutoff frequency can be expected to reach the maximum by improving the transconductance

while depressing the drain conductance and other resistances and capacitances in the small-signal equivalent circuit.

When only the intrinsic part of the small-signal equivalent circuit is to be considered, then the intrinsic cutoff frequency  $f_{T,int}$  can be obtained as

$$f_{T,int} \approx \frac{g_m}{2\pi \cdot C_{ox}} \quad (4.13)$$

Where  $g_m$  is the transconductance and  $C_{ox}$  is the gate oxide capacitance [93]. Therefore, an improvement in transconductance can lead to increase in intrinsic cutoff frequency, for instance when measured in the saturation region where the maximum transconductance can be achieved [90]. Normally, the intrinsic cutoff frequency is higher than the cutoff frequency, because of the neglect of extrinsic components which lead to degradation of frequency response [94]. As an example, the random network-based CNTFETs made in this study had a 200 nm thick  $\text{SiO}_2$  layer ( $\kappa_{ox} = 3.9$ ) within an channel area of  $10^{-3} \text{ cm}^2$  ( $L = 100 \text{ } \mu\text{m}$ ,  $W = 1 \text{ mm}$ ), resulting in an oxide capacitance of 17.26 pF, while the transconductance was in the order of 100  $\mu\text{S}$  when measured at  $V_{ds} = -10 \text{ V}$  in the saturation region; therefore the intrinsic cutoff frequency was around 1 MHz.

The cutoff frequency of random network-based CNTFETs can be increased via increase in density of semiconducting tubes, which results in an increase in transconductance and thus the current gain [94]. Another influence factor is the scaling of the intrinsic cutoff frequency with the channel length [63], [90]. When channel length scales down for about one order of magnitude, the cutoff frequency will increase for about one order.

From the small-signal equivalent circuit of CNTFET, the maximum frequency of oscillation  $f_{max}$  can be deduced as a function of the cutoff frequency as

$$f_{max} \approx \frac{f_T}{2[g_d(R_s + R_g) + 2\pi f_T \cdot C_{gd} \cdot R_g]^{1/2}} \quad (4.14)$$

Where  $g_d$  is the drain conductance,  $C_{gd}$  is the gate-drain capacitance,  $R_g$  the gate series resistance, and  $R_s$  the source series resistance [63]. Generally, the values of  $f_T$  and  $f_{max}$  are of the same order of magnitude and dependent on the device characteristics [93].

## 4.3 Raman spectroscopy

### 4.3.1 Raman spectra of single-walled carbon nanotubes

The Raman spectroscopy has been commonly used in characterization of material composition and structure [56], [74], [95]. The Raman spectroscopy is a kind of vibrational spectroscopy. When light falls on the substrate surface, the frequency of scattered light can be shifted in a tiny fraction due to the atomic vibration of surface material. The main part of scattered light maintains the original frequency, known as the Rayleigh scattering; while the other parts of scattered light can either obtain a frequency shift from the interaction with acoustic phonons, known as the Brillouin scattering, or obtain a frequency shift from the interaction with optical phonons, known as the Raman scattering, which has stronger intensity than the former one [56]. To measure the Raman scattering, an intense monochromatic light source, usually a laser, is required. Normally, the intensity of scattered light is plotted as a function of the relative frequency shift, known as the Raman spectrum, as shown in Fig. 4.10. The Raman spectroscopy enables a non-contacting, non-destructive material characterization with minimum sample preparation, and free from the charging effects that occurs by electron or ion beam techniques [56].

Fig. 4.10 shows the typical Raman spectra of single-walled carbon nanotubes, measured from a random network of 98%-sc IsoNanotubes-S CNTs on silicon substrate. The Raman spectra were taken via a 532 nm green laser. The spectra includes the peak of Rayleigh scattering placed at zero Raman shift, the features of silicon substrate (around  $500\text{ cm}^{-1}$  and  $950\text{ cm}^{-1}$  in the positive sector of frequency sector), and the features of CNTs. The Raman spectra of CNTs include different categories of scattering processes, which can be generally distinguished as the first-order or second-order scatterings, while the second-order scattering further includes one-phonon or two-phonon processes [74]. For instance, the G-band and radial breathing mode (RBM) belong to the first-order scattering, while the D-band belongs to the second-order one-phonon scattering, and the M-, G'-, and 2G-bands belong to the second-order two-phonon scattering [74].

The radial breathing mode is exclusive for carbon nanotubes, as it is resulted from the radial vibration of CNTs [74], [96]-[97]. The location of RBM band has been known as dependent on the radius of CNT and can be approximately given as

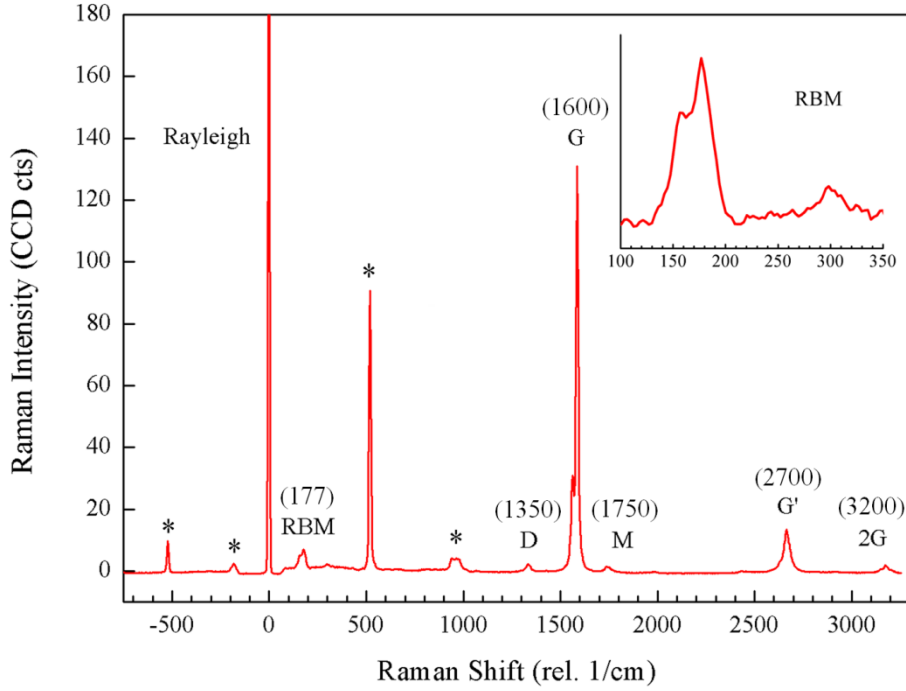


**Figure 4.10** Raman spectra of single-walled carbon nanotubes (measured via 532 nm laser,  $E_L = 2.33$  eV). The Rayleigh scattering is located at zero Raman shift with the strongest Raman intensity. Silicon features are marked with “\*”. The Raman features of SWNTs include: the RBM band around  $177 \text{ cm}^{-1}$  (insert,  $d_t = 1.4 \text{ nm}$ , the relative Raman shift  $\omega_R = 248/d_t$ ), the G-band around  $1600 \text{ cm}^{-1}$ , D-band around  $1350 \text{ cm}^{-1}$ , M-band around  $1750 \text{ cm}^{-1}$ , G'-band around  $2700 \text{ cm}^{-1}$ , and 2G-band around  $3200 \text{ cm}^{-1}$ .

$$\omega_R = \frac{248}{d_t} \quad (4.15)$$

Where  $\omega_R$  is the relative Raman shift, and  $d_t$  the tube diameter [74]. Therefore, the RBM band can be used to detect the tube diameter of CNTs. For instance, the RBM band in Fig. 4.10 has a peak at  $177 \text{ cm}^{-1}$ , resulting in a tube diameter of  $1.4 \text{ nm}$ , the same as known for IsoNanotubes-S CNTs.

The G-band is the Raman active mode for graphite, which is located at around  $1600 \text{ cm}^{-1}$  and normally contains both a  $G^+$ - and a  $G^-$ -features for SWNTs [74], [95]. Not only CNTs, but also amorphous carbon and graphene show G-band in their Raman spectra [95]. Therefore, the G-band is generally considered as an evidence for the presence of carbon material, while the intensity of G-peak indicates the amount of carbon content in total.

The D-band is a disorder-induced feature, which is located at around  $1350 \text{ cm}^{-1}$ . Unlike the first-order scatterings such as RBM and G-band, the location of D-band varies

**TABLE 4.2**  
RAMAN SPECTROSCOPIC FEATURES OF CNTs

Band	$\omega_R$ (cm <sup>-1</sup> )	Type	$d\omega_R/dE_L$	Notes
RBM	177	SR	0	Radius-dependent
G	1600	SR	0	Raman active mode
D	1350	DR1	53	Disorder-induced
oTO	860	DR1	0	IR-active mode
M	1750	DR2	-	Overtone of oTO band
G'	2700	DR2	106	Overtone of D-band
2G	3200	DR2	0	Overtone of G-band

IsoNanotubes-S CNTs, 98%-sc,  $d_t = 1.4$  nm,  $E_L = 2.33$  eV, 532 nm Laser;  
SR: first-order scattering, DR1: second-order one-phonon scattering,  
DR2: second-order two-phonon scattering [74]

with the laser energy used in measurement [74]. For instance, the laser energy is 2.33 eV for the green laser with a wavelength of 532 nm used in this study. As mentioned before, the ratio of intensities of G-band and D-band is known as the G/D ratio and has been used to characterize the quality of CNTs: the higher the G/D ratio, the smaller the content of carbon impurities such as amorphous carbon or damaged CNTs. For instance, the G/D ratio of CNTs shown in Fig. 4.10 is above 50, which indicates a very low level of carbon impurities.

The RBM, G-, and D-bands are major features used in analyzing CNTs. In addition to them, further minor features are shown in Fig. 4.10. The M-band is an overtone of the infrared (IR) active mode in graphite, which is located at around 1750 cm<sup>-1</sup> in Fig. 4.10. The G'-band is an overtone of the D-band and is located at around 2700 cm<sup>-1</sup> in Fig. 4.10. Similar to the D-band, the location of G'-band is dependent on the laser energy [74]. The 2G-band is an overtone of G-band and located at around 3200 cm<sup>-1</sup>. As shown in Fig. 4.10, for semiconducting CNTs, the G-band normally has the strongest intensity. The properties of the Raman spectroscopic features of IsoNanotubes-S CNTs used in this study are summarized in Table 4.2 [74].

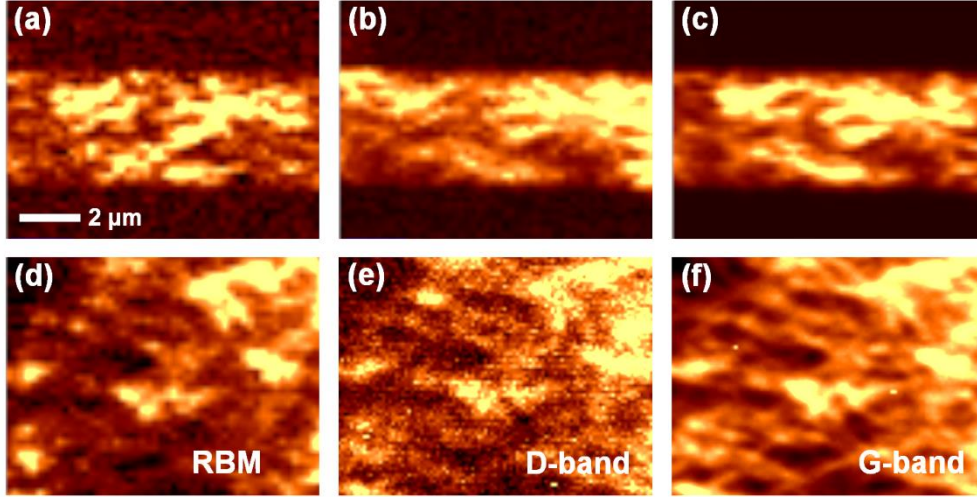


**Figure 4.11** Confocal Raman images of random carbon nanotube networks: (a)-(c) SG65 CNTs, (d)-(f) IsoNanotubes-S CNTs. Each line from left to right: the same area scanned at RBM, D-, and G-band, respectively (scale bar: 2  $\mu\text{m}$ ).

#### 4.3.2 Confocal Raman imaging of carbon nanotube random network

The Raman spectroscopic measurements were taken on a confocal Raman microscope (WITec alpha300-M), as shown in Fig. 4.1, which was connected with an external green laser source with a wavelength of 532 nm. The confocal Raman technique combines the Raman spectroscopy with confocal optical microscopy which provides a series of different measurements like the Raman line scanning (one-dimensional line scan), Raman mapping (two-dimensional area scan), and in-situ Raman study [98]. The confocal microscopy uses a laser light scanning across the selected sample surface and illuminating only one point each time; the illuminated point and the light source are confocal controlled by placing a pinhole [56]. The confocal technique can improve the contrast of scanned image although require longer time for scanning than conventional optical microscopy. The resolution of confocal microscope is given by

$$s = \frac{0.44\lambda}{\text{NA}} \quad (4.16)$$

Where  $\lambda$  is the wavelength of light source and NA is the numerical aperture [56]. The microscope used in this study had a numerical aperture of 0.5, so that the resolution was around 0.5  $\mu\text{m}$ .



As mentioned before, the Raman spectroscopy reveals the material composition on sample surface. Therefore, the Raman mapping restricted on specific Raman features can provide two-dimensional images of the location and amount of specific material on scanned sample surface, while the Raman intensity indicates the material amount, as shown in Fig. 4.10. Nevertheless, when focused on single Raman feature, the Raman intensity is a relative quantity which can vary with the laser intensity and exposure time. Generally, increase in either laser intensity or exposure time can lead to increased intensity of measured feature and thus create clearer image of scanned area with improved signal-to-noise ratio. However, the sample surface might be damaged under longer and intensive laser exposure. The Raman mapping is time-consuming. For instance, about 0.04–0.1 second was required to measure one pixel in this study, so that about 4 minutes was required to obtain a  $50 \times 50$  pixel image with a moderate scan speed of 0.1 second/pixel.

Fig. 4.11 shows the confocal Raman images taken from two different CNT random networks: one with SG65 CNTs, another with IsoNanotubes-S CNTs. As mentioned before, the Raman scan images can be taken at different features of CNTs. For instance, the images in Fig. 4.11 were taken at the RBM, D-, and G-band within the same scan area for each sample, respectively. The RBM band is radius-dependent. The G-band is for carbon content generally, which includes both CNTs and carbonaceous impurities. The D-band is for damaged CNTs. Normally, the G-band has the strongest intensity among all Raman features of CNTs thus the images scanned at G-band have the best resolution, as shown in Fig. 4.11. In case of the IsoNanotubes-S CNTs, the image scanned at D-band is the noisiest due to the lowest Raman intensity of the D-band. In case of the SG65 CNTs, the image scanned at RBM band is the noisiest, while the D-band image becomes much clearer, indicating an increased content of damaged tubes. Moreover, comparison of the Raman images taken at different features can qualitatively describe the homogeneity of material distribution. For uniformly distributed CNT network, images scanned at RBM, G-, and D-band should be quasi-consistent with each other. Finally, the bright colour indicates the location and amount of CNTs distributed on sample surface, thus the homogeneity of CNT network can be evaluated from the distribution of brightness across the scanned area.

Fig. 4.12 shows the Raman scan images from the channel area of several random network-based CNTFETs made from SG65 CNTs. The channel area was defined via a

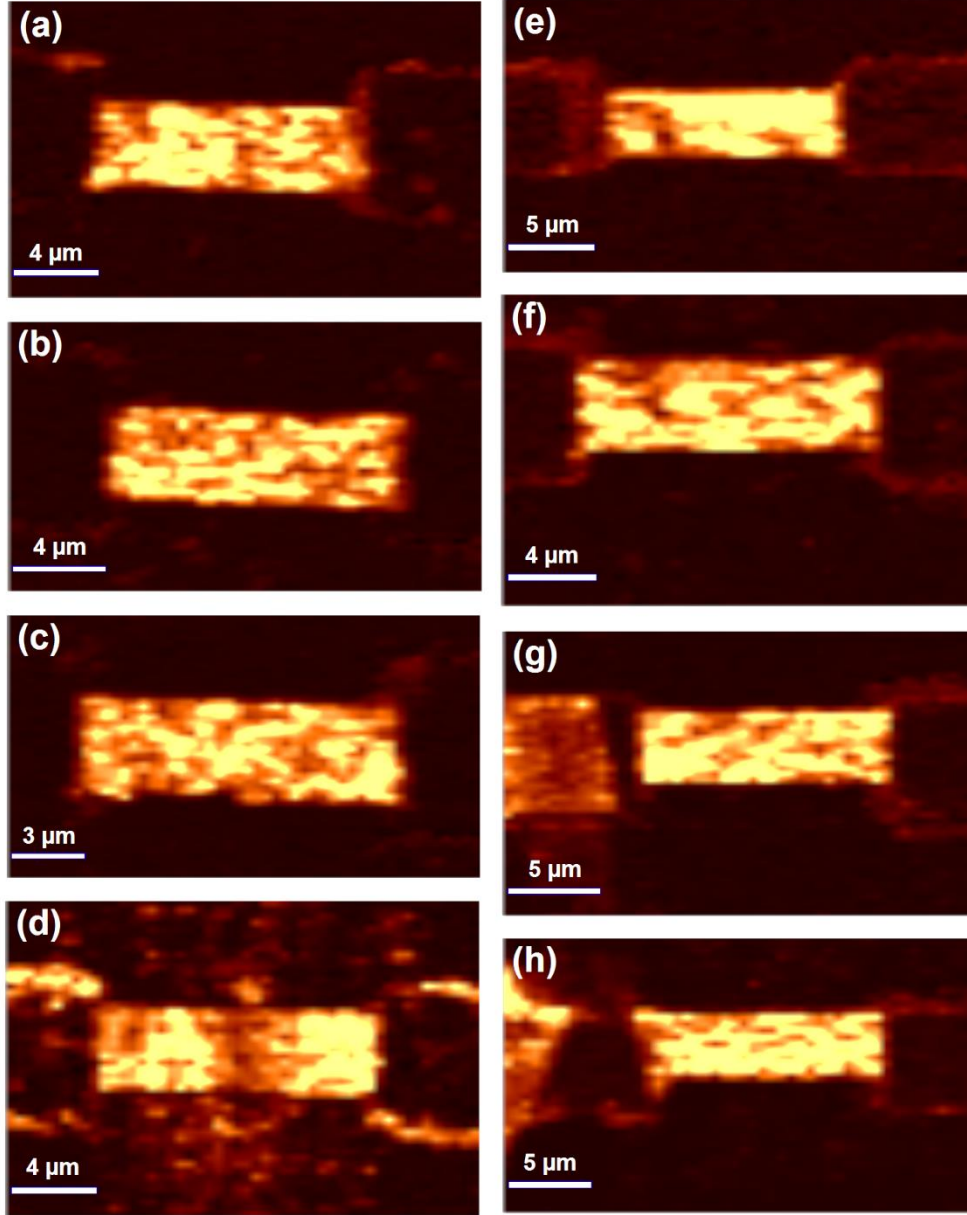


**Figure 4.12** Confocal Raman images of random network-based CNTFETs: made from solution-based process with SG65 CNTs,  $L = 12 \mu\text{m}$ ,  $W = 4 \mu\text{m}$ ; (a)-(d) are CNTFETs from one silicon wafer, (e)-(h) from another. The scale bar is  $3 \mu\text{m}$  in (c),  $5 \mu\text{m}$  in (e), (g)-(h), and  $4 \mu\text{m}$  in the rest. The scanning images were measured at the G-band around  $1600 \text{ cm}^{-1}$ . The bright colour indicates the location of CNTs.

conventional photoresist process and has a channel length of  $L = 12 \mu\text{m}$  and channel width of  $W = 4 \mu\text{m}$ . The Raman images were taken at G-band of *ca.*  $1600 \text{ cm}^{-1}$ . The intensity distribution within the channel area can be used to qualitatively predict the performance of CNTFETs. For instance, the CNTFET in Fig. 4.12e shows a higher homogeneity than the one in Fig. 4.12f, while measurement of transistor performance on

**TABLE 4.1**  
DEVICE PERFORMANCE OF RANDOM NETWORK-BASED CNTFETs

Device Parameter	Symbol	Value
CNT concentration	-	2.5 – 60 mg/L
CNT density	-	0.625 – 15 mg/m <sup>2</sup>
Channel geometry	-	$L = 100 \mu\text{m}$ , $W = 1000 \mu\text{m}$
On-off ratio	-	$1 - 10^3$ ( $V_{ds} = -1.0 \text{ V}$ , $V_{gs}$ within $\pm 10 \text{ V}$ )
Transconductance	$g_{m,max}$	0.01 – 10 $\mu\text{S}$ ( $V_{ds} = -1.0 \text{ V}$ ) up to 100 $\mu\text{S}$ ( $V_{ds} = -10 \text{ V}$ )
Transistor gain	-	$> 10$
Gate oxide capacitance	$C_{ox}$	17.26 nF/cm <sup>2</sup> ( $t_{ox} = 200 \text{ nm}$ , SiO <sub>2</sub> )
Field-effect mobility	$\mu_{FE}$	0.02 – 60 cm <sup>2</sup> /Vs
Subthreshold swing	$S_{min}$	$> 3 \text{ V/dec}$
Intrinsic cutoff frequency	$f_{T,int}$	1 MHz ( $V_{ds} = -10 \text{ V}$ )

Data obtained from IsoNanotubes-S CNTFETs with different network density

those two devices has indeed shown the CNTFET in Fig. 4.12e with better performance than the one in Fig. 4.12f, in terms of drain current and on-off ratio. However, as mentioned before, the Raman scan is time-consuming and restricted to small scan area, so that no further investigation was carried out in this study. Exploring the capability of confocal Raman image in evaluation of transistor performance can be included in future.



## Chapter 5

# Performance Analysis of Carbon Nanotube Random Network Transistors

The Chapter 4 gives an overview of characterization of device performance, which provides basis for a systematic performance analysis of random network-based CNTFETs. In recent years, along with the progress in the research for random network-based CNTFETs, prior research works have also studied various influence factors on the performance of random network-based CNTFETs. Among various device parameters, on-off ratio and mobility are two parameters which have been widely used to compare the device performance. Apart from the type and thickness of gate dielectric [3], potential influence factors further include: channel length [8]-[9], [46], channel width [22], [99]-[100], network density [17]-[18], [21], and metallic tube content [21], [100]. Inspired by prior research results, this work focused on the co-influence of network density and metallic tube content on device performance, which provides a new aspect. A systematic study has been carried out on a set of over 100 random network-based CNTFETs with identical gate dielectric and channel geometry. Moreover, the channel length and width was chosen in such an order ( $L = 100 \mu\text{m}$ ,  $W = 1 \text{ mm}$ ) that slight variation would not have strong influence on device performance [8]-[9], [100].

An overview of the design of experiment is given in Section 5.1, followed by performance analysis in Section 5.2 with focus on parameters like drain current, on-off

ratio, and field-effect mobility influenced by network density, metallic tube content, and tube diameter. As mentioned before, the tube diameter has been suggested to be inversely proportional to the band gap of semiconducting CNTs [43], [45]. To describe the co-influence of network density and metallic tube content, a new parameter, the metallic tube density, was introduced as network density multiplying metallic tube content [101]. Finally, Section 5.3 deals with the hysteresis observed in transistor characteristics, including experimental results and theories about the possible origin of hysteresis cited from prior research works. Further investments are required in order to fully understand this complex phenomenon and can be a part of future work.

The aim of this systematic performance analysis is to reveal the way how device performance could be influenced by the parameter of CNT random networks, which enables better understanding of the device mechanism and further optimization of device performance.

## 5.1 Design of experiment

A set of over 100 random network-based CNTFETs were made with IsoNanotubes-S CNTs with two kinds of semiconductor enrichment: 90%-sc and 98%-sc. Although purified CNTs with even higher semiconductor enrichment are commercially available, for instance 99%-sc, but those are with a dramatically increased price. Another available category is the 95%-sc CNTs, which is between the two kinds of CNTs chosen in this work. The basic idea was to create a difference in semiconductor enrichment, or equivalently metallic tube content, to compare their potential influence on device performance. In this case, the 98%-sc CNTs can be considered as with lower metallic tube content, in comparison to the 90%-sc CNTs. Future work can also add the two other available categories (95%-sc and 99%-sc) to proof the results observed in this work.

For each kind of CNTs, a series of varied network density was obtained via the drop-casting method described in Section 3.2.3. The variation of network density can be marked with the equivalent CNT/NMP concentration from 2.5 mg/L to 60 mg/L, or alternatively with the network density from  $0.625 \text{ mg/m}^2$  to  $15 \text{ mg/m}^2$ , as listed in Table 3.2. An overview of the sample size in this study is given in Fig. 5.1. The whole set of

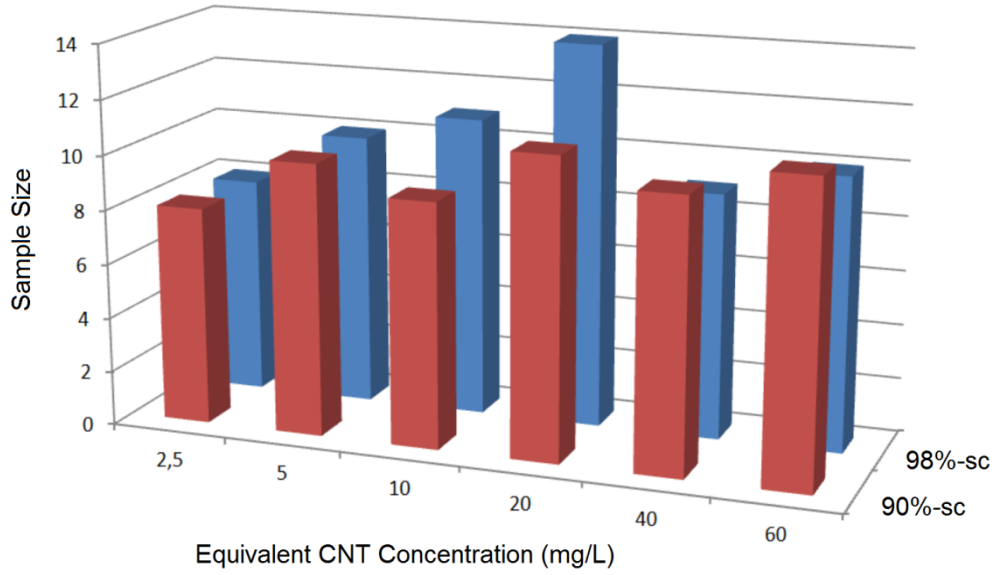


**Figure 5.1** Sample size of the systematic study: depicted as a function of the equivalent CNT concentration (from 2.5 mg/L to 60 mg/L), for 90%-sc (red columns in front) or 98%-sc (blue columns) CNTs respectively. Each group has an average sample size around ten, while the whole size is 121 CNTFETs.

CNTFETs can therefore be divided in 12 groups classified by the semiconductor enrichment and network density, for instance the group (98%-sc, 10 mg/m<sup>2</sup>). Each group of CNTFETs has the same semiconductor enrichment and network density, with a group size around 10 samples. The combination of semiconductor enrichment and network density provides basis for investigation in the co-influence of these two parameters.

In the following part, two similar but different terms are used in relation to metallic CNTs: the metallic tube content and metallic tube density. The metallic tube content is a quantity without unit and often written in percentage. Generally, the metallic tube content can be considered as unity subtracting the semiconductor enrichment. For example, CNTs with 98% semiconductor enrichment has a metallic tube content of 2%; while 90%-sc CNTs has 10% metallic tube content. Therefore the metallic tube content and semiconductor enrichment are sometimes equivalently used to describe the property of CNTs in this study. The metallic tube density is defined as network density multiplying metallic tube content, therefore has the same unit as the network density. For example, the metallic tube density of CNTFETs in this study varied from 0.0125 mg/m<sup>2</sup> to 1.5 mg/m<sup>2</sup>, resulted from a variation of network density from 0.625 mg/m<sup>2</sup> to 15 mg/m<sup>2</sup>. The metallic tube density is generally low in semiconductor-enriched CNT random networks.

A further set of random network-based CNTFETs consisted devices with either SG65 or IsoNanotubes-S CNTs. As mentioned before, the SG65 CNTs have an average tube diameter of 0.8 nm, which is smaller than the average tube diameter of 1.4 nm for IsoNanotubes-S CNTs. The band gap of SG65 CNTs is around 1.0 eV, while the band gap of IsoNanotubes-S CNTs around 0.6 eV. This set of CNTFETs was used to study the influence of band gap of semiconducting CNTs on transistor performance, as will be discussed in Section 5.2.3.

Moreover, all the CNTFETs used in following study had identical device layout with Pd/Au (10 nm/ 30 nm) multilayer contacts, channel length of 100  $\mu\text{m}$ , channel width of 1000  $\mu\text{m}$ , and built on silicon substrate with a 200 nm thick  $\text{SiO}_2$  layer serving as the back-gate.

As mentioned before, all the measurements on random network-based CNTFETs were carried out in ambient environment at room-temperature on a probe station controlled by a Keithley-4200 SCS. The group size as shown in Fig. 5.1 enables calculation of the mean value of performance characterization in each group. The confidence of the mean value can then be described via standard error, or graphically represented in error bars. The standard error is defined as the standard deviation of mean and given as

$$\text{Standard Error} = \frac{\text{Standard Deviation}}{\sqrt{\text{Sample Size}}} = \frac{\text{STDEV}}{\text{SQRT}(N)} \quad (5.01)$$

Where STDEV and SQRT are functions in Excel, and  $N$  is the sample size. An increase in sample size can then lead to decrease in standard error. The error bars include the value range of plus/minus one standard error around the mean value. If two neighboring mean values are within the error bar range of each other, the confidence of the mean value need to be improved, for instance via increase in the sample size, or possibly no significant difference could be expected between those measure points. The mean value of device performance from sample groups built the basis of following performance analysis.



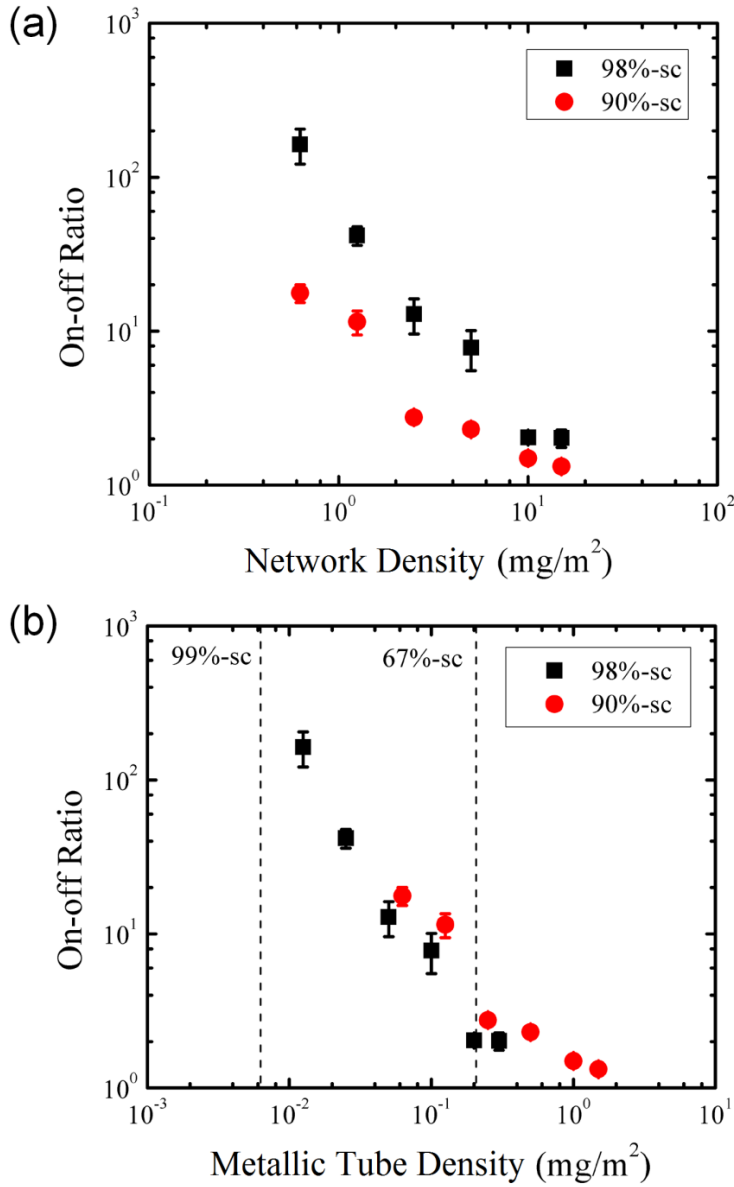
## 5.2 Influence of network properties

### 5.2.1 Influence factors concerning the on-off ratio

Section 4.2.1 summarizes various aspects relating to the characterization of the on-off ratio. In the following study, the on-off ratio of random network-based CNTFETs was extracted from the transfer characteristics measured at  $V_{ds} = -1.0$  V and within a voltage range of  $V_{gs}$  from -10 V to +10 V. Fig. 5.2a summarizes the results of all the groups, represented by the average on-off ratio of each group plotted as a function of the network density. Both on-off ratio and network density are in logarithmic scales. For both kinds of CNTs, the on-off ratio increases with decreasing network density, which has also been observed in previous research works [17], [21]. Moreover, CNTFETs with less metallic tube content also have higher on-off ratio for the same network density [21], [100]. The maximum on-off ratio of the groups with 98%-sc CNTs is of about one order higher than the groups with 90%-sc CNTs. Among all the test groups made in this study, the maximum on-off ratio is approaching  $10^3$ .

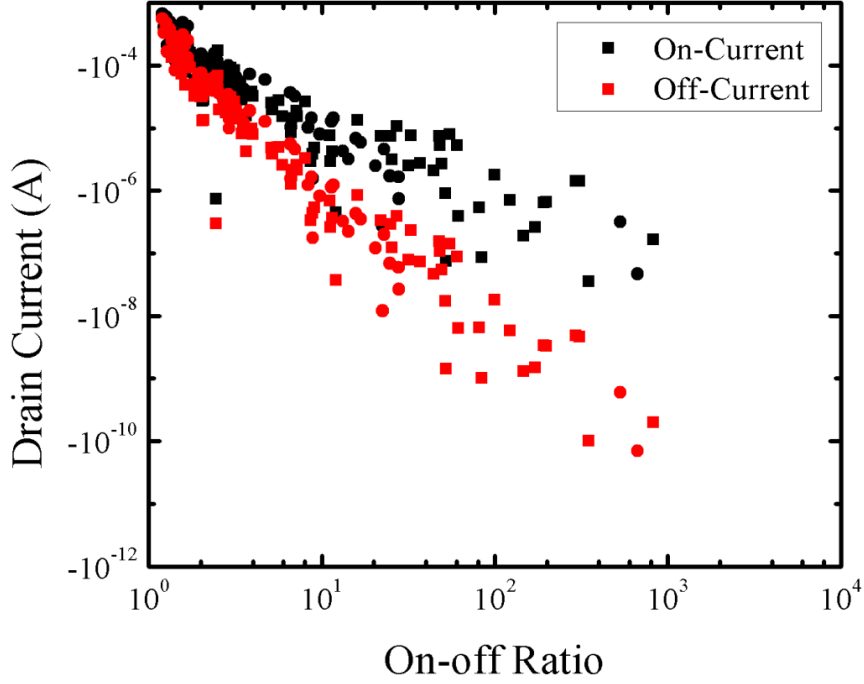
Fig. 5.2b shows the same results from Fig. 5.2a but plotted as a function of metallic tube density instead of network density, again in logarithmic scales. Unlike the previous one, in this case, the results of both kinds of CNTs seem to share the same quasi-linear trace. In other words, the quasi-linear model relating to the metallic tube density can be used to describe or predict the on-off ratio of CNTFETs which have the same device layout but different network density or metallic tube content. For instance, the dashed vertical lines in Fig. 5.2b are threshold lines for prediction of the on-off ratio of CNTFETs with 99%-sc or as-grown (*ca.* 67%-sc) CNTs.

As stated earlier in Section 3.2.3, for device layout used in this study, CNT random networks deposited from 2.5 mg/L CNT/NMP suspension had a network density near the percolation threshold. Therefore the minimum network density was around  $0.625 \text{ mg/m}^2$ , and the minimum metallic tube density was  $0.0125 \text{ mg/m}^2$  for 98%-sc CNTs and  $0.0625 \text{ mg/m}^2$  for 90%-sc CNTs. For 99%-sc and as-grown CNTs, the minimum metallic tube density can then be calculated as  $0.00625 \text{ mg/m}^2$  and  $0.2 \text{ mg/m}^2$ , as drawn in Fig. 5.2b. Combining the threshold line with the quasi-linear trace of the on-off ratio, then the possible maximum on-off ratio for as-grown CNTs is lower than one order of magnitude, while the possible maximum on-off ratio for 99%-sc CNTs is further approaching  $10^3$ . If



**Figure 5.2** The average on-off ratio of random network-based CNTFETs. (a) The average on-off ratio plotted as a function of network density for 98%-sc (black squares) and 90%-sc (red circles) CNTFETs, respectively. (b) The average on-off ratio plotted as a function of metallic tube density. The dashed vertical lines are estimated thresholds for 99%-sc and as-grown (*ca.* 67%-sc) CNTs, respectively.

the semiconductor enrichment is further improved, for instance to 99.9%-sc, the possible maximum on-off ratio can be expected to approach  $10^4$ . However, it is unknown whether the on-off ratio follows the same trace for even higher semiconductor enrichment. On the other hand, other methods concerning the modification of device layout can be applied to achieve the improvement of on-off ratio, as discussed previously in Section 4.2.1.



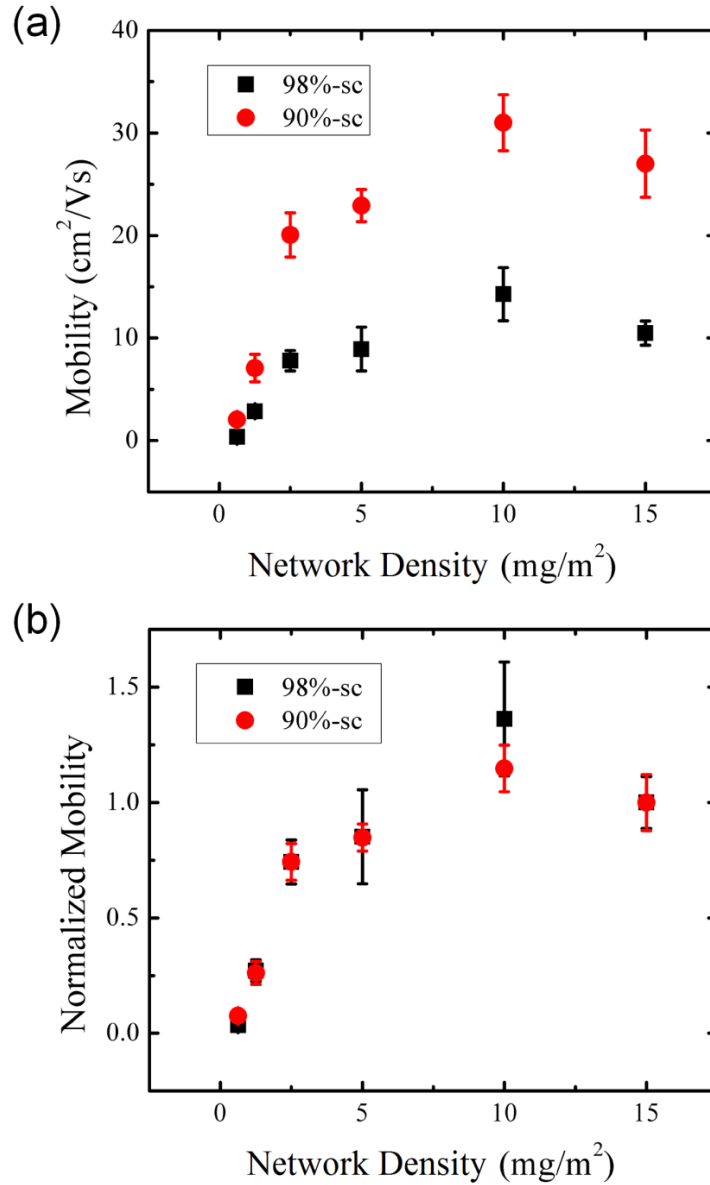
**Figure 5.3** Statistic of drain currents and on-off ratio. The on-current (black) and off-current (red) were measured at  $V_{ds} = -1.0$  V and within the voltage range of  $V_{gs}$  from -10 V to +10 V. The statistic includes results from both 98%-sc (squares) and 90%-sc (circles) CNTFETs with diverse network density.

Fig. 5.3 shows a statistic of drain currents versus on-off ratio, collected from all the random network-based CNTFETs made in this study. As mentioned before, the on-current and off-current were measured at  $V_{ds} = -1.0$  V and within a voltage range of  $V_{gs}$  from -10 V to +10 V. The drain currents and on-off ratio are both plotted in logarithmic scale. As can be seen in Fig. 5.3, both on-current and off-current follow a quasi-linear trace against the on-off ratio. Generally, on-current and off-current both decrease with increase in on-off ratio, while the latter one has a steeper slope. In this case, the on-current varies from below 1 mA to the order of 0.1  $\mu$ A, while the off-current varies from below 1 mA to the order of 0.1 nA. For those CNTFETs with an on-off ratio above 100, the on-current is below 1  $\mu$ A. The level of on-current is generally low in this case and can be improved though modified metal contacts, for instance with increased thickness of electrodes or improved contact to measurement circuit. Moreover, Fig. 5.3 includes results from both 90%-sc and 98%-sc CNTFETs. Despite the difference in semiconductor enrichment, they share the same cluster and no clear deviation is visible between those two kinds of CNTs. The shared cluster in this statistic also indicates the possibility of a common trace relating to the on-off ratio.

### 5.2.2 Influence factors concerning the field-effect mobility

Section 4.2.3 gives an overview of various aspects concerning the characterization of MOSFET mobilities. In this study, field-effect mobility was characterized from random network-based CNTFETs, which was derived from transconductance and gate oxide capacitance  $17.26 \text{ nF/cm}^2$ . Fig. 5.4a shows summarized results of all test groups, plotted as the mean value with error bars for each group. Generally, CNTFETs with lower semiconductor enrichment (90%-sc) have shown clear increase in mobility in comparison to those CNTFETs with same network density but higher semiconductor enrichment (98%-sc). The increase in mobility as a result of decrease in semiconductor enrichment has also been observed by other research group [100]. For the test groups with same semiconductor enrichment, the mobility increases with increasing network density, as shown in prior research works [17], [21]. However, as shown in Fig. 5.4a, the increase in mobility tends to saturate, when the increasing network density reaches certain threshold [101]-[102]. In this study, the threshold of network density was around  $10 \text{ mg/m}^2$ . The average field-effect mobility of 98%-sc CNTFETs varies from  $0.36 \text{ cm}^2/\text{Vs}$  to  $13 \text{ cm}^2/\text{Vs}$ , while the average mobility of 90%-sc CNTFETs varies from  $1.84 \text{ cm}^2/\text{Vs}$  to  $33 \text{ cm}^2/\text{Vs}$ . In this study, the maximum field-effect mobility of single device was  $61 \text{ cm}^2/\text{Vs}$ . For those CNTFETs with on-off ratio above 100, the field-effect mobility varies from  $0.02 \text{ cm}^2/\text{Vs}$  to  $1.14 \text{ cm}^2/\text{Vs}$ . However, as mentioned before in Section 4.2.3, it should be remembered that the field-effect mobility represents an underestimated value of device mobility.

The mean values of 98%-sc and 90%-sc CNTs have some similarities when comparing their traces plotted as a function of network density, as shown in Fig. 5.4a. In fact, when normalized by the mobility of group with maximum network density, the results of both kinds of CNTs almost overlap with each other or within the error bar range, as shown in Fig. 5.4b. From this result, the influence of network properties on device mobility can be interpreted as following: the change of mobility follows a trace determined by the network density, including the increase and saturation as observed; while the semiconductor enrichment determines the amplitude of this trace and acts as a constant factor. Therefore, the change of mobility can be predicted for CNTFETs with same device layout but different network density or semiconductor enrichment.



**Figure 5.4** The average field-effect mobility of random network-based CNTFETs. (a) The average field-effect mobility plotted as a function of network density for 98%-sc (black squares) and 90%-sc (red circles) CNTFETs, respectively. (b) The normalized mobility plotted as a function of network density.

Unlike the on-off ratio that has been mentioned in Section 5.2.1, for CNTFETs with different semiconductor enrichment, the mobility cannot be plotted as a shared quasi-linear function of metallic tube density as shown in Fig. 5.2b, due to the saturation of mobility above a certain threshold of network density. In return, for CNTFETs with different semiconductor enrichment, the on-off ratio cannot be normalized to have a shared trace as shown in Fig. 5.4b, because the semiconductor enrichment has a roll more than just a constant factor as in the case of mobility.

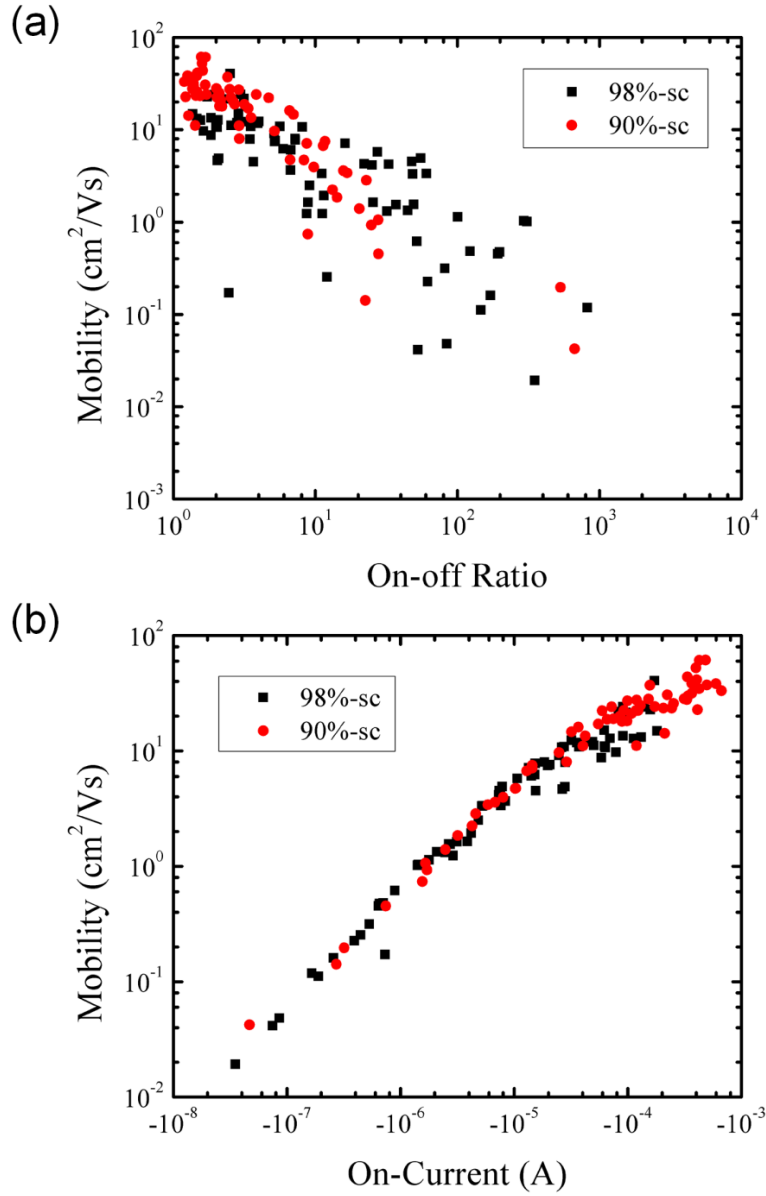


**Figure 5.5** Statistic of field-effect mobility. (a) Mobility versus on-off ratio shows a quasi-linear relation in a loose cluster. (b) Mobility versus on-current shows a quasi-linear relation in a tight cluster. The statistic includes both 98%-sc (black squares) and 90%-sc (red circles) CNTs.

Previous research works have observed an inverse trend between mobility and on-off ratio [21]-[22], [46]. Generally, the mobility decreases while the on-off ratio increases, although both high mobility and high on-off ratio are desired for good performance of transistors. Therefore, a compromise has to be made between mobility and on-off ratio. Such inverse trend has also been observed in this study. As shown in Fig. 5.5a, the mobility and on-off ratio have a quasi-linear inverse relation, when both plotted in logarithmic scales. Fig. 5.5a includes results from both 98%-sc and 90%-sc CNTs and

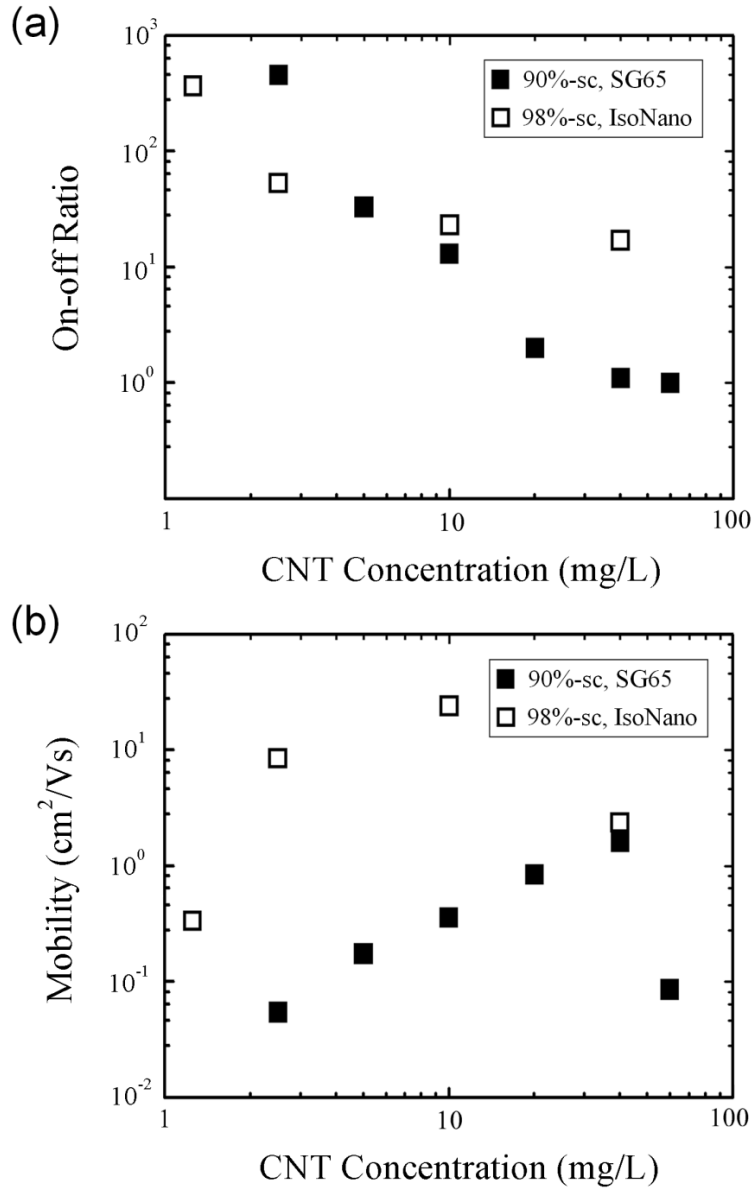
they share the same cluster. In this study, the mobility varies from  $10^{-2}$  cm<sup>2</sup>/Vs to  $10^2$  cm<sup>2</sup>/Vs, while the on-off ratio up to  $10^3$ .

Fig. 5.5b shows a statistic of mobility versus on-current, both plotted in logarithmic scales. Results of both 98%-sc and 90%-sc CNTs are included and they share the same cluster, which is much tighter in comparison to the one in Fig. 5.5a. The on-current varies from 10 nA to 1 mA. In the lower range of scale, the mobility and on-current have a quasi-linear relation. Generally, the mobility increases with increasing on-current. However, in the higher range of scale, the increase in mobility tends to saturate. This result is similar to the one shown in Fig. 5.4b and both of them show saturation in mobility. In other word, the mobility can be increased via increase in network density for random network-based CNTFETs, but limited to a certain threshold.

### 5.2.3 Tube diameter as an influence factor

Another set of random network-based CNTFETs was made to investigate the influence of tube diameter on transistor performance. The device layout was as same as discussed before but made from following two kinds of CNTs: 90%-sc SG65 CNTs and 98%-sc IsoNanotubes-S CNTs. As stated before, the SG65 CNTs have an average tube diameter smaller than the IsoNanotubes-S CNTs, therefore larger band gap than the latter ones. The average tube diameter of SG65 CNTs is 0.8 nm, while the average tube diameter of IsoNanotubes-S CNTs is 1.4 nm, as listed in Table 3.1. As mentioned before in Section 2.1.3, the band gap of semiconducting CNTs can be roughly considered as inversely proportional to the tube diameter. According to (2.02), the band gap is then around 1.0 eV for SG65 CNTs and 0.6 eV for IsoNanotubes-S CNTs.

A variety of network density was achieved via change of the equivalent CNT concentration used for drop-casting CNT random networks. In following discussion, the network density is denoted by the equivalent CNT concentration. The IsoNanotubes-S CNTFETs contain following equivalent concentrations: 1.25 mg/L, 2.5 mg/L, 10 mg/L, and 40 mg/L. The SG65 CNTFETs contain following equivalent concentrations: 2.5 mg/L, 5 mg/L, 10 mg/L, 20 mg/L, 40 mg/L, and 60 mg/L. In Section 3.2.3, the CNT concentration of 2.5 mg/L has been stated as the bottom line for the device layout used in this study to contain a network density near the percolation threshold. This statement is



**Figure 5.6** Transistor performance influenced by tube diameter [102]. The 90%-sc SG65 CNTs (black squares) have an average tube diameter of 0.8 nm, while the 98%-sc IsoNanotubes-S CNTs (white squares) have an average tube diameter of 1.4 nm. (a) The on-off ratio plotted as a function of network density. (b) The field-effect mobility plotted as a function of network density. The network density was denoted by CNT concentration used for drop-casting of CNT random networks.

based on the fact that the CNTFETs from the category of 2.5 mg/L had shown a dropping reliability in comparison to categories with higher network density. In other words, a part of CNT random networks drop-cast from 2.5 mg/L suspension could not form conducting paths across the channel. Therefore, although CNTFETs drop-cast from an equivalent concentration lower than 2.5 mg/L could by chance work, for instance the one with 1.25



mg/L in this Section, they cannot be expected to form a reliable category with large sample size.

To compare the transistor performance, on-off ratio and field-effect mobility were measured from each CNTFET. The results are summarized in Fig. 5.6, plotted as a function of network density denoted by CNT concentration. For both kinds of CNTs, the on-off ratio decreases with increasing network density, as described before. For CNTs with equal tube diameter, the on-off ratio also decreases with decreasing semiconductor enrichment, as shown in Fig. 5.2a. However, for CNTs with different tube diameter, a steeper slope can be seen for those with smaller tube diameter. Therefore, as shown in Fig. 5.6a, the SG65 CNTFETs have higher on-off ratio than the IsoNanotubes-S CNTFETs in the lower range of network density. As mentioned above, the SG65 CNTs have smaller tube diameter than the IsoNanotubes-S CNTs and thus larger band gap than the latter ones. As mentioned before in Section 2.1.3, semiconducting CNTs with larger band gap exhibit stronger semiconducting character and therefore higher on-off ratio [43].

Fig. 5.6b shows the field-effect mobility plotted as a function of network density. Similar as discussed before in Section 5.2.2, for both kinds of CNTs, an increase in mobility with increasing network density and saturation at higher range of network density can be seen. For CNTs with equal tube diameter, the mobility largely increases with decreasing semiconductor enrichment as shown in Fig. 5.4a. However, as shown in Fig. 5.6b, the mobility of SG65 CNTFETs (90%-sc) is generally lower than the IsoNanotubes-S CNTFETs (98%-sc), despite the higher semiconductor enrichment of the latter ones. The decrease in mobility as a result of increasing band gap as observed here is known as a general trend for conventional semiconductors and has also been predicted for CNTs and graphene nanoribbons [90]. The reason for the decrease in mobility can be an increase in the effective mass of the charge carriers with decreasing curvature of energy bands resulted by the increase in band gap, as suggested in [90]. Moreover, the increase in band gap also leads to higher energy barrier at the nanotube-metal interface as shown in Figure 2.4.

In Section 5.2.2, the influence of semiconductor enrichment on mobility has been concluded as a constant factor for those CNTs with equal tube diameter. For CNTs with unequal tube diameter, however, not only the semiconductor enrichment but also the

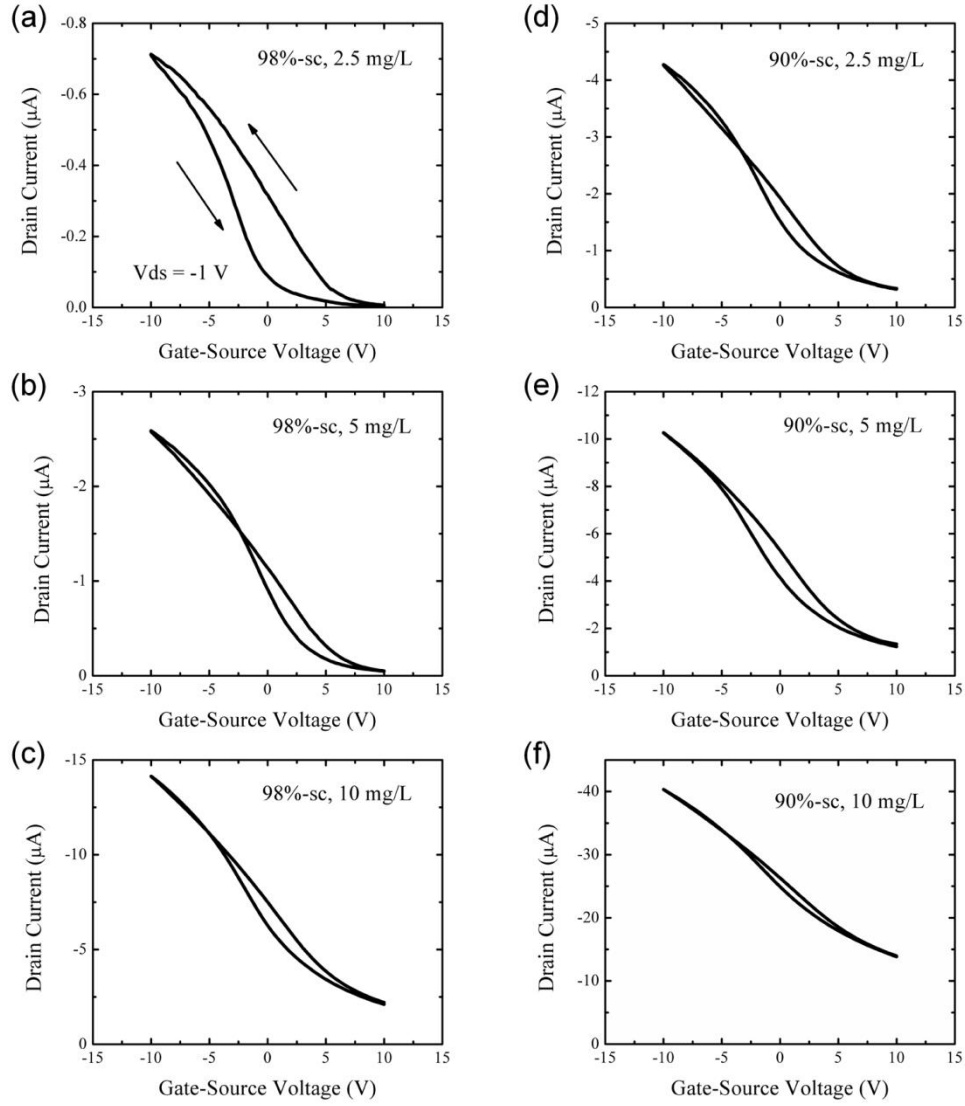
intense of their semiconducting character, for instance the size of band gap, needs to be taken into consideration.

### 5.3 Hysteresis

The measurement of transfer characteristic of CNTFETs, depending on the direction of voltage sweep applied on device, can result in a different curve of drain current. This effect is known as hysteresis and has been observed in CNTFETs both based on single CNT rope and on CNT random networks [103]-[105]. Fig. 5.7a shows an example of hysteresis observed in the transfer characteristic of random network-based CNTFET, measured with a forward voltage sweep from off-state to on-state and with a backward sweep inversely. The curves of drain current forms a hysteresis loop, as the one measured with backward voltage sweep shifted in the direction of negative voltage range. Due to the presence of hysteresis, the transfer characteristics in this study have been generally measured with backwards voltage sweep from on-state to off-state.

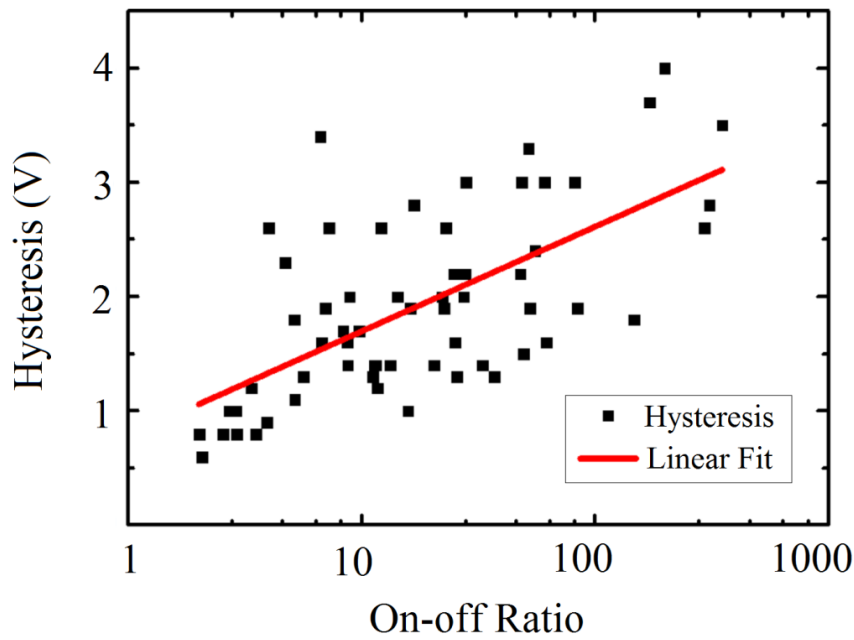
Generally, hysteresis has been considered as an undesired effect, which for instance can lead to a shift in threshold voltage when the CNTFET is operated with different voltage sweep directions. However, hysteresis is also a complex occurrence, of which the origin has not been fully understood yet. Different methods have been developed for characterization of hysteresis. One of them measures the hysteresis as the gap between the threshold voltages from both sweep directions [104]. Another method characterizes the hysteresis as the voltage gap at the half maximum of current change [105]. The applicability of those methods depends on the shape of hysteresis loops. To give an example, for the hysteresis loop shown in Fig. 5.7a, the method of threshold voltage gap is more suitable due to the unsymmetrical shape of the current loop.

Fig. 5.7 shows a summary of hysteresis loops from representative CNTFETs made in this study, including both 90%-sc and 98%-sc CNTs and the CNT random networks deposited from 2.5 mg/L, 5 mg/L, and 10 mg/L suspensions. Generally, the hysteresis decreases with increasing network density or decreasing semiconductor enrichment. The trend is similar to the one of on-off ratio as discussed before. In fact, a statistic of hysteresis gap versus on-off ratio summarized from the CNTFETs made in this study,



**Figure 5.7** Hysteresis observed in random network-based CNTFETs. The transfer characteristics were taken from representative CNTFETs from each group, measured at  $V_{ds} = -1.0$  V. The two arrows in (a) indicate the sweep direction of gate-source voltage as forward from off- to on-state and as backward inversely. (a)-(c) 98%-sc CNT network deposited from 2.5 mg/L, 5 mg/L, and 10 mg/L CNT suspensions. (d)-(f) 90%-sc CNT network deposited from 2.5 mg/L, 5 mg/L, and 10 mg/L CNT suspensions.

exhibits a loose linear cluster between these two parameters as shown in Fig. 5.8, where the on-off ratio plotted in logarithmic scale while the hysteresis gap in linear scale. The hysteresis gap varies from around 0.5 V to 4.0 V, when measured within a voltage range of 20 V. For those CNTFETs made in this study with even higher network density, the hysteresis gap becomes further smaller, which have not been included here.



**Figure 5.8** Statistic of hysteresis and on-off ratio. The rot line shows a linear fit of the cluster. The on-off ratio is plotted in logarithmic scale, while the hysteresis gap in linear scale. The statistic includes random networks with 98%-sc or 90%-sc CNTs, deposited from 2.5 mg/L, 5 mg/L, and 10 mg/L CNT suspensions.

The origin of hysteresis observed in CNTFETs is a matter under debate. One theory suggests that the water molecules attached to the sidewall of CNTs or to the underlying substrate surface result in mobile surface ions trapping by water molecules and cause the hysteresis behaviour [15], [103]. Experiments have shown depression of hysteresis with treatments like heating in vacuum or coating with hydrophobic layer like silane-based SAM, PMMA, or methylsiloxane [87], [103]-[104]. However, as shown in Fig. 5.7, such charge trapping effect should influence preferably the semiconducting nanotubes and especially when the semiconducting species dominates the charge transport within transistor channel, for instance in those CNT random networks with lower network density and higher semiconductor enrichment. Another theory suggests that defects in underlying substrate oxide and therefore a gate-induced effect result in the hysteresis [104]. Such defects include bulk defects embedded near nanotubes and interface defects between nanotubes and substrate. Therefore, hysteresis can be depressed by improving the quality of substrate oxide.

The measurement settings can also influence the hysteresis behaviour of CNTFETs. For instance, an increase in the voltage sweep rate has been shown to enable depression of hysteresis, indicating that the slowly moving species might be the cause of hysteresis behaviour [15], [103]. Alternatively, a pulsed measurement method associated with charge trapping and relaxation mechanism has been developed to reduce hysteresis [105]. A time interval of up to 10 seconds is added after each voltage sweep. Although this technique is rather impractical due to the time consuming, it can help to reveal the mechanism of hysteresis behaviour.



## Chapter 6

# Conclusion and Outlook

As described in Introduction, this thesis has been involved in a research project towards the manufacturability of CNT-based printed electronics. Firstly, a solution-processable technique was developed for fabrication of random network-based CNTFETs. Commercial products of sorted CNTs with high semiconductor enrichment were dissolved in organic solvent without additional surfactants. Although the CNT suspension remained stable only within several hours after preparation and needed to be sonicated again before each use, but the shelf time was longer than those dissolved with additional surfactants. CNT random networks were drop-cast through shadow-mask covered on substrate, followed by evaporation of metal contacts through shadow-mask. The use of shadow-masks provided photoresist-free process. The solution-processable technique developed in this work was simple, fast, and reliable. The random network-based CNTFETs made in this study have stable performance after storage in ambient environment for 20 months. The drop-casting process enables easy control of network density by varying the drop-cast CNT concentration or volume.

At the next step, a systematic study was carried out on a set of over hundred random network-based CNTFETs to investigate the influence factors on transistor performance of CNTFETs. As influence factors were the tube diameter, semiconductor enrichment, and network density, with a focus on the co-influence of the latter two parameters. As transistor performance was drain current, on-off ratio, and field-effect mobility. The on-

off ratio was found to be quasi-linearly related to the metallic tube density, a new parameter defined as network density multiplying semiconductor enrichment. Generally, on-off ratio increases with decreasing metallic tube density. This quasi-linear relationship can be used to predict the on-off ratio of CNTFETs with same device layout but different semiconductor enrichment. Furthermore, the co-influence of network density and semiconductor enrichment indicates that CNTFETs made with lower semiconductor enrichment can sometimes achieve similar on-off ratio to those with higher semiconductor enrichment and higher network density within a certain network density range.

Unlike on-off ratio, the field-effect mobility was found to act as a function of network density multiplying a certain constant given by semiconductor enrichment. Generally, mobility increases with increasing network density or decreasing semiconductor enrichment. However, the increase in mobility tends to saturate above certain threshold value of network density. Therefore decrease in semiconductor enrichment can be more efficient to improve the field-effect mobility. Similar as for on-off ratio, the relationship found relating field-effect mobility can also be used to predict the performance of CNTFETs with same device layout but different network properties.

The tube diameter of semiconducting CNTs is known to be inversely proportional to the band gap. Study on the influence of tube diameter has shown that CNTs with larger band gap have steeper slope in the change of on-off ratio as a function of network density. Moreover, increase in band gap leads to decrease in field-effect mobility.

In addition to conventional semiconductor characterization process on probe station, Raman spectroscopy was applied on CNT random networks. The Raman spectra of CNTs can be used to quickly detect the location and relative amount of CNTs on sample surface. Moreover, comparison of the confocal Raman imaging taken on various spectral features of CNTs can provide information for quality control of deposited CNT random networks.

The performance of random network-based CNTFETs in this work can be further improved via following ways: shorter channel width or striping, thicker metal contacts, and more effective gate control for instance with local gate electrode made with thin-film of high- $\kappa$  dielectrics. Although this thesis deals only with CNTFETs on silicon substrate, the solution-processable fabrication process is also suitable for flexible substrate like plastic foils. Moreover, the drop-casting method can be adapted to printing techniques



like inkjet or roll-to-roll printing that enables high-yield production. However, an important issue concerning flexible CNTFETs is the choice of gate dielectric, which usually requires additional fabrication steps, because the thermally grown SiO<sub>2</sub> layer, as in case of back-gated transistors, is not adaptable to plastic foils.

The future work can include optimization of random network-based CNTFETs from current version, design of device layout for applications like in radio frequency technique, and expanding the solution-processable fabrication process to flexible substrate with high-yield. For the last one, the preparation of suitable CNT ink is required. CNT-based radio frequency devices are expected to be low-cost, flexible, and stable. Moreover, the drop-cast CNT random networks exhibit bio-compatibility, functionality, sensibility, and stability for usage. Therefore, CNTFET-based novel sensors can be included in future work, for instance to improve the sensibility or explore novel sensing mechanisms. Although logic circuits of random network-based CNTFETs have already been realized on plastic foils, most devices so far have been based on p-type metal-oxide-semiconductor (PMOS) technique only. Therefore, *n*-doping of random network-based CNTFETs and realization of CMOS logic circuit on flexible substrate can be an interesting part of future work. The performance analysis in this study has shown some rules relating to the influence factors on transistor performance. The future work can expand current study to sample set with different semiconductor enrichment, for instance 95%-sc and 99%-sc, to check the rules.



# Appendix A

## How to make a CNTFET

### **1. Substrate preparation**

- 1) Silicon wafer cut to  $1\text{ cm} \times 1\text{ cm}$  pieces.
- 2) Wafer sonicated in Acetone and IPA, 5 minutes each, then blown dry, and baked on hotplate at  $150\text{ }^{\circ}\text{C}$  for 10 minutes.
- 3) Wafer treated with  $\text{O}_2$ -Plasma: 0.3 mbar, 50% power, for 10 minutes. Or
- 4) RCA clean with 1:1:5 solution of  $\text{NH}_4\text{OH} + \text{H}_2\text{O}_2 + \text{DI-H}_2\text{O}$  heated to  $60\text{ }^{\circ}\text{C}$  for 20 minutes, then rinsed in organic solvent (Acetone/IPA) and blown dry.
- 5) Wafer covered with shadow-mask for drop-casting, or treated with APTES before.

### **2. APTES treatment (optional)**

- 1) Wafer soaked in APTES for 10 minutes or longer.
- 2) Wafer sonicated in IPA for 5 minutes, blown dry, on hotplate at  $150\text{ }^{\circ}\text{C}$  for 10 minutes.

### **3. Preparation of CNT/NMP Suspension**

- 1) NMP filtered through 0.2  $\mu\text{m}$  filter.
- 2) CNT powder added in NMP and sonicated in ice bath for 90 minutes or longer.

### **4. Drop-casting of CNT suspension**

- 1) Pipette adjusted to 0.5  $\mu\text{L}$  volume, drop-cast on silicon wafer over shadow-mask.
- 2) Wafer baked on hotplate at 100  $^{\circ}\text{C}$  for 5 minutes.
- 3) Repeat the above steps if multi-casting process is required.
- 4) Wafer post-baked on hotplate at 150  $^{\circ}\text{C}$  for 10 minutes.
- 5) Wafer covered with shadow-mask for deposition of metal contacts.

### **5. Deposition of metal contacts**

- 1) Wafer mounted in the thermal evaporation chamber.
- 2) The evaporation process should start when pumped down to lower than  $7\text{e}^{-7}$  mbar.
- 3) Evaporation of 10 nm Pd-layer with a rate of 0.5  $\text{\AA}/\text{sec}$ .
- 4) Evaporation of 30 nm Au-layer with a rate of 1.0  $\text{\AA}/\text{sec}$ .

## Appendix B

### List of Work Functions

Work function of SWNT rope is given as 5.10 eV [57]

Work function of elements [58]

Ca	2.87 eV
Al	4.06 – 4.26 eV
Ti	4.33 eV
Cr	4.50 eV
Ag	4.52 – 4.74 eV
Mo	4.36 – 4.95 eV
Cu	4.53 – 5.10 eV
W	4.32 – 5.22 eV
Au	5.31 – 5.47 eV
Pd	5.22 – 5.60 eV
Pt	5.12 – 5.93 eV
Si	4.60 – 4.85 eV



## Appendix C

### List of Symbols

$a_{c-c}$	minimum carbon-carbon distance ( <i>ca.</i> 1.42 Å)
$B$	body effect factor
$C_b$	bulk capacitance (F/cm <sup>2</sup> )
$C_{dsp}$	parasitic drain-source capacitance (F)
$C_{gd}$	gate-drain capacitance (F)
$C_{gdp}$	parasitic gate-drain capacitance (F)
$C_{gs}$	gate-source capacitance (F)
$C_{gsp}$	parasitic gate-source capacitance (F)
$C_{it}$	interface trap capacitance (F/cm <sup>2</sup> )
$C_{ox}$	oxide capacitance (F)
$C_{ox}$	oxide capacitance per unit area (F/cm <sup>2</sup> )
$C_Q$	quantum capacitance ( $4.0 \times 10^{-12}$ F/cm)
$d_t$	(average) tube diameter (nm)
$E$	(band) energy (eV)
$E_c$	conduction band edge (eV)
$E_F$	Fermi energy (eV)
$E_{gap}$	band gap (eV)
$E_L$	laser energy (eV)
$E_v$	valence band edge (eV)

$E_{\text{vac}}$	vacuum level (eV)
$f_{\text{max}}$	maximum oscillation frequency (Hz)
$f_{\text{T}}$	cutoff frequency (Hz)
$f_{\text{T,int}}$	intrinsic cutoff frequency (Hz)
$g_{\text{d}}$	drain conductance (S)
$g_{\text{m}}$	transconductance (S)
$g_{\text{m,max}}$	maximum transconductance (S)
$h$	Planck's constant ( $6.626 \times 10^{-34}$ J·s)
$I$	current (A)
$I_{\text{d}}$	drain current (A)
$I_{\text{on}}$	on-current (A)
$I_{\text{off}}$	off-current (A)
$k$	Boltzmann's constant ( $8.617 \times 10^{-5}$ eV/K, $1.38 \times 10^{-23}$ J/K)
$L$	channel length ( $\mu\text{m}$ )
$l_{\text{t}}$	(average) tube length ( $\mu\text{m}$ )
$m_{\text{t}}$	(average) tube weight (g)
$N_{\text{A}}$	Avogadro's constant ( $6.022 \times 10^{23}$ mol <sup>-1</sup> )
NA	numerical aperture
(n, m)	chiral indices
$q$	elemental electronic charge ( $1.602 \times 10^{-19}$ C)
$R_{\text{d}}$	drain series resistance ( $\Omega$ )
$R_{\text{g}}$	gate series resistance ( $\Omega$ )
$R_{\text{gd}}$	gate-drain resistance ( $\Omega$ )
$R_{\text{gs}}$	gate-source resistance ( $\Omega$ )
$R_{\text{q}}$	quantum limit of resistance ( $\Omega$ )
$R_{\text{s}}$	source series resistance ( $\Omega$ )
$r_{\text{t}}$	(average) tube radius (nm)
$S$	subthreshold swing (V/dec)
$S_{\text{min}}$	minimum subthreshold swing (V/dec)
$s$	resolution ( $\mu\text{m}$ )
$T$	temperature (K)
$t_{\text{ox}}$	oxide thickness (nm)
$V$	voltage (V)
$V_{\text{ds}}$	drain-source voltage (V)



$V_{\text{dsi}}$	intrinsic drain-source voltage (V)
$V_{\text{gs}}$	gate-source voltage (V)
$V_{\text{gsi}}$	intrinsic gate-source voltage (V)
$V_{\text{int}}$	intercept gate-source voltage (V)
$V_{\text{th}}$	threshold voltage (V)
$W$	channel width ( $\mu\text{m}$ )
$\gamma_0$	minimum carbon-carbon overlap energy ( <i>ca.</i> 2.9 eV)
$\epsilon_0$	permittivity of free space ( $8.854 \times 10^{-14}$ F/cm)
$\Theta$	contact angle ( $^\circ$ )
$\theta$	chiral angle ( $^\circ$ )
$\kappa_{\text{ox}}$	oxide dielectric constant
$A_0$	average tube spacing ( $\mu\text{m}$ )
$\lambda$	wavelength (nm)
$\mu_{\text{eff}}$	effective mobility ( $\text{cm}^2/\text{V}\cdot\text{s}$ )
$\mu_{\text{FE}}$	field-effect mobility ( $\text{cm}^2/\text{V}\cdot\text{s}$ )
$\mu_{\text{sat}}$	saturation mobility ( $\text{cm}^2/\text{V}\cdot\text{s}$ )
$\rho$	density of states
$\Phi_{\text{B}}$	barrier height (eV)
$\Phi_{\text{m}}$	metal work function (eV)
$\Phi_{\text{s}}$	semiconductor work function (eV)
$\chi$	semiconductor electron affinity (eV)
$\omega_{\text{R}}$	(relative) Raman shift ( $\text{cm}^{-1}$ )



## Appendix D

### Abbreviations and Acronyms

AFM	atomic force microscope
APTES	3-aminopropyl triethoxysilane
BTS	11-bromoundecyl trimethoxysilane
CMOS	complementary metal-oxide-semiconductor
CNT	carbon nanotube
CNTFET	carbon nanotube field-effect transistor
CoMoCAT	Co-Mo catalyst
CTS	11-cyanoundecyltrimethoxysilane
CVD	chemical vapor deposition
DCB	1,2-dichlorobenzene
DEP	dielectrophoresis
DGU	density gradient ultracentrifugation
DMF	dimethylformamide
DNA	deoxyribonucleic acid
DOS	density of states
DR1	second-order one-phonon scattering
DR2	second-order two-phonon scattering
FESEM	field emission scanning electron microscope
FET	field-effect transistor

GNR	graphene nanoribbon
HiPCO	high-pressure carbon monoxide
IPA	isopropyl alcohol
IR	infrared
ITRS	International Technology Roadmap for Semiconductors
LED	light-emitting diode
MOSFET	metal-oxide-semiconductor field-effect transistor
MWNT	multi-walled carbon nanotube
NMP	<i>N</i> -methylpyrrolidinone
OTFT	organic thin-film transistor
OTS	<i>n</i> -octadecyltrichlorosilane
P3HT	poly (3-hexylthiophene)
PEI	polyethylene imine
PEN	polyethylene naphthalate
PET	polyethylene terephthalate
PI	polyimide
PMMA	polymethylmetacrylate
PMOS	p-type metal-oxide-semiconductor
RBM	radial breathing mode
RFID	radio frequency identification
SAM	self-assembled monolayer
SCS	semiconductor characterization system
SDBS	sodium dodecyl benzene sulphonate
SDS	sodium dodecyl sulfate
SEM	scanning electron microscope
SR	first-order scattering
STM	scanning tunneling microscope
SWNT	single-walled carbon nanotube
TEM	transmission electron microscope
TGA	thermogravimetric analysis

# Appendix E

## List of Publications

### Conference proceedings papers

1. **Q. Gong**, E. Albert, B. Fabel, A. Abdellah, P. Lugli, M. B. Chan-Park, and G. Scarpa, “Solution-processable random carbon nanotube networks for thin-film transistors,” in *Proceedings of the IEEE Conference on Nanotechnology*, Portland, USA, 2011, pp. 378-381.
2. P. Lugli, A. Abdellah, E. Albert, G. Csaba, C. Erlen, B. Fabel, **Q. Gong**, M. B. Chan-Park, P. R. Divina, and G. Scarpa, “Circuit and system implementations of molecular devices,” in *Proceedings of the 12<sup>th</sup> International Symposium on Integrated Circuits*, Singapore, Singapore, 2009, pp. 125-128.

### Peer reviewed journal papers

1. **Q. Gong**, V. D. Bhatt, E. Albert, A. Abdellah, B. Fabel, P. Lugli, and G. Scarpa, “On the performance of solution-processable random network carbon nanotube transistors: unveiling the role of network density and metallic tube content,” *IEEE Transactions on Nanotechnology*, vol. 13, pp. 1181-1185, Nov. 2014.

2. N. Mzoughi, A. Abdellah, **Q. Gong**, H. Grothe, P. Lugli, B. Wolf, and G. Scarpa, “Characterization of novel impedimetric pH-sensors based on solution-processable biocompatible thin-film semiconducting organic coatings,” *Sensors and Actuators B: Chemical*, vol. 171-172, pp. 537-543, Aug.-Sep. 2012.

### **Book chapter**

1. **Q. Gong**, E. Albert, A. Abdellah, P. Lugli, M. B. Chan-Park, and G. Scarpa, “Solution-processed random carbon nanotube networks used in thin-film transistor,” in *Nanoelectronic Device Applications Handbook*, J. Morris and K. Iniewski, Ed. New York: CRC Press, 2013, chapter 42.

## Appendix F

### Bibliography

- [1] S. Iijima, “Helical microtubules of graphitic carbon,” *Nature*, vol. 354, pp. 56-58, Nov. 1991.
- [2] S. Iijima and T. Ichihashi, “Single-shell carbon nanotubes of 1-nm diameter,” *Nature*, vol. 363, pp. 603-605, Jun. 1993.
- [3] J. Appenzeller, J. Knoch, V. Derycke, R. Martel, S. Wind, and P. Avouris, “Field-modulated carrier transport in carbon nanotube transistors,” *Phys. Rev. Lett.*, vol. 89, 126801, Sep. 2002.
- [4] Z. Wu, Z. Chen, X. Du, J. M. Logan, J. Sippel, M. Nikolou, K. Kamaras, J. R. Reynolds, D. B. Tanner, A. F. Hebard, and A. G. Rinzler, “Transparent, conductive carbon nanotube films,” *Science*, vol. 305, pp. 1273-1276, Aug. 2004.
- [5] K. H. Baloch, N. Voskanyan, M. Bronsgeest, and J. Cumings, “Remote Joule heating by a carbon nanotube,” *Nature Nanotechnology*, vol. 7, pp. 316-319, May 2012.
- [6] M. E. Roberts, M.C. LeMieux, and Z. Bao, “Sorted and aligned single-walled carbon nanotube networks for transistor-based aqueous chemical sensors,” *ACS Nano*, vol. 3, pp. 3287-3293, Oct. 2009.
- [7] C. B. Jacobs, M. J. Peairs, and B. J. Venton, “Review: Carbon nanotube based electrochemical sensors for biomolecules,” *Analytica Chimica Acta*, vol. 662, pp. 105-127, Mar. 2010.

- [8] C. Wang, J. Chien, K. Takei, T. Takahashi, J. Nah, A. M. Niknejad, and A. Javey, "Extremely bendable, high-performance integrated circuits using semiconducting carbon nanotube networks for digital, analog, and radio-frequency applications," *Nano Lett.*, vol. 12, pp. 1527-1533, Mar. 2012.
- [9] S. Jang, H. Jang, Y. Lee, D. Suh, S. Baik, B. H. Hong, and J. Ahn, "Flexible, transparent single-walled carbon nanotube transistors with graphene electrodes," *Nanotechnology*, vol. 21, 425201, Oct. 2010.
- [10] M. M. J. Treacy, T. W. Ebbesen, and J. M. Gibson, "Exceptionally high Young's modulus observed for individual carbon nanotubes," *Nature*, vol. 381, pp. 678-680, Jun. 1996.
- [11] International Technology Roadmap for Semiconductors, 2009.
- [12] International Technology Roadmap for Semiconductors, 2011.
- [13] M. Freitag, "Carbon nanotube electronics and devices," in *Carbon Nanotubes: Properties and Applications*, M. J. O'Connell, Ed. New York: CRC Press, 2006, ch. 4.
- [14] T. Dürkop, S. A. Getty, E. Cobas, and M. S. Fuhrer, "Extraordinary mobility in semiconducting carbon nanotubes," *Nano Lett.*, vol. 4, pp. 35-39, Jan. 2004.
- [15] D. Hecht and G. Grüner, "Solution cast films of carbon nanotubes for transparent conductors and thin film transistors," in *Flexible Electronics: Materials and Applications*, W. S. Wong and A. Salleo, Eds. New York: Springer, 2009, ch. 10.
- [16] P. Lugli, A. Abdellah, E. Albert, G. Csaba, C. Erlen, B. Fabel, Q. Gong, M. B. Chan-Park, P. R. Divina, and G. Scarpa, "Circuit and system implementations of molecular devices," in *Proc. 12<sup>th</sup> Int. Symposium on Integrated Circuits*, Singapore, 2009, pp. 125-128.
- [17] T. Takahashi, K. Takei, A. G. Gillies, R. S. Fearing, and A. Javey, "Carbon nanotube active-matrix backplanes for conformal electronics and sensors," *Nano Lett.*, vol. 11, pp. 5408-5413, Dec. 2011.
- [18] M. Jung, J. Kim, J. Noh, N. Lim, C. Lim, G. Lee, J. Kim, H. Kang, K. Jung, A. D. Leonard, J. M. Tour, and G. Cho, "All-printed and roll-to-roll-printable 13.56-MHz-operated 1-bit RF tag on plastic foils," *IEEE Trans. Electron Devices*, vol. 57, pp. 571-580. Mar. 2010.
- [19] N. Mzoughi, A. Abdellah, Q. Gong, H. Grothe, P. Lugli, B. Wolf, and G. Scarpa, "Characterization of novel impedimetric pH-sensors based on solution-processable biocompatible thin-film semiconducting organic coatings," *Sensors and Actuators B: Chemical*, vol. 171-172, pp. 537-543, Aug.-Sep. 2012.



- [20] M. S. Arnold, A. A. Green, J. F. Hulvat, S. I. Stupp, and M. C. Hersam, "Sorting carbon nanotubes by electronic structure using density differentiation," *Nature Nanotechnology*, vol. 1, pp. 60-65, Oct. 2006.
- [21] N. Rouhi, D. Jain, and P. J. Burke, "High-performance semiconducting nanotube inks: Progress and prospects," *ACS Nano*, vol. 5, pp. 8471-8487, Nov. 2011.
- [22] Q. Cao, H. Kim, N. Pimparkar, J. P. Kulkarni, C. Wang, M. Shim, K. Roy, M. A. Alam, and J. A. Rogers, "Medium-scale carbon nanotube thin-film integrated circuits on flexible plastic substrates," *Nature*, vol. 454, pp. 495-500, Jul. 2008.
- [23] F. Hennrich, C. Chan, V. Moore, M. Rolandi, and M. O'Connell, "The element carbon," in *Carbon Nanotubes: Properties and Applications*, M. J. O'Connell, Ed. New York: CRC Press, 2006, ch. 1.
- [24] P. Ehrenfreund and B. H. Foing, "Fullerenes and cosmic carbon," *Science*, vol. 329, pp. 1159-1160, Sep. 2010.
- [25] O. A. Shenderova, V. V. Zhirnov, and D. W. Brenner, "Carbon nanostructures," *Critical Reviews in Solid State and Materials Science*, vol. 27(3-4), pp. 227-356, 2002.
- [26] W. Kim, H. C. Choi, M. Shim, Y. Li, D. Wang, and H. Dai, "Synthesis of ultralong and high percentage of semiconducting single-walled carbon nanotubes," *Nano Lett.*, vol. 2, pp. 703-708, Jul. 2002.
- [27] P. Kim and C. M. Lieber, "Nanotube nanotweezers," *Science*, vol. 286, pp. 2148-2150, Dec. 1999.
- [28] H. Dai, J. H. Hafner, A. G. Rinzler, D. T. Colbert, and R. E. Smalley, "Nanotubes as nanoprobe in scanning probe microscopy," *Nature*, vol. 384, pp. 147-150, Nov. 1996.
- [29] R. H. Baughman, A. A. Zakhidov, and W. A. de Heer, "Carbon nanotubes – the route toward applications," *Science*, vol. 297, pp. 787-792, Aug. 2002.
- [30] P. R. Bandaru, C. Daraio, S. Jin, and A. M. Rao, "Novel electrical switching behaviour and logic in carbon nanotube Y-junctions," *Nature Materials*, vol. 4, pp. 663-666, Sep. 2005.
- [31] K. Jensen, J. Weldon, H. Garcia, and A. Zettl, "Nanotube radio," *Nano Lett.*, vol. 7, pp. 3508-3511, Nov. 2007.
- [32] S. Wang, Q. Zeng, L. Yang, Z. Zhang, Z. Wang, T. Pei, L. Ding, X. Liang, M. Gao, Y. Li, and L. Peng, "High-performance carbon nanotube light-emitting diodes with asymmetric contacts," *Nano Lett.*, vol. 11, pp. 23-29, Jan. 2011.

- [33] Y. Hayamizu, T. Yamada, K. Mizuno, R. C. Davis, D. N. Futaba, M. Yumura, and K. Hata, "Integrated three-dimensional microelectromechanical devices from processable carbon nanotube wafers," *Nature Nanotechnology*, vol. 3, pp. 289-294, May 2008.
- [34] D. V. Kosynkin, A. L. Higginbotham, A. Sinitskii, J. R. Lomeda, A. Dimiev, B. K. Price, and J. M. Tour, "Longitudinal unzipping of carbon nanotubes to form graphene nanoribbons," *Nature*, vol. 458, pp. 872-876, Apr. 2009.
- [35] H. Dai, "Nanotube growth and characterization," in *Topics Appl. Phys.*, vol. 80, *Carbon Nanotubes*, M. S. Dresselhaus, G. Dresselhaus, and P. Avouris, Eds. Berlin, Germany: Springer, 2001, pp. 29-53.
- [36] C. Journet, W. K. Maser, P. Bernier, A. Loiseau, M. Lamy de la Chapelle, S. Lefrant, P. Deniard, R. Lee, and J. E. Fischer, "Large-scale production of single-walled carbon nanotubes by the electric-arc technique," *Nature*, vol. 388, pp. 756-758, Aug. 1997.
- [37] A. Thess, R. Lee, P. Nikolaev, H. Dai, P. Petit, J. Robert, C. Xu, Y. H. Lee, S. G. Kim, A. G. Rinzler, D. T. Colbert, G. E. Scuseria, D. Tománek, J. E. Fischer, and R. E. Smalley, "Crystalline ropes of metallic carbon nanotubes," *Science*, vol. 273, pp. 483-487, Jul. 1996.
- [38] C. D. Scott, S. Arepalli, P. Nikolaev, and R. E. Smalley, "Growth mechanisms for single-wall carbon nanotubes in a laser-ablation process," *Appl. Phys. A*, vol. 72, pp. 573-580, May 2001.
- [39] J. Kong, H. T. Soh, A. M. Cassell, C. F. Quate, and H. Dai, "Synthesis of individual single-walled carbon nanotubes on patterned silicon wafers," *Nature*, vol. 395, pp. 878-881, Oct. 1998.
- [40] J. P. Edgeworth, N. R. Wilson, and J. V. Macpherson, "Controlled growth and characterization of two-dimensional single-walled carbon-nanotube networks for electrical applications," *Small*, vol. 3, pp. 860-870, May 2007.
- [41] N. R. Franklin and H. Dai, "An enhanced CVD approach to extensive nanotube networks with directionality," *Adv. Mater.*, vol. 12, pp. 890-894, Jun. 2000.
- [42] M. Burghard, "Electronic and vibrational properties of chemically modified single-wall carbon nanotubes," *Surface Science Reports*, vol. 58, 1-109, Aug. 2005.
- [43] J. W. G. Wildöer, L. C. Venema, A. G. Rinzler, R. E. Smalley, and C. Dekker, "Electronic structure of atomically resolved carbon nanotubes," *Nature*, vol. 391, pp. 59-62, Jan. 1998.
- [44] R. Martel, T. Schmidt, H. R. Shea, T. Hertel, and P. Avouris, "Single- and multi-wall carbon nanotube field-effect transistors," *Appl. Phys. Lett.*, vol. 73, pp. 2447-2449, Oct. 1998.

- [45] J. Charlier, X. Blase, and S. Roche, "Electronic and transport properties of nanotubes," *Rev. Mod. Phys.*, vol. 79, pp. 677-732, Apr.-Jun. 2007.
- [46] D. Sun, M. Y. Timmermans, Y. Tian, A. G. Nasibulin, E. I. Kauppinen, S. Kishimoto, T. Mizutani, and Y. Ohno, "Flexible high-performance carbon nanotube integrated circuits," *Nature Nanotechnology*, vol. 6, pp. 156-161, Mar. 2011.
- [47] V. Derycke, R. Martel, J. Appenzeller, and P. Avouris, "Carbon nanotube inter- and intramolecular logic gates," *Nano Lett.*, vol. 1, pp. 453-456, Sep. 2001.
- [48] S. J. Wind, J. Appenzeller, R. Martel, V. Derycke, and P. Avouris, "Vertical scaling of carbon nanotube field-effect transistors using top gate electrodes," *Appl. Phys. Lett.*, vol. 80, pp. 3817-3819, May 2002.
- [49] A. Javey, H. Kim, M. Brink, Q. Wang, A. Ural, J. Guo, P. McIntyre, P. McEuen, M. Lundstrom, and H. Dai, "High- $\kappa$  dielectrics for advanced carbon-nanotube transistors and logic gates," *Nature Materials*, vol. 1, pp. 241-246, Dec. 2002.
- [50] A. D. Franklin and Z. Chen, "Length scaling of carbon nanotube transistors," *Nature Nanotechnology*, vol. 5, pp. 858-862, Dec. 2010.
- [51] Z. Chen, D. Farmer, S. Xu, R. Gordon, P. Avouris, and J. Appenzeller, "Externally assembled gate-all-around carbon nanotube field-effect transistor," *IEEE Elec. Dev. Lett.*, vol. 29, pp. 183-185, Feb. 2008.
- [52] W. B. Jackson, "Flexible transition metal oxide electronics and imprint lithography," in *Flexible Electronics: Materials and Applications*, W. S. Wong and A. Salleo, Eds. New York: Springer, 2009, ch. 5.
- [53] A. D. Franklin, M. Luisier, S. Han, G. Tulevski, C. M. Breslin, L. Gignac, M. S. Lundstrom, and W. Haensch, "Sub-10 nm carbon nanotube transistor," *Nano Lett.*, vol. 12, pp. 758-762, Feb. 2012.
- [54] M. Shim, A. Javey, N. W. S. Kam, and H. Dai, "Polymer functionalization for air-stable n-type carbon nanotube field-effect transistors," *J. Am. Chem. Soc.*, vol. 123, pp. 11512-11513, Nov. 2001.
- [55] V. Derycke, R. Martel, J. Appenzeller, and P. Avouris, "Controlling doping and carrier injection in carbon nanotube transistors," *Appl. Phys. Lett.*, vol. 80, pp. 2773-2775, Apr. 2002.
- [56] D. K. Schroder, *Semiconductor Material and Device Characterization*, New York: John Wiley & Sons, 1998.

- [57] D. Lovall, M. Buss, E. Graugnard, R. P. Andres, and R. Reifenberger, "Electron emission and structural characterization of a rope of single-walled carbon nanotubes," *Phys. Rev. B*, vol. 61, pp. 5683-5691, Feb. 2000.
- [58] D. R. Lide, Ed., *Handbook of Chemistry and Physics*, CRC, 2008, pp. 12-114.
- [59] S. Heinze, J. Tersoff, R. Martel, V. Derycke, J. Appenzeller, and P. Avouris, "Carbon nanotube as Schottky barrier transistors," *Phys. Rev. Lett.*, vol. 89, 106801, Sep. 2002.
- [60] J. Li, Y. Lu, Q. Ye, M. Cinke, J. Han, and M. Meyyappan, "Carbon nanotube sensors for gas and organic vapor detection," *Nano Lett.*, vol. 3, pp. 929-933, Jul. 2003.
- [61] X. Li, L. Zhang, X. Wang, I. Shimoyama, X. Sun, W. Seo, and H. Dai, "Langmuir-Blodgett assembly of densely aligned single-walled carbon nanotubes from bulk materials," *J. Am. Chem. Soc.*, vol. 129, pp. 4890-4891, Apr. 2007.
- [62] M. Engel, J. P. Small, M. Steiner, M. Freitag, A. A. Green, M. C. Hersam, and P. Avouris, "Thin film nanotube transistors based on self-assembled, aligned, semiconducting carbon nanotube arrays," *ACS Nano*, vol. 2, pp. 2445-2452, Dec. 2008.
- [63] C. Rutherglen, D. Jain, and P. Burke, "Nanotube electronics for radiofrequency applications," *Nature Nanotechnology*, vol. 4, pp. 811-819, Dec. 2009.
- [64] Y. Huang, X. Duan, Q. Wei, and C. M. Lieber, "Directed assembly of one-dimensional nanostructures into functional networks," *Science*, vol. 291, pp. 630-633, Jan. 2001.
- [65] R. Krupke, F. Hennrich, H. v. Löhneysen, and M. M. Kappes, "Separation of metallic from semiconducting single-walled carbon nanotubes," *Science*, vol. 301, pp. 344-347, Jul. 2003.
- [66] C. Kocabas, S. Hur, A. Gaur, M. A. Meitl, M. Shim, and J. A. Rogers, "Guided growth of large-scale, horizontally aligned arrays of single-walled carbon nanotubes and their use in thin-film transistors," *Small*, vol. 1, pp. 1110-1116, Nov. 2005.
- [67] S. J. Kang, C. Kocabas, H. Kim, Q. Cao, M. A. Meitl, D. Khang, and J. A. Rogers, "Printed multilayer superstructures of aligned single-walled carbon nanotubes for electronic applications," *Nano Lett.*, vol. 7, pp. 3343-3348, Nov. 2007.
- [68] C. L. Pint, Y. Xu, S. Moghazy, T. Cherukuri, N. T. Alvarez, E. H. Haroz, S. Mahzooni, S. K. Doorn, J. Kono, M. Pasquali, and R. H. Hauge, "Dry contact transfer printing of aligned carbon nanotube patterns and characterization of their optical properties for diameter distribution and alignment," *ACS Nano*, vol. 4, pp. 1131-1145, Feb. 2010.
- [69] M. C. Hersam, "Progress towards monodisperse single-walled carbon nanotubes," *Nature Nanotechnology*, vol. 3, pp. 387-394, Jul. 2008.

- [70] P. G. Collins, M. S. Arnold, and P. Avouris, "Engineering carbon nanotubes and nanotube circuits using electrical breakdown," *Science*, vol. 292, pp. 706-709, Apr. 2001.
- [71] S. M. Bachilo, L. Balzano, J. E. Herrera, F. Pompeo, D. E. Resasco, and R. B. Weisman, "Narrow  $(n,m)$ -distribution of single-walled carbon nanotubes grown using a solid supported catalyst," *J. Am. Chem. Soc.*, vol. 125, pp. 11186-11187, Sep. 2003.
- [72] L. Huang, H. Zhang, B. Wu, Y. Liu, D. Wei, J. Chen, Y. Xue, G. Yu, H. Kajiura, and Y. Li, "A generalized method for evaluating the metallic-to-semiconducting ratio of separated single-walled carbon nanotubes by UV-vis-NIR characterization," *J. Phys. Chem. C*, vol. 114, pp. 12095-12098, Jul. 2010.
- [73] K. Yanagi, Y. Miyata, T. Tanaka, S. Fujii, D. Nishide, and H. Kataura, "Colors of carbon nanotubes," *Diamond & Related Materials*, vol. 18, pp. 935-939, May-Aug. 2009.
- [74] M. S. Dresselhaus, G. Dresselhaus, R. Saito, and A. Jorio, "Raman spectroscopy of carbon nanotubes," *Physics Reports*, vol. 409, pp. 47-99, Mar. 2005.
- [75] J. L. Bahr, E. T. Mickelson, M. J. Bronikowski, R. E. Smalley, and J. M. Tour, "Dissolution of small diameter single-wall carbon nanotubes in organic solvents?" *Chem. Commun.*, vol. 2, pp. 193-194, Jan. 2001.
- [76] A. Hirsch, "Functionalization of single-walled carbon nanotubes," *Angew. Chem. Int. Ed.*, vol. 41, pp. 1853-1859, Jun. 2002.
- [77] R. Haggemueller, S. S. Rahatekar, J. A. Fagan, J. Chun, M. L. Becker, R. R. Naik, T. Krauss, L. Carlson, J. F. Kadla, P. C. Trulove, D. F. Fox, H. C. DeLong, Z. Fang, S. O. Kelley, and J. W. Gilman, "Comparison of the quality of aqueous dispersion of single wall carbon nanotubes using surfactants and biomolecules," *Langmuir*, vol. 24, pp. 5070-5078, Apr. 2008.
- [78] M. Vosgueritchian, M. C. LeMieux, D. Dodge, and Z. Bao, "Effect of surface chemistry on electronic properties of carbon nanotube network thin film transistors," *ACS Nano*, vol. 4, pp. 6137-6145, Oct. 2010.
- [79] S. Auvray, V. Derycke, M. Goffman, A. Filoramo, O. Jost, and J. Bourgoin, "Chemical optimization of self-assembled carbon nanotube transistors," *Nano Lett.*, vol. 5, pp. 451-455, Mar. 2005.
- [80] R. Krupke, S. Malik, H. B. Weber, O. Hampe, M. M. Kappes, and H. v. Löhneysen, "Patterning and visualizing self-assembled monolayers with low-energy electrons," *Nano Lett.*, vol. 2, pp. 1161-1164, Oct. 2002.

- [81] F. C. Krebs, "Fabrication and processing of polymer solar cells: A review of printing and coating techniques," *Solar Energy Materials & Solar Cells*, vol. 93, pp. 394-412, Apr. 2009.
- [82] Q. Gong, E. Albert, B. Fabel, A. Abdellah, P. Lugli, M. B. Chan-Park, and G. Scarpa, "Solution-processable random carbon nanotube networks for thin-film transistors," in *Proc. 11<sup>th</sup> IEEE Conf. Nanotechnology*, Portland, USA, 2011, pp. 378-381.
- [83] M. C. LeMieux, M. Roberts, S. Barman, Y. W. Jin, J. M. Kim, and Z. Bao, "Self-sorted, aligned nanotube networks for thin-film transistors," *Science*, vol. 321, pp. 101-104, Jul. 2008.
- [84] Y. Kim, N. Minami, W. Zhu, S. Kazaoui, R. Azumi, and M. Matsumoto, "Langmuir-Blodgett films of single-wall carbon nanotubes: Layer-by-layer deposition and in-plane orientation of tubes," *Jpn. J. Appl. Phys.*, vol. 42, pp. 7629-7634, Dec. 2003.
- [85] L. Hu, D. S. Hecht, and G. Grüner, "Percolation in transparent and conducting carbon nanotube networks," *Nano Lett.*, vol. 4, pp. 2513-2517, Dec. 2004.
- [86] J. Ahn, H. Kim, K. J. Lee, S. Jeon, S. J. Kang, Y. Sun, R. G. Nuzzo, and J. A. Rogers, "Heterogeneous three-dimensional electronics by use of printed semiconductor nanomaterials," *Science*, vol. 314, pp. 1754-1757, Dec. 2006.
- [87] R. T. Weitz, U. Zschieschang, F. Effenberger, H. Klauk, M. Burghard, and K. Kern, "High-performance carbon nanotube field effect transistors with a thin gate dielectric based on a self-assembled monolayer," *Nano Lett.*, vol. 7, pp. 22-27, Jan. 2007.
- [88] Z. Chen, J. Appenzeller, J. Knoch, Y. Lin, and P. Avouris, "The role of metal-nanotube contact in the performance of carbon nanotube field-effect transistors," *Nano Lett.*, vol. 5, pp. 1497-1502, Jul. 2005.
- [89] Y. X. Zhou, A. T. Johnson, Jr., J. Hone, and W. F. Smith, "Simple fabrication of molecular circuits by shadow mask evaporation," *Nano Lett.*, vol. 3, pp. 1371-1374, Oct. 2003.
- [90] F. Schwierz, "Graphene transistors," *Nature Nanotechnology*, vol. 5, pp. 487-496, Jul. 2010.
- [91] Q. Cao, M. Xia, C. Kocabas, M. Shim, J. A. Rogers, and S. V. Rotkin, "Gate capacitance coupling of singled-walled carbon nanotube thin-film transistors," *Appl. Phys. Lett.*, vol. 90, 023516, Jan. 2007.
- [92] A. Le Louarn, F. Kapche, J. Bethoux, H. Happy, G. Dambrine, V. Derycke, P. Chenevier, N. Izard, M. F. Goffman, and J. Bourgoïn, "Intrinsic current gain cutoff frequency of 30 GHz with carbon nanotube transistors," *Appl. Phys. Lett.*, vol. 90, 233108, Jun. 2007.
- [93] F. Schwierz and J. J. Liou, "RF transistors: Recent developments and roadmap toward terahertz applications," *Solid-State Electronics*, vol. 51, pp. 1079-1091, Aug. 2007.

- [94] L. Nougaret, H. Happy, G. Dambrine, V. Derycke, J. Bourgoin, A. A. Green, and M. C. Hersam, "80 GHz field-effect transistors produced using high purity semiconducting single-walled carbon nanotubes," *Appl. Phys. Lett.*, vol. 94, 243505, Jun. 2009.
- [95] M. S. Dresselhaus, A. Jorio, M. Hofmann, G. Dresselhaus, and R. Saito, "Perspectives on carbon nanotubes and graphene Raman spectroscopy," *Nano Lett.*, vol. 10, pp. 751-758, Mar. 2010.
- [96] A. M. Rao, E. Richter, S. Bandow, B. Chase, P. C. Eklund, K. A. Williams, S. Fang, K. R. Subbaswamy, M. Menon, A. Thess, R. E. Smalley, G. Dresselhaus, and M. S. Dresselhaus, "Diameter-selective Raman scattering from vibrational modes in carbon nanotubes," *Science*, vol. 275, pp. 187-191, Jan. 1997.
- [97] P. T. Araujo, P. B. C. Pesce, M. S. Dresselhaus, K. Sato, R. Saito, and A. Jorio, "Resonance Raman spectroscopy of the radial breathing modes in carbon nanotubes," *Physica E*, vol. 42, pp. 1251-1261, Mar. 2010.
- [98] Q. Bao, Y. Gan, J. Li, and C. M. Li, "Ex and in situ confocal Raman studies of organic thin film and its on-working transistors," *J. Phys. Chem. C*, vol. 112, pp. 19718-19726, Dec. 2008.
- [99] N. Pimparkar, Q. Cao, J. A. Rogers, and M. A. Alam, "Theory and practice of 'striping' for improved on/off ratio in carbon nanonet thin film transistors," *Nano Res.*, vol. 2, pp. 167-175, Feb. 2009.
- [100] A. Behnam, V. K. Sangwan, X. Zhong, F. Lian, D. Estrada, D. Jariwala, A. J. Hoag, L. J. Lauhon, T. J. Marks, M. C. Hersam, and E. Pop, "High-field transport and thermal reliability of sorted carbon nanotube network devices," *ACS Nano*, vol. 7, pp. 482-490, Jan. 2013.
- [101] Q. Gong, V. D. Bhatt, E. Albert, A. Abdellah, B. Fabel, P. Lugli, and G. Scarpa, "On the performance of solution-processable random network carbon nanotube transistors: unveiling the role of network density and metallic tube content," *IEEE Trans. Nanotechnology*, vol. 13, pp. 1181-1185, Nov. 2014.
- [102] Q. Gong, E. Albert, B. Fabel, A. Abdellah, P. Lugli, G. Scarpa, and M. B. Chan-Park, "Solution-processed random carbon nanotube networks used in thin-film transistor," in *Nanoelectronic Device Applications Handbook*, J. Morris and K. Iniewski, Ed. New York: CRC Press, 2013, chapter 42.
- [103] W. Kim, A. Javey, O. Vermesh, Q. Wang, Y. Li, and H. Dai, "Hysteresis caused by water molecules in carbon nanotube field-effect transistors," *Nano Lett.*, vol. 3, pp. 193-198, Feb. 2003.

- [104] S. H. Jin, A. E. Islam, T. Kim, J. Kim, M. A. Alam, and J. A. Rogers, "Sources of hysteresis in carbon nanotube field-effect transistors and their elimination via methylsiloxane encapsulants and optimized growth procedures," *Adv. Funct. Mater.*, vol. 22, pp. 2276-2284, Jun. 2012.
- [105] D. Estrada, S. Dutta, A. Liao, and E. Pop, "Reduction of hysteresis for carbon nanotube mobility measurements using pulsed characterization," *Nanotechnology*, vol. 21, 085702, Jan. 2010.